Development of a Multi-band Plenoptic Camera for High Temperature Measurements

by

Dustin Kelly

A thesis submitted to the Graduate Faculty of
Auburn University
in partial fulfillment of the
requirements for the Degree of
Master of Science

Auburn, Alabama
May 2, 2020

Keywords: Plenoptic Imaging, Pyrometry, Multi-spectral Imaging

Approved by

Brian Thurow, Chair, W. Allen and Martha Reed Professor of Aerospace Engineering
David Scarborough, Assistant Professor of Aerospace Engineering
Roy Hartfield, Walt & Virginia Woltosz Professor of Aerospace Engineering

Abstract

In this thesis, the development of a novel multi-band plenoptic pyrometer is discussed and applied to several applications of interest in the engineering field. The multi-band plenoptic camera is a non-contact measurement technique used to determine the temperature of a surface or flame using the emitted radiation from a body, which can also be referred to as an optical pyrometer. Traditional two-dimensional (2D) pyrometers are limited by the number of wavelengths available, requiring assumptions to be made about surface emissivity. Errors in emissivity can lead to large errors in temperature measurements. The multi-band plenoptic camera is a combination of a plenoptic camera and a linearly variable wavelength filter, which can be used to instantaneously and robustly measure 2D temperatures. The present experiments evaluate the multi-band camera's ability to determine temperatures from the captured spectral content using a pyrometric technique called spectral pyrometry. Discussion of the design concept and process are presented. Microlens, wavelength, and temperature calibration are data processing steps required for temperature calculations. Three experiments to test the camera's efficacy in measuring temperature are discussed, including a graphite plate at constant and varying temperatures, solid rocket strand burner plumes, and solidifying copper. The multi-band plenoptic camera captured temperatures within the range of thermocouple accuracy for both constant and varying graphite temperatures. The solid rocket plume measurements were of two fuels with a known temperature difference caused by aluminum (Al) particles added to one. Preliminary results showed a temperature increase of 400°C when Al was added to the fuel. Captured temperatures had a range of 800°C. Finally, the copper experiment was designed to test the ability to calculate temperatures with challenging material properties. The multi-band camera was able to distinguish between temperatures of the liquid and solid copper. Several challenges, including low emissivity, high background temperature, and boundary artifacts need to be resolved to reduce errors in temperature measurements. Future work will investigate simultaneously using spectral and angular information to obtain 3D temperatures.

Acknowledgments

The work presented in this thesis required countless support by many individuals to be completed. First, I would like to thank Dr. Thurow for his guidance and knowledge throughout the research process. He is certainly very passionate about progressing the aerodynamic diagnostic field, and he passed that along to me. He helped me advance both technically and professionally in the aerospace field. I would also like to thank Dr. Paul Danehy and his group at NASA Langley for their support of the project. The group provided critical supplies and input on the development of the multi-band plenoptic camera. Another research group that provided crucial equipment for further development was the Alabama Micro/Nano Science and Technology Center, of which, I would like to thank M. C. Hamilton and J. A. Sellers for the flexibility and knowledge of the equipment. The Combustion Physics Laboratory under Dr. Scarborough provided knowledge and materials to conduct experiments with solid rocket plumes. Of which, I thank Austin Phillips for manufacturing the solid fuel samples along with helping during the experiments. I would like to thank Dr. David Scarborough and Dr. Roy Hartfield for serving on my committee. Members of the Advanced Flow Diagnostic Laboratory provided academic and technical guidance during my studies, which helped to produced many friendships. Finally, I would like to thank my family for the encouragement and support throughout my educational journey, without it, I could not have done it.

Table of Contents

List of Figures

List of Tables

Chapter 1

Introduction

Optical pyrometry is the technique of capturing emitted radiation to determine the temperature of a surface or body. Since radiation can travel through most transparent mediums, optical pyrometry is a non-contact temperature measurement. The non-intrusive nature of optical pyrometry results in the ability to obtain measurements without interfering with other aspects of an experiment. Alternatively, intrusive measurements require the devices to withstand extreme temperatures, which is not always possible with temperatures that exceed material limits like combustion gases and reentry vehicles. Intrusive methods can interfere with aspects of the experiment or measurement. For example, thermocouples can be inserted in solid rocket fuel to measure temperatures within the fuel, but the thermocouples can weaken the fuel and increase heat transfer into the fuel. Hypersonic vehicles, like reentry vehicles, generate extreme temperatures that weaken or destroy the vehicle. Therefore, research and new diagnostic tools, including the current work, are needed to understand heating on these vehicle structures. Many other applications, including additive manufacturing and combustion, will also benefit from new diagnostic tools like optical pyrometers to better understand high temperature processes that are occurring.

There are different techniques which have been developed for optical pyrometry. Single-wavelength pyrometry captures radiation intensity at one wavelength or band, while multi-wavelength pyrometry captures two or more discrete wavelengths or wavelength bands for temperature measurements. A wavelength band is a finite range of wavelengths, which will have one corresponding intensity. Optical pyrometry is limited due to factors including non-contact surface emissivity, reflectivity, and the surrounding environment. Single-wavelength pyrometry is very sensitive to varying material properties including emissivity and surface finish, where

a small error in emissivity approximation generates large errors in temperature. Multi-spectral pyrometry was developed to compensate for unknown emissivity. Analysis of different multi-spectral techniques have been discussed by Araújo [1]. Many of the multi-spectral pyrometry techniques require emissivity to be calculated for a temperature measurement, where slight error in emissivity calculation can generate large errors in temperature measurements [15]. Another technique, called spectral pyrometry [9], has been developed to reduce the effects of emissivity in temperature measurements by diminishing the effects of fluctuating emissivity. For high temperature measurements, the visible spectra is better suited than the infrared spectrum due to large temperature uncertainties that arise from emissivity uncertainty in the infrared spectrum [8].

Traditional multi-color pyrometers only measure temperatures around a point, which can limit the ability to capture dynamic and complex temperature structures in engineering applications. However, there has been new spectral camera development that allows sensors to capture two dimensional (2D) multi-wavelength information [10]. Some of the most common color cameras used for pyrometry are filter wheels, beamsplitters, and pixel level filters. These designs have trade-offs between complexity of the camera, flexibility in changing wavelengths, and time required between wavelength acquisition. Cameras that implement beamsplitters can capture multiple high-resolution wavelength images, but they have increasing complexities when increasing the number of acquired wavelengths. Alternatively, filter wheels have a simplistic design, but wavelength acquisition requires time between each wavelength image. While pixel level filter cameras are both compact and instantaneous, it is difficult to change wavelength filters on the filter array.

The multi-band plenoptic camera has compactness like pixel level filters, while still having ability to easily change filters and wavelengths. The new diagnostic tool provides a 2D snapshot image of 15 wavelength bands across the visible and near-infrared spectrum. The multi-band plenoptic pyrometer combines a plenoptic camera with a linearly variable wavelength filter, also known as a 'rainbow' filter, that is placed at the aperture plane of the camera. The configuration of a plenoptic camera is unique due to the placement of a microlens array between the main lens and the image sensor. The microlens array discretizes the main lens,

which gives the ability to sample both spatial and angular information of light in a single snapshot. Adding the rainbow filter at the main lens, maps wavelengths to a portion of the angular information.

The objective of the current work is to design and evaluate the multi-band plenoptic pyrometer's efficacy in calculating 2D temperature maps of both surfaces and flames using the spectral pyrometry technique. Unlike most 2D snapshot pyrometers, which sample at most 4 wavelengths, the multi-band plenoptic provides enough wavelength information to minimize the effect of varying emissivity. The additional wavelength information allows for wavelengths to be chosen during post-processing, granting flexibility during acquisition regarding varying temperature and material properties. Such a diagnostic tool will be crucial for temperature measurements in dynamic systems like solid rocket plumes, heating caused by hypersonic flight, and additive manufacturing, which all require measuring 2D temperatures well above 1000 K.

Chapter 2 provides background information on optical pyrometry techniques and spectral imaging cameras that are used to capture wavelength information for pyrometry. The chapter begins by covering the fundamental information about thermal radiation caused by a material's temperature. Then, a review of optical pyrometry methods including single and multi-wavelength pyrometry, previous research, and applications. The chapter concludes with a discussion on spectral snapshot imaging. Chapter 3 provides the foundation for light-field imaging to develop the concept of a plenoptic cameras and their unique capabilities. The chapter finishes by describing multi-band plenoptic imaging and how it takes advantage of the plenoptic capabilities.

Chapter 4 provides the steps and improvements that have been made from the preliminary design of the multi-band adapter for the plenoptic camera, starting with the origins of the design from Fahringer [11]. This chapter will cover the preliminary design, artifacts that originate from the design, and iterations to the initial design and algorithm to compensate for the artifacts. Chapter 5 will then step through the different data processing that is required to calculate 2D temperature maps of a given target. Chapter 6 reviews three experimental setups that were designed to test the multi-band plenoptic efficacy in temperature measurements. The first experiment captures temperatures of graphite at constant and varying temperatures. The

multi-band plenoptic camera is used to measure temperatures of two different solid fuels in a strand burner for the second experiment. The third experiment consists of measuring of temperatures of solidifying copper in a metal foundry. Chapter 7 presents the results from the three different experiments and discusses the performance of the multi-band plenoptic camera for each case. Finally, Chapter 8 concludes the paper reviewing the contents of the experiments and discussion.

Chapter 2

Background

This chapter covers the fundamentals of radiation and optical pyrometry. Initially, this chapter will cover the concepts of radiation that are required to understand optical pyrometry. For optical pyrometry, different techniques including: single-wavelength, dual-wavelength, multi-wavelength, and spectral pyrometry will be described along with past research and applications. The chapter will then discuss the fundamentals of spectral imaging and typical ways of capturing wavelength information used for pyrometry. Overall, the purpose of this chapter is to provide information on how the different pyrometry techniques compare to the proposed pyrometer.

2.1 Radiation

Radiation is a sizable topic that cannot be covered completely in this section. Therefore, this section will focus on basics required for optical pyrometry. Thermal radiation is the emission of energy through electromagnetic waves as a result of a body's temperature. All objects at room temperature are continuously emitting radiation that is not visible to the human visual system because the majority of emitted energy is in the infrared region (1μm to 1000μm). The mechanism for radiation energy release is from excited electrons vibrating or transitioning to lower energy levels in an atom or molecule of the object. Radiation from an opaque solid or liquid originates from molecules or atoms within 1 μm from the surface because internal molecules will absorb their adjacent molecules' radiation. For gases and transparent materials, radiation is emitted in a volumetric manner, where overall radiation is a combination of emitted radiation from infinitely small volumes that make up the global volume described by Bergman and Lavine [16].

A blackbody radiator is a theoretical body that "absorbs all incident radiation regardless of wavelength and direction" [16]. A blackbody is also a diffuse emitter, which means emitted radiation only depends on temperature and wavelength and not the direction of emission. While some surfaces are a close approximation of a blackbody, no surface actually has the exact properties of a blackbody. The equation that describes the spectral intensity emitted from a blackbody is given by Planck's equation as shown in Equation 2.1.

$$I_b(\lambda, T) = \frac{2hc^2}{\lambda^5} \frac{1}{\exp(\frac{hc}{\lambda kT}) - 1} \tag{2.1}$$

where h is the universal Planck's constant, k is the universal Boltzmann constant, and c is the speed of light in vacuum. Figure 2.1 displays intensities given by Equation 2.1 for three different temperatures, shown in blue. Some things to note about Planck's equation: (1) it is a smooth curve for all wavelengths for a certain temperature, (2) the intensities increase over all wavelengths for an increase in temperature, and (3) the radiation concentration shifts to shorter wavelengths as the temperature increases. Another equation that approximates blackbody radiation is given by Wien's distribution law as shown in Equation 2.2.

$$I_{Wien}(\lambda, T) = \frac{2hc^2}{\lambda^5} \exp\left(-\frac{hc}{\lambda kT}\right) \tag{2.2}$$

Wien's distribution law is very similar to Planck's equation without subtracting by one in the denominator, which allows the exponential to be easily inverted. Wien's distribution law is easier to manipulate compared to Equation 2.1, therefore, Wien's distribution law is often used for pyrometry techniques. With the equation only being an approximation, the equation only matches Planck's equation at wavelengths shorter than the wavelength corresponding to maximum intensity. A comparison between the two functions at 1200 K, 1500 K, and 1800 K is provided in Figure 2.1. The intensities before the peak are very similar, while at longer wavelengths the slopes are similar but actually diverge with increasing wavelength. Therefore, it is best to use Wien's law at wavelengths shorter than where the peak intensity occurs. The peak intensity of Wien's equation for a given temperature is given by Equation 2.3.

$$\lambda_{max} T = C_3 \tag{2.3}$$

where the constant is C_3 = 2898 μm·K. For a temperature of 1000K, the peak is in the infrared region at 2.9 μm. The peak doesn't appear in the visible wavelengths until approximately 4000 K.

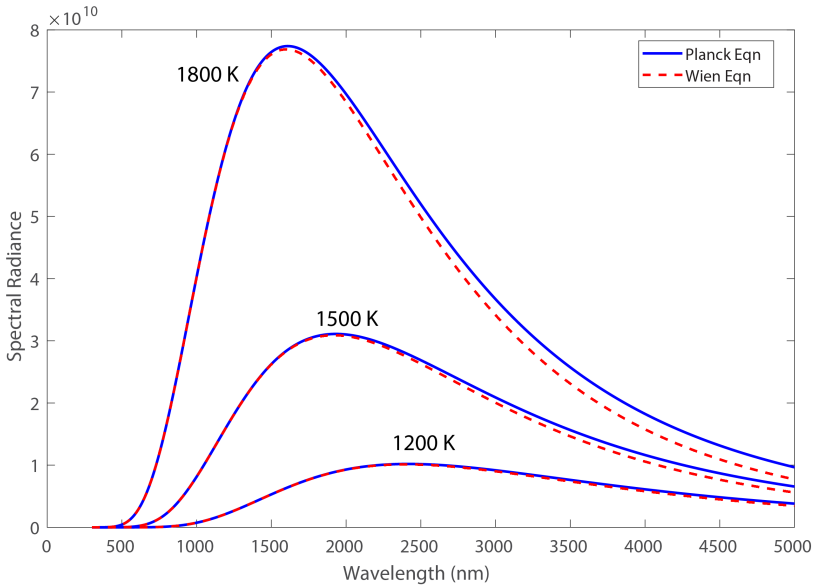

Figure 2.1: Comparison between Planck's blackbody equation (blue) and Wien's distribution law (red) at temperatures of 1200 K, 1500 K, and 1800 K.

Emissivity (ε), reflectivity (ρ), absorptivity (α), and transmissivity (τ) are material properties that affect emitted radiation and irradiation. Emissivity is the surface property that describes the amount of radiation that is emitted. Reflectivity is the fraction of irradiation that is reflected by the surface. The fraction of irradiation that is absorbed by the body is called absorptivity, and the fraction of the irradiation that transmits through the surface is called transmissivity. Irradiation is all radiation that is incident on a surface from the surroundings. All irradiation must be reflected, absorbed, or transmitted, therefore, it must follow Kirchhoff's law as given by Equation 2.4.

$$\rho + \alpha + \tau = 1 \tag{2.4}$$

For an opaque material, $\tau = 0$. As discussed earlier, a blackbody absorbs all radiation, therefore, $\alpha = 1$ and $\rho = 0$ for a blackbody. Overall, emissivity affects pyrometry the most. Emissivity accounts for the non-blackbody nature of emitted radiation from a surface. Emissivity is defined by Equation 2.5,

$$\varepsilon(\lambda, T) = \frac{I(\lambda, T)}{I_b(\lambda, T)} \tag{2.5}$$

where I_b is blackbody intensity and I is actual intensity the material radiates at a wavelength and temperature. Since no material can radiate more than a blackbody at a given temperature and wavelength, it must be the case that: $0 \leq \varepsilon \leq 1$. The emissivity of an object can change with both temperature and wavelength. In pyrometry, variations in emissivity will have a major effect on temperature measurements. Absortivity, reflectivity, and transmissivity can also change with temperature and wavelength. A gray body is one which α and ε do not vary with wavelength. For any gray body, spectral, direction emissivity and absorptivity are equal ($\alpha_{\lambda,\phi} = \varepsilon_{\lambda,\phi}$) under any condition. Spectral emissivity and absorptivity are equal ($\alpha_\lambda = \varepsilon_\lambda$) for a gray body as long as the irradiation is diffuse or the surface is diffuse. A blackbody is a special form of a gray body where $\alpha = \varepsilon = 1$. The assumption of a gray body is used for many applications of optical pyrometry [16] because it simplifies equations.

2.2 Optical Pyrometry

An optical pyrometer is a device that captures emitted radiation from a body of interest, which typically, uses optics to focus radiation onto a line or 2D sensor. Temperature measurements have been conducted for a point, one-dimensions, two-dimensions, and three-dimensions. One main advantage of a pyrometer is that it does not require a probe to be in contact with a surface of interest. Separation from the environment of the target allows for the optical device to measure extreme temperatures without being exposed to those temperatures. Contact methods can impact measured temperatures due to heat transfer, however, non-contact methods are separated eliminating the issue. Most pyrometers use the infrared (IR) range because most engineering applications have peak emitted radiation in the IR range. It is not until higher temperatures

that radiation is high enough to be recorded in the visible spectrum. Typically, signal generated by a detector caused by radiation is used to determine temperature by using a function that is formed during calibration as explained by Araújo [1].

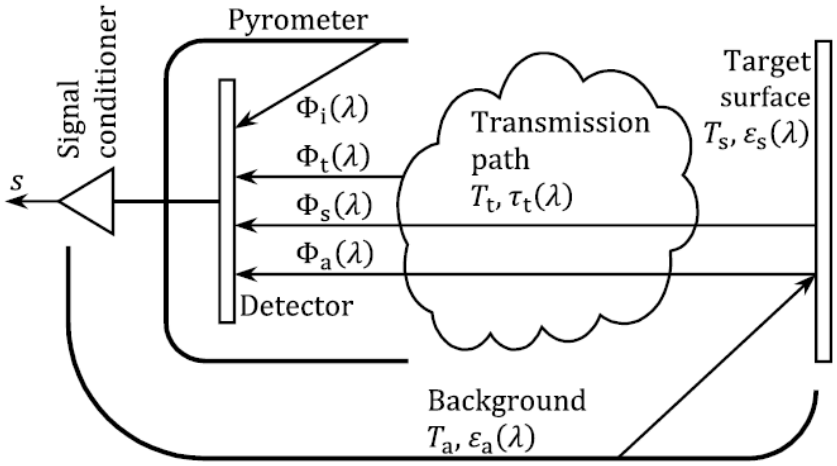

Figure 2.2: Schematic of different radiation fluxes captured by a pyrometer. Taken from Arújo[1]

Figure 2.2 shows four different emitted radiation fluxes that are captured by a pyrometer including: the target surface ($\Phi_s(\lambda)$), background reflected radiation ($\Phi_a(\lambda)$), radiation emitted by molecules in transmission path ($\Phi_t(\lambda)$), and radiation emitted by inner surfaces of the pyrometer ($\Phi_i(\lambda)$). Radiation emitted by the pyrometer can be disregarded unless the surfaces of the pyrometer are greater than or equal to the target surface's temperature. Therefore, high temperature measurements can disregard this radiation because radiation intensities scale on the order of O(T^4). Radiation reaching a pyrometric sensor emitted from a target is given by Equation 2.6 [1],

$$\Phi_s(\lambda) = \varepsilon_s(\lambda)\tau_t(\lambda)I_b(\lambda, T_s) \tag{2.6}$$

where $\varepsilon_s(\lambda)$ is the spectral emissivity of the target surface, $\tau_t(\lambda)$ is the spectral transmissivity of the material making up the transmission path, and T_s is the temperature of the target surface [1].

Background radiation flux will also be captured by the pyrometer. If the target is completely surrounded by a background surface, generally a good assumption, the background will

act as a blackbody with a temperature of T_a with respect to the target surface. Background radiation received by the camera is given by Equation 2.7,

$$\Phi_a(\lambda) = [1 - \varepsilon_s(\lambda)]\tau_t(\lambda)I_b(\lambda, T_a) \tag{2.7}$$

where reflectivity of the target surface was replaced with $[1 - \varepsilon_s(\lambda)]$ because of the assumption that $\alpha(\lambda) = \varepsilon(\lambda)$ [1].

Lastly, spectral radiation is emitted by the transmission path as given by Equation 2.8,

$$\Phi_t(\lambda) = [1 - \tau_t(\lambda)]I_b(\lambda, T_t) \tag{2.8}$$

where T_t is the temperature of the transmission medium. With the transmission path being air for most experiments, there are regions of the spectral transmissivity such that, $\tau_t(\lambda) \simeq 1$. With this in mind, many of the pyrometry techniques use spectra that are not affected by transmissivity including the visible (400-750nm), near-infrared (750-1000nm), short-wave infrared range (2-5μm), and long-wave infrared range (8-14μm). Assuming $\tau_t(\lambda) \simeq 1$ reduces Equation 2.6 and Equation 2.7, while it eliminates Equation 2.8 [1].

Output signal of the pyrometer is an accumulation of all the radiation fluxes explained earlier [17]. However, the pyrometer detector has a spectral response ($\alpha_d(\lambda)$) because not all of the irradiation that reaches the sensor will be recorded. Spectral response encompasses quantum efficiency of the sensor and attenuation caused by the optical system. Therefore, the signal generated by irradiation is given by Equation 2.9 [1],

$$s = k \int_{\lambda=\lambda'}^{\lambda''} \alpha_d(\lambda)\{\varepsilon_s(\lambda)I_b(\lambda, T_s) + [1 - \varepsilon_s(\lambda)]I_b(\lambda, T_a) + \Phi_i(\lambda)\}d\lambda \tag{2.9}$$

where k is a proportionality constant dependent on gain of the electrical sensor, and λ' and λ'' are the lower and upper wavelengths limits of integration respectively.

There are many variations in pyrometers including the number of wavelengths captured, the spectrum used for pyrometry, and size of the wavelength range captured. In this next part, a comparison of the different pyrometer variations is explained along with application examples.

2.2.1 Single-wavelength pyrometry

One of the first designs for optical pyrometers used intensities recorded at one wavelength, called single-wavelength pyrometry. Since this paper focuses on multi-wavelength pyrometry, single-wavelength pyrometry is only discussed shortly to understand its usefulness and downfalls. Most commercially available pyrometers use single-wavelength pyrometry because of the simplicity and low-cost designs. However, selection of the proper wavelength can be very challenging. Unknown emissivity and material properties can create large errors in temperature measurements. Commercially available pyrometers give the option to input an emissivity value to help mitigate this issue. Most commercial cameras, also known as thermal cameras, use an IR sensor, since most applications require measurements around room temperature. Some varieties of thermal cameras offer cooled sensors, which lowers sensor temperatures to cryogenic levels. Lowering the temperature reduces the thermal noise of the sensor. It also reduces the effects of radiation emitted by the pyrometer (Φ_i).

Zhang [18] used a monochromatic pyrometer to calculate temperatures during casting billets, where different emissivity properties due to oxidation can cause issues. The single-wavelength pyrometer consisted of a CCD sensor camera with a narrow band-pass optical filter with a center wavelength of 780nm. A colorimetric thermometer with wavelengths $0.8\mu m$ and $1.05\mu m$ was used to perform error correction. Zhang found the relative error of the system was 8.1% in the temperature range form 800°C and 1200°C, even with emissivity correction by a dual-wavelength colorimetric thermometer. This method is also specific for the application. For most engineering applications at cooler temperatures, the errors generated are acceptable.

Another single-wavelength pyrometer was compared to a dual-wavelength method for temperature measurements of gas turbine blades in the work by Ketui *et al.* [2]. To ensure wavelengths were not affected by CO_2 and H_2O, the wavelengths of 1.6 and 2.2 μm were used. An Ex-InGaAs detector was used to make capture these wavelengths. The probe had to be scanned across the blade for different sensor integration periods since the pyrometer captured wavelength information from a single point. To compare temperature measurements captured

by the pyrometer, Ketui placed a 3D model of the vanes and blades in a simulation that calculated blade temperatures. The simulation temperature distribution along with the pyrometer scanning path is shown in Figure 2.3. Single-wavelength pyrometry measurements were conducted for both wavelengths captured. At lower emissivity (ε = 0.2) and relatively high temperatures (T = 1350 K), single-wavelength pyrometry produced errors of approximately 70% and 90% for 1.6 μm and 2.2 μm, respectively. In the same case, using a dual-wavelength ratio method, assuming a gray body, produced errors of approximately 30%. Ketui suggested that corrections to the wavelength information or temperature calculations are required for temperature measurements of reflective surfaces surrounded by high temperature surfaces to ensure reliable measurements.

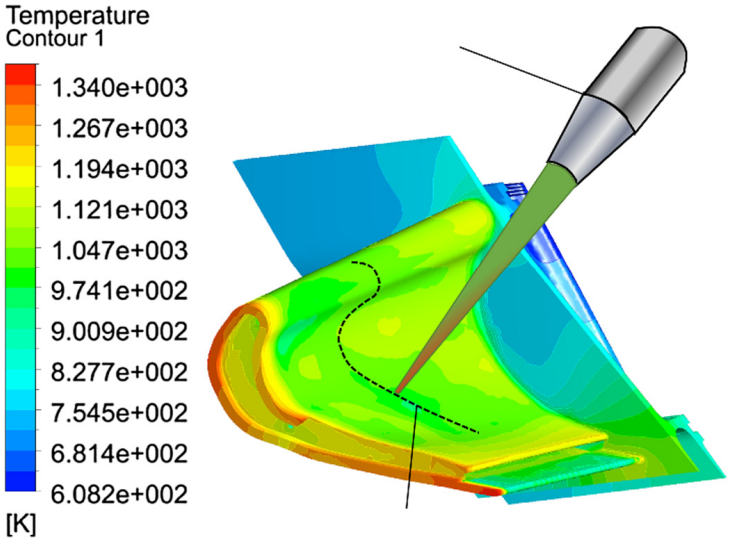

Figure 2.3: Schematic that presents the temperature contour map on a turbine blade with the pyrometer probe scanning path depicted across the blade. Taken from Ketui [2].

2.2.2 Dual-wavelength pyrometry

Dual-wavelength pyrometry is a subset of multi-wavelength pyrometry, which records irradiation at two distinct wavelengths to calculate temperature. Dual-wavelength pyrometry techniques have been developed for both surface and soot pyrometry. One of the biggest advantages to dual-wavelength is that it uses a ratio between the wavelength intensities, reducing the need to know emissivity. Generally, dual-wavelength pyrometry is limited by assuming surfaces and

soot are gray bodies with respect to the two wavelengths that are captured. Since spectral emissivity can vary widely, this assumption can lead to errors in temperature measurements when spectral emissivity is not known. Some methods try to determine a surface emissivity model, eliminating a gray body assumption. However, with the increased wavelength information and less dependence on emissivity, dual-wavelength pyrometers provide more accurate results [1].

In surface pyrometry, the background needs to be cool enough relative to the target such that Φ_a can be neglected. There are two main methods for dual-wavelength surface pyrometry called radiation method and temperature method. In both of these methods, several different equations can be used to determine surface emissivity. For radiation method, temperature is calculated using Equation 2.10 [1],

$$T_s = \frac{c_2(\lambda_2 - \lambda_1)}{\lambda_1\lambda_2\left(\ln\frac{s_2k_1}{s_1k_2} + 5\ln\frac{\lambda_2}{\lambda_1} + \ln\frac{\varepsilon_1}{\varepsilon_2}\right)} \tag{2.10}$$

where s_1 and s_2 are the output signals for λ_1 and λ_2, respectively. Similarly, k is the proportionality constant found during calibration for each wavelength. The spectral emissivity in this equation will either need to be known or constant. For temperature method, temperature is calculated using Equation 2.11 [1].

$$\frac{1}{T_s} = \frac{1}{(\lambda_2 - \lambda_1)}\left(\frac{\lambda_2}{T_1} - \frac{\lambda_1}{T_2} + \frac{\lambda_1\lambda_2}{c_2}\ln\frac{\varepsilon_1}{\varepsilon_2}\right) \tag{2.11}$$

The above method has been used to calculate temperatures of different aluminum alloys that possess different surface characteristics as explained by Tsai *et al.* [19]. However, prior knowledge of surface emissivity of the alloys was needed to determine the appropriate emissivity algorithm. Danehy *et al.* [3] developed a three-color pyrometer based on plenoptic imaging using wavelengths 800nm, 632nm, and 550nm. However, temperature measurements only used 800nm and 550nm wavelength intensities because it produced the most temperature sensitivity. The ratios between 800nm and 550nm intensities at different known temperatures were fit to an exponential curve that was used for temperature measurements. Temperature maps of a ceramic heating element, displayed in Figure 2.4, shows temperature measurements deteriorating when the temperature drops below 1100 K because signal-to-noise ratio decreased for a fixed

exposure time. Looking at one of the images, temperature variations of 20 K can be seen, when the target surface was approximately 1250 K.

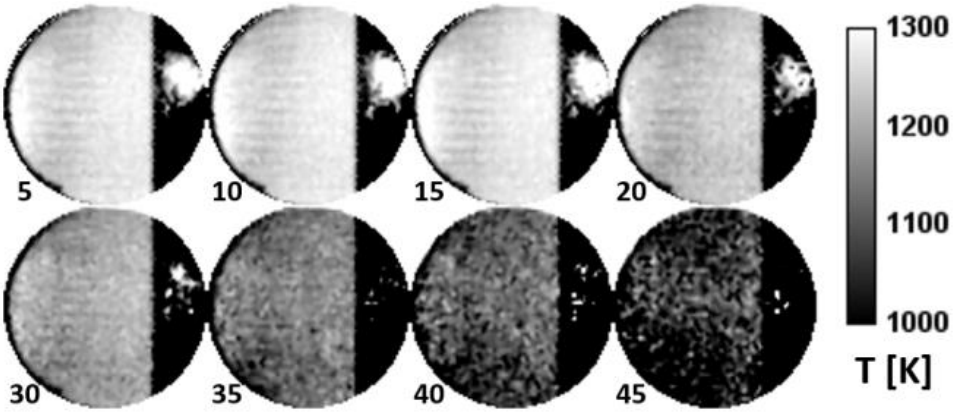

Figure 2.4: Temperature distributions of a ceramic heating element during steady state then cool down. Taken from Danehy [3].

For dual-wavelength soot pyrometry, a measurement in temperature also requires knowing the concentration of soot particles present in the combustion flame because the amount of radiation depends on the soot volume. For 2D and 3D temperature measurements, the soot volume fraction also needs to be determined in those dimensions. Emissions are captured through a line of sight measurement, which results in temperature measurements to be biased toward the higher temperatures due to a T^4 dependency on emitted radiation [20]. Temperature is calculated using Equation 2.12,

$$T_s = \frac{c_2 \left(\frac{1}{\lambda_2} - \frac{1}{\lambda_1}\right)}{\ln\left(\frac{s_1}{s_2}\left(\frac{\lambda_1}{\lambda_2}\right)^5 \frac{\varepsilon_2}{\varepsilon_1}\right)} \tag{2.12}$$

where ε_1 and ε_2 are the spectral emissivity at λ_1 and λ_2, respectively. Typically, emissivity cannot be assumed to be a gray body in sooting flames due to changing composition. One emissivity model that has been used is shown in Equation 2.13,

$$\varepsilon_\lambda = 1 - \exp\left(-\frac{F_\lambda}{\lambda} f_v L\right) \tag{2.13}$$

where F is an index of refraction at a wavelength, f_v is the soot volume fraction, and L is the optical path length of the flame. An iterative method is required to update temperature and soot volume fraction because both calculations are coupled.

A study conducted by di Stasio and Massoli [21] pointed to the visible spectrum being superior to the infrared range because of uncertainties stemming from refractive index. Furthermore, Jenkins and Hanson [20] mentions that uncertainties in the infrared are dominated by the emissivity, and visible is dominated by emission intensity. When recording at low signal-to-noise intensities, errors can lead to uncertainties on the same order as those in the infrared region caused by emissivity.

Dual-wavelength pyrometry has been very popular in measuring temperatures in diesel engine combustion [22, 23] and turbulent flames. Dual-wavelength pyrometry has a minimum temperature of approximately 800 K when using the visible spectrum due to emitted intensities being too low to record at lower temperatures. Despite this short coming, the visible spectrum is the most used for dual-wavelength with diesel engines because concentration of pollutants is most important at the highest temperatures of the flame [20]. In recent times, a dual-wavelength pyrometer has been developed to measure temperatures in turbulent flames [1].

2.2.3 Multi-wavelength pyrometry

Mutli-wavelength pyrometry, in the context of the current work, refers to pyrometers that record irradiation at three or more wavelengths. The idea for multi-wavelength pyrometry is the additional wavelength information eliminates the need for the limiting assumption of a gray body that was used for some dual-wavelength pyrometry. Increasing the number of wavelengths, increases the ability to model spectral emissivity. In theory, the increased emissivity model will allow accurate temperature measurements across more materials and applications. However, each additional wavelength requires another emissivity parameter that is unknown. Therefore, there are $m+1$ unknowns and n measurements, where m is the number of emissivity parameters of the emissivity model, with the additional 1 for unknown temperature, and n is the number of wavelengths. Generally, multi-wavelength approach is an underdetermined system, where $m + 1 > n$ because optimally there is an emissivity parameter for every wavelength measured ($m = n$). Methods have been developed to reduce the number of emissivity unknowns to a maximum of $n - 1$. If $m < n - 1$, then the system is overdetermined and will have to be solved by a least-squares method [1]. Generally, an increase in captured wavelengths would increase

accuracy, however, Coates [15] showed that additional wavelengths ($n > 4$) can cause temperature error to grow for determined systems ($m = n - 1$). The growth in error is attributed to over-fitting of the emissivity models. Coates suggests that over-fitting errors may be reduced if n$\geq$2m.

As explained above, an emissivity model is an essential component to temperature measurements. Two of the commonly used models are shown in Equation 2.14 and Equation 2.15, where the a terms are variables found during calibration. The most popular model is a polynomial as given by Equation 2.14.

$$\varepsilon_s(\lambda_i) = a_0 + a_1\lambda_i + ... + a_{m-1}\lambda_i^{m-1} \tag{2.14}$$

$$\ln \varepsilon_s(\lambda_i) = a_0 + a_1\lambda_i + ... + a_{m-1}\lambda_i^{m-1} \tag{2.15}$$

Analysis of different multi-wavelength devices along with spectral range have been conducted. Initial analysis showed that use of the visible range did not give any benefit compared to infrared as discussed by Duvaut [24]. Duvaut used the middle infrared range (2-7μm) and the visible range (0.45-0.7μm) to measure temperatures of different metals at a range of (600K to 1200K). Issues with the visible spectrum originates from the difficulty in selecting a single emissivity model for a family of metals, and low signal-to-noise ratio (SNR) when temperatures are below 800K. Duvaut did report some precise results using monochromatic pyrometry in the visible spectrum. However, the temperature range used by Duvaut was on the low side, increasing uncertainty due to low emission intensity. Fu *et al.* [4] explains that emissivity uncertainty correlates to temperature uncertainty, for which there is more uncertainty in the infrared spectrum than the visible spectrum.

Many different multi-wavelength pyrometers have been developed using CCD cameras [25, 5, 3, 11, 26]. Ng and Fralick [27] used a multi-wavelength device to measure temperatures of several aerospace applications, including surface heating due to a jet burner and measurements of combustion gas temperatures. The multi-wavelength pyrometer had multiple sensors in order to record a wavelength range of 0.5μm - 2.5μm from a point on the target surface or

flame. The wavelengths towards the edges of the spectral range of the sensors deviated from other measurements due to poor signal. Madura [28] created a three-wavelength pyrometer capturing wavelengths of 1.6, 1.8, and 2μm, which were claimed to be suitable for metallic surfaces. He developed an algorithm that automatically chooses a function approximating emissivity values and a method of temperature calculations that minimizes errors. Fu *et al.* [26] created a fast fiber-optic multi-wavelength pyrometer, which used a CCD and a InGaAs detector to capture a wavelength range of 200nm-1700nm. Fiber optic cables relayed images captured by a collocating lens to a grating that diffracts the light onto the sensors. The pyrometer was used to measure temperatures of a hot oxidized steel sample, which was heated by both SiC heaters from the back and a butane burner on the front. The optimal bandwidths for these measurements were found to be $\Delta\lambda_{CCD}$ = 30nm and $\Delta\lambda_{InGaAs}$ = 50nm. The optimal bandwidths were found due to a trade-off between simple emissivity model assumptions and signal discrimination.

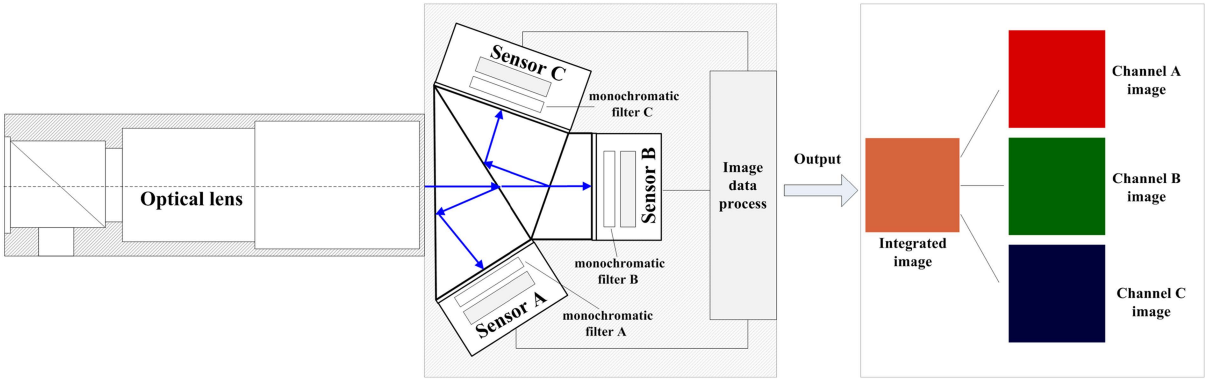

Figure 2.5: Schematic of the multi-wavelength pyrometer using beam splitters, monochromatic filters, and three CCD sensors. Taken from Fu [4].

Fu *et al.* [4] created a three-wavelength pyrometer using wavelengths in the visible and near-infrared range that measured temperatures of a ceramic model in a plasma flow. Figure 2.5 shows the design of the multispectral pyrometer used by Fu [4]. Center wavelengths of 700nm, 810nm, and 920nm, are used for the monochromatic filters in front of the sensors. Each CCD had to be micro-aligned to reduce spectrum artifacts. Figure 2.6 shows both colored images and temperature distributions of the ceramic model at different times. He showed the advantage of three-wavelength pyrometry to measure 2D temperatures with large spatial temperature

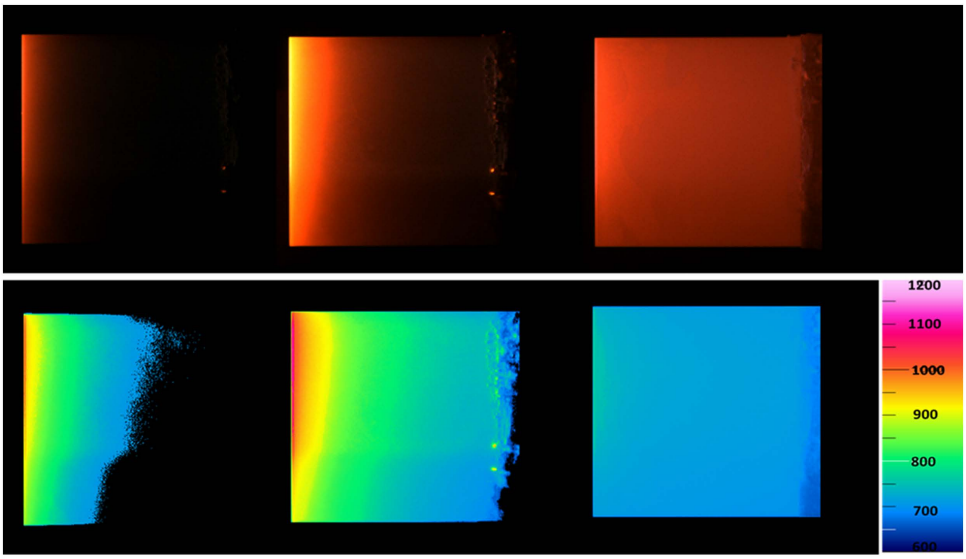

Figure 2.6: (Upper) Colored images produced using the three wavelength images captued by the camera and (lower) surface temperature distribution obtain at three heating times (a) initial transient, (b) steady state, and (c) cooling transient. Taken from Fu [4].

gradients. Temperature uncertainty was between 9.7°C - 13.2°C across the model. A new technique developed by Fu *et al.* [5], used multi-wavelength pyrometery to calculate sub-pixel temperatures on a fin in a plasma jet flow. The pyrometer used a high-speed near-infrared sensor to capture 175 wavelengths in the range of 1.0 - 1.65 μm. Typical pyrometers with similar design calculate an averaged temperature measurement, but Fu took the intensity distribution across the sensor to determine temperature gradients over the field of view. The new method was used to determine temperature of the same ceramic model in a plasma jet flow from above. Figure 2.7 shows the temperature distributions of the ceramic model for different cases. The temperature measurements agreed with the earlier paper by Fu *et al.* [4].

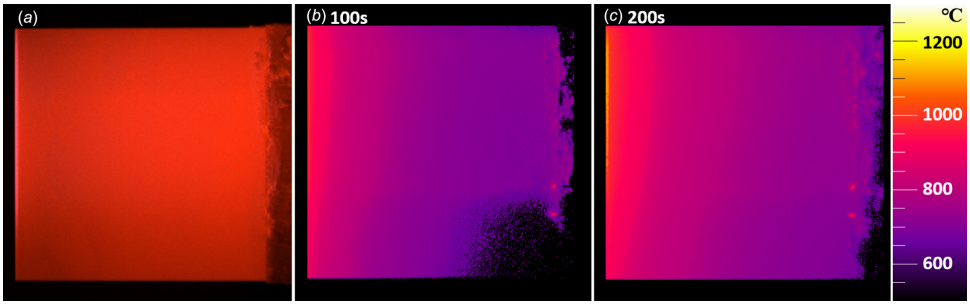

Figure 2.7: Measured thermal image (a) of the model at high temperatures and temperature distribution of the ceramic model at in the plasma flow at 100 s (b) and 200 s (c) using the sub-pixel technique described by Fu. Image taken from Fu [5].

2.2.4 Multi-band pyrometry

Finally, distinction between multi-wavelength and multi-band pyrometry is required to understand the multi-band plenoptic camera. Multi-wavelength pyrometry assumes that the recorded wavelength bands are narrow enough that discrete wavelengths for spectral measurements ($\lambda' = \lambda''$ from Equation 2.9) can be assumed [1, 29]. Multi-band pyrometry cannot assume monochromatic acquisition. The previous equations for mutli-wavelength are not valid for multi-band pyrometers. Multi-band pyrometry follows a series of equations given by Equation 2.9, where $\lambda' \neq \lambda''$. The number of equations, n, equals the number of spectral bands that are recorded. There is no analytical solution to Planck's equation for a band of wavelength ($\lambda' - \lambda''$) as explained by Modest [30]. Therefore, a numerical integrator like Simpson's method is required to solve. One issue found for multi-band pyrometry is the difficulty in selecting an emissivity model. The simplest model that is used in other pyrometric techniques is the gray body assumption.

There have been many techniques developed for multi-band pyrometry [29, 6, 31, 32]. Araújo [29] developed a multi-band pyrometer that captured twelve wavelength bands in the range of 2-60 μm. It was found that the largest decrease in uncertainty was when the number of bands used went from 2 to 3. Anything greater than 4 only negligibly reduced uncertainty. It was also found that some multi-band wavelengths resulted in an increase in uncertainty, showing the importance of selecting wavelength bands. However, the temperature and large wavelength range in the infrared spectrum could have influenced the uncertainty. Fu *et al.* [32] showed that multi-band pyrometry is sometimes the optimum method compared to multi-wavelength. Accuracy of multi-band methods can be very sensitive to bandwidth range. Fu *et al.* [33] developed the concept of measurement coordinates for multi-band pyrometry, which described how solutions of temperature and emissivity vary in measurement coordinates. Fu suggested it would help optimization of multi-band systems.

Gao *et al.* [6] developed a fiber-optic four band pyrometer to measure temperature of an oven at a range of 700 K to 1200 K, and eliminated effects of reflected radiation with unknown

emissivity. The fiber optic pyrometer had four recorded spectral bands between 1000nm-2000nm as shown in Figure 2.8. Each sensor captures a spectral band between 100nm to 200nm wide to improve the SNR compared to thinner bands. Gao does not disregard $\Phi_a(\lambda)$. Gao used a Multi-objective Genetic Algorithm to find the equivalent wavelengths for each of the four detectors. The experiment consisted of a specimen inside an oven, with K-type thermocouples for a temperature comparison. The ambient tempreatures were much higher compared to surface temperatures. It was shown to have measurement error within 0.44%, which is improved accuracy compared to traditional methods.

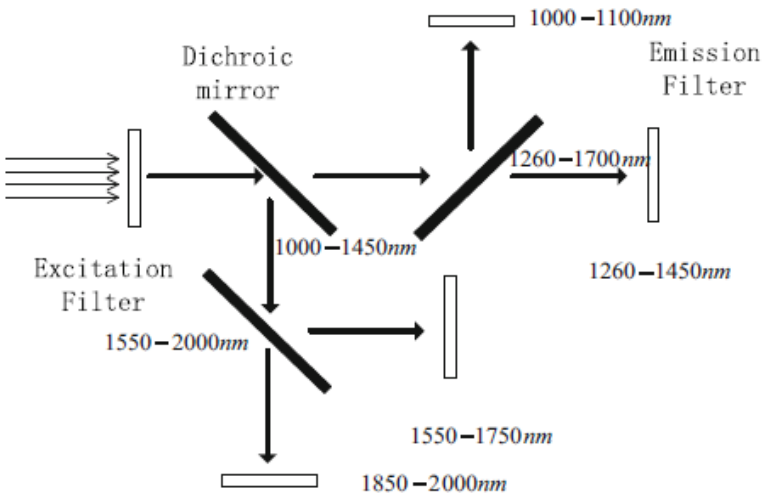

Figure 2.8: Schematic of the multiple sensor and dichroic mirror placement for the pyrometer designed by Gao. Taken from Gao [6].

Fu *et al.* [7, 8] developed a technique using a commercially available color camera using a Bayer style filter to capture red, green, and blue colors to determine temperature. Each wavelength channel was first used to simulate single-color measurements, which was able to calculate a temperature without any other hardware. A three-color method that separated emissivity modeling from temperature measurement was developed to avoid uncertain integral computations, making it more suitable for actual object measurements. In the earlier paper by Fu *et al.* [7], the spectral sensitivity at each channel spanned over 100nm as shown in Figure 2.9. In [7], Fu applied a filter to narrow the spectral response curves for red and blue as shown

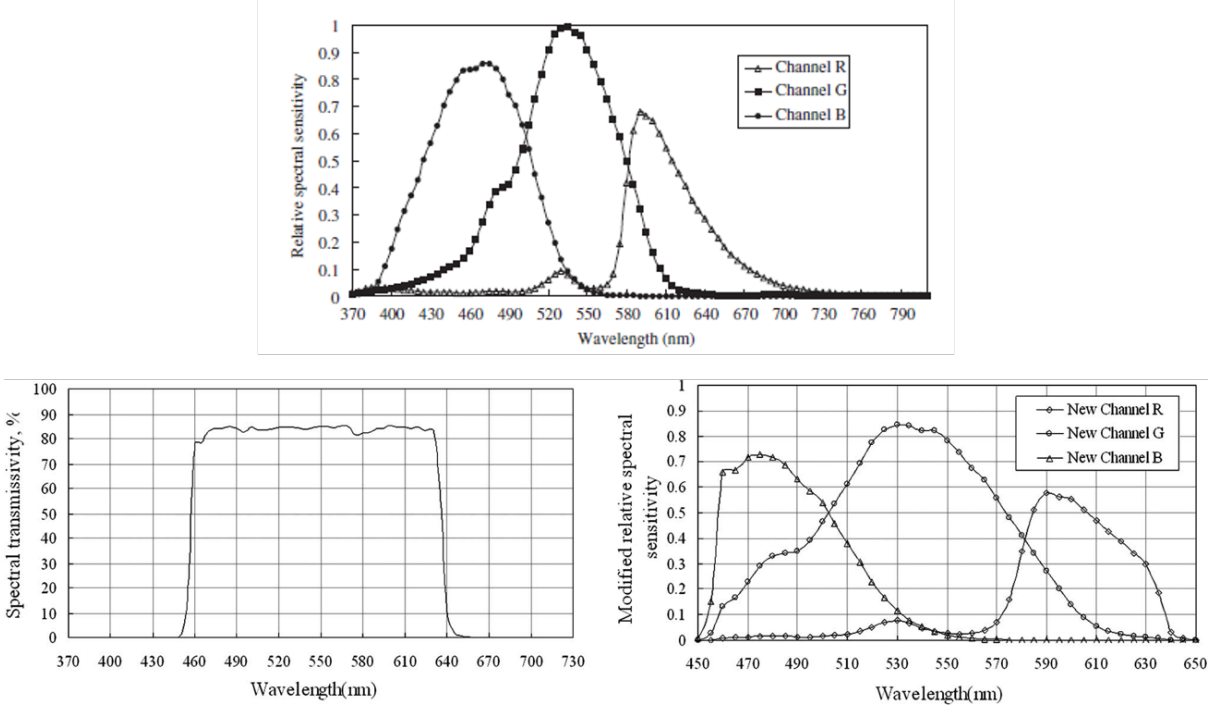

Figure 2.9: (Upper) Relative spectral band sensitivity curves for red (R), green (G), and blue (B). (Lower left) filter transmissivity graph, and (lower right) spectral response of R,G,and B after the filter is applied. Taken from Fu [7] and [8], respectively.

in Figure 2.9. Narrowing the spectrum bandwidth for red and blue made the linear emissivity model more suitable, and reduced the numerical uncertainty of the wavelengths, increasing temperature sensitivity.

2.2.5 Spectral pyrometry

Another technique that is used for temperature measurements is called spectral pyrometry. There are regions of the emission spectrum of an object that will be of similar shape to the spectrum of a blackbody, which allows temperature to be found from intensity distribution. Spectral pyrometry differs from multi-wavelength/band by the number of wavelengths used, where typically 4 or less wavelengths are used for multi-wavelength. The number of wavelengths along with not requiring a emissivity model to solve for temperature defines spectral pyrometry. Spectral pyrometry does this by minimizing the effects of emissivity in the equation for temperature measurements, which has plagued many of the techniques described earlier. Many of the other techniques have had to experimentally measure the emissivity, which was used to determine temperature. The concept behind the spectral pyrometry technique has been

widely used in gas-discharge plasma physics, which uses the slope of a straight line created by linearizing the Maxwellian electron-energy distribution equation as explained by Magunov [9].

Similar to how a plasma physics technique linearizes the Maxwellian electron-energy equation, spectral pyrometry linearizes Wien's distribution law. Manipulating Equation 2.2 gives the follow equation:

$$\ln(\lambda^5 I) - \ln(\varepsilon C_1) = -\frac{C_2}{\lambda T} \tag{2.16}$$

where $C_1 = 2hc^2$ and $C_2 = \frac{hc}{k}$. The derivation of the linearized Wien equation is shown in Appendix A.1. This equation can be used if the camera records the light intensity in Watts per squared centimeter (W/cm^2). Many of the current sensors are a charge-transfer photodetector, which include charged couple device (CCD) and complementary metal-oxide-semiconductor (CMOS). Charge-transfer photodetectors record the amount of photons that interact with a pixel for an exposure time. IR image sensors would also work. Equation 2.17 is the relationship that converts the number of photons (n) that interact with a pixel to the light intensity (I),

$$I = n(h\nu)\Delta t \tag{2.17}$$

where ν is the frequency of light. Using Equation 2.17 to convert Equation 2.16 gives [9]:

$$\ln(\lambda^4 n) - \ln\left(\frac{\varepsilon C_1}{hc}\right) = -\frac{C_2}{\lambda T} \tag{2.18}$$

Equation 2.18 is Wien's spectrum that can be represented in y = mx + b form, where x = $\frac{C_2}{\lambda}$, y = $\ln(\lambda^4 n)$, and b = $\ln(\frac{\varepsilon C_1}{hc})$. If the body can be represented as a gray body, the effect of emissivity change with temperature only causes a parallel shift of the linear Wien curve. A parallel shift does not change the slope of a curve, therefore, temperature can be found using the slope of the linearized curve. Even without the gray body assumption, the effect of varying spectral emissivity is a logarithmic dependence, which is much weaker than I(λ) as explained by Magunov [9].

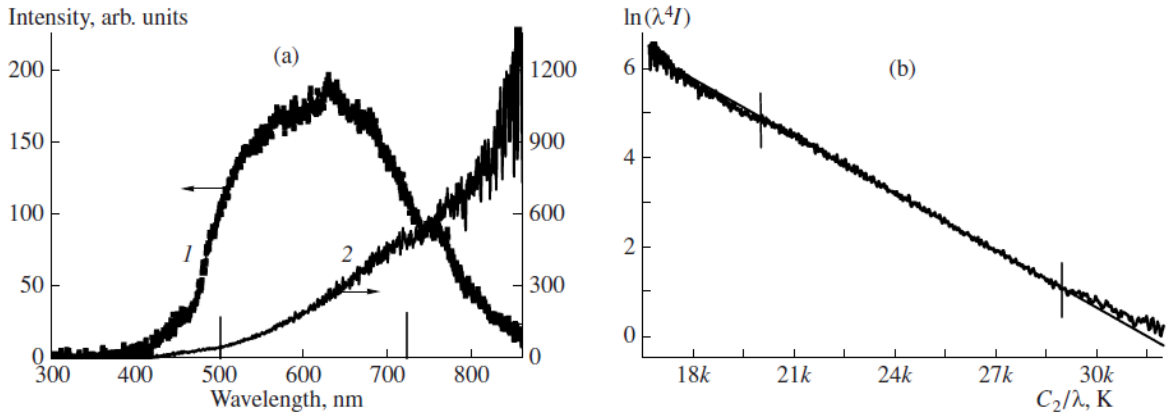

Figure 2.10: (a) Captured emission spectrum of a chemical reaction of (1) before and (2) after correction at temperature of T = 2336 K. (b) Captured spectrum that is converted to Wien coordinates. Adapted from Magunov [9].

Figure 2.10 shows an example conversion from recorded intensity to Wien coordinates for a chemical reaction. The conversion from 1 to 2 was conducted because the sensor used by Magunov had large varying spectral sensitivity, which is not required for all sensors. Wien coordinates is a useful technique, which can be used in the "Wien region" as explained by Magunov [9]. High accuracy can be achieved when wavelengths 3 to 4 times shorter than $\lambda = C_2/T$ are used, which includes λ_{max}. When using the visible spectrum, the Wien region stays in the visible range until about 8000 K.

2.3 Spectral imaging

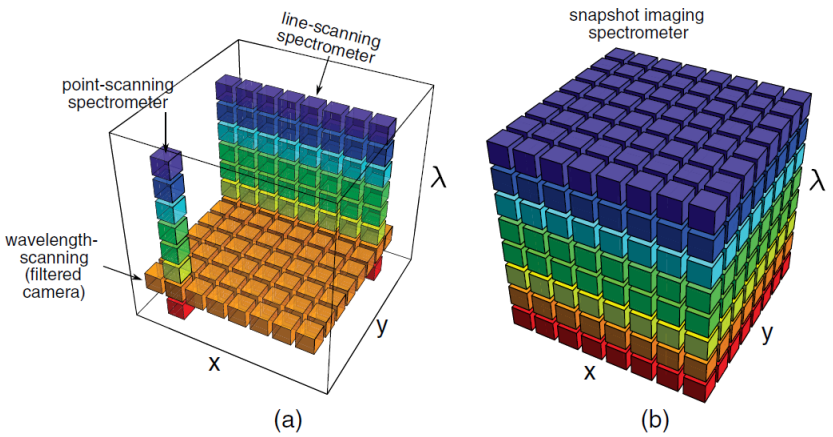

Figure 2.11: Depiction of how the 3D data cube is sampled during a capturing period of the detector for (a) scanning and (b) snapshot imagers. Taken from Hagen and Kudenov [10].

Now that it is known how different pyrometry techniques use wavelength information, an understanding of how pyrometers capture wavelength information is required. A sensor that samples the spectral content of a scene is known as a spectral imaging device. Two main spectral imaging devices are known as spectral scanning systems and spectral snapshot cameras. A comparison between the sampling methods of the two scanning systems are shown in Figure 2.11. The data cube is a three-dimensional (3D) dataset having to two spatial coordinates (x,y) and a wavelength (λ) coordinate. Scanning systems capture a portion of the data cube for one integration period of the sensor, and the amount sampled depends on the scanning device. Three of the main types of scanning spectrometers are point-scanning, line-scanning, and wavelength-scanning. Snapshot systems are ones that capture the entire data cube during one integration period of a detector. Since sensors are two-dimensional (2D), the datacube is sampled in multiple slices and combined during post-processing. Generally, snapshot systems capture light more efficiently compared to scanning devices as described by Hagen and Kudenov [10]. In this section, spectral imagers typically used for pyrometry will be discussed.

One type of snapshot spectral camera used for pyrometry is a multi-spectral beamsplitter that has several examples shown in Figure 2.12. A beamsplitter is one which allows a range of wavelengths to pass, while reflecting another range. Consequently, most beamsplitter designs require several sensors to capture light from the scene. Another design is shown in Figure 2.12(d) where a beamsplitting stack is created by offsetting filters at an angle. These filters create a grating effect allowing one sensor to capture wavelengths on separate portions of a single sensor. Beam splitting systems have the ability to get high resolution snapshot wavelength images of the same scene but can be very complex to design. It can be very difficult and expensive to increase the number of wavelengths past 4 or 5 because of increasing complexity of path lengths, sensors, and beamsplitters as described by Hagen and Kudenov [10].

Another snapshot spectral camera that is utilized for pyrometry is spectrally resolving detector arrays (SRDA). An example of a SRDA system is shown in Figure 2.13a. These systems consists of an array of pixel-level-filters, which can create a very compact system compared to many other designs. A version of the SRDA is called the Bayer-style filter-array, which consists of a certain pattern of red, green, and blue filters. The Bayer-style filter is used

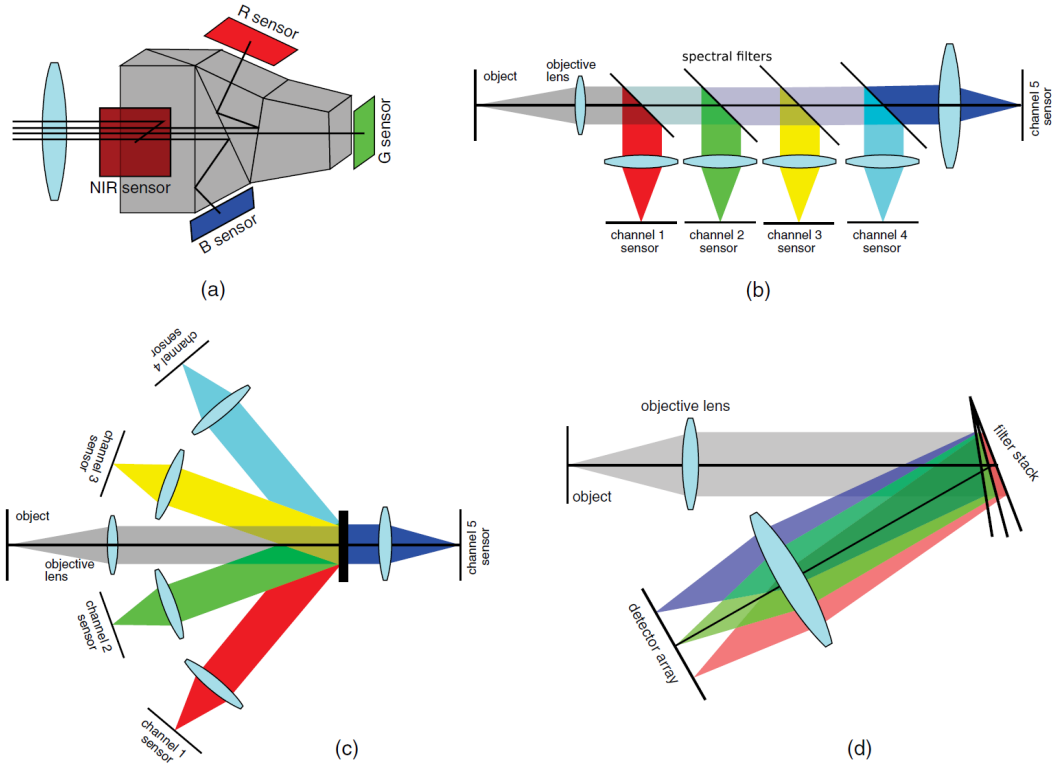

Figure 2.12: Common beamsplitter configurations, which include (a) monolithic beamsplitter blocks, (b) a sequence of spectral filters/beamsplitters, (c) a volume hologram optical element splitter, and (d) a stack of tilted spectral filters. Taken from Hagen and Kudenov [10].

in most consumer color cameras because of the compact size and ability to mimic the way color displays and human visual systems operate. One issue that arises for a SRDA design is the difficulty to produce highly specific designs and difficulty changing spectral filters. SRDA systems also have a disadvantage of being spatially band limited to the Nyquist limit, that if not met, will cause aliasing of color images [10].

Figure 2.13b shows an example of a scanning spectral camera known as a filter wheel. The filter wheel has a number of filters that can be rotated in front of a camera to capture a distinct wavelength for one integration period. The filter wheel can vary in size depending on the number of filters that are needed. Filter wheels are one of the simpler designs to implement and color filters can be easily exchanged. However, the design is a scanning technique, therefore, wavelengths are imaged at different sensor integration periods. For dynamic environments with varying colors, the color images could not be related since the scene has changed. Lack

of snapshot capability can cause errors in pyrometry for fast processes including flames and additive manufacturing.

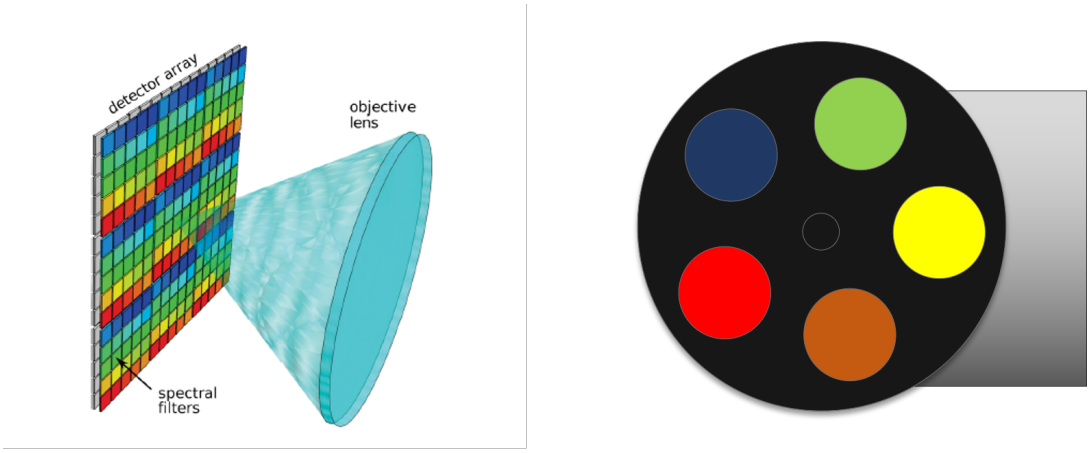

Figure 2.13: (a) SRDA example layout with a pixel-level filter array, taken from Hagen [10], and (b) a filter wheel example with 5 different color filters.

Finally, the current work focuses on the snapshot system that Hagen [10] referred to as a multiaperture filtered camera (MAFC), where an example is displayed in Figure 2.14. MAFC consists of a main lens, lenslet array, and sensor. The lenslet array captures sub-images from the aperture. Three different designs are presented by Hagen, one with filters at the detector level (c), one at the lenslet array level (b), and one with filters at the aperture plane of the main lens (a). MAFC can be compact, similar to a SRDA design. One of the first MAFC was developed in 2004 by Shogenji *et al.* [34], which had the filter array at the microlens level. Each microlens in the array had a corresponding spectral filter that was placed in front. A design with an optical filter placed at the main lens was first suggested by Levoy [12], and then implemented by Horstmeyer *et al.* [35]. For this design, the microlens array is placed at a focal length distance away from the sensor. Each microlens produces a micro image of the filter array. Another example of a filter placed at the main lens is developed by Mitchell and Stone [36], which uses a linearly variable filter at the main lens, similar to the design from this thesis. Yu *et al.* [37] analyzed color demosaicing methods for a colored plenoptic camera, which is a form of a MAFC with the Bayer style filters at the sensor plane.

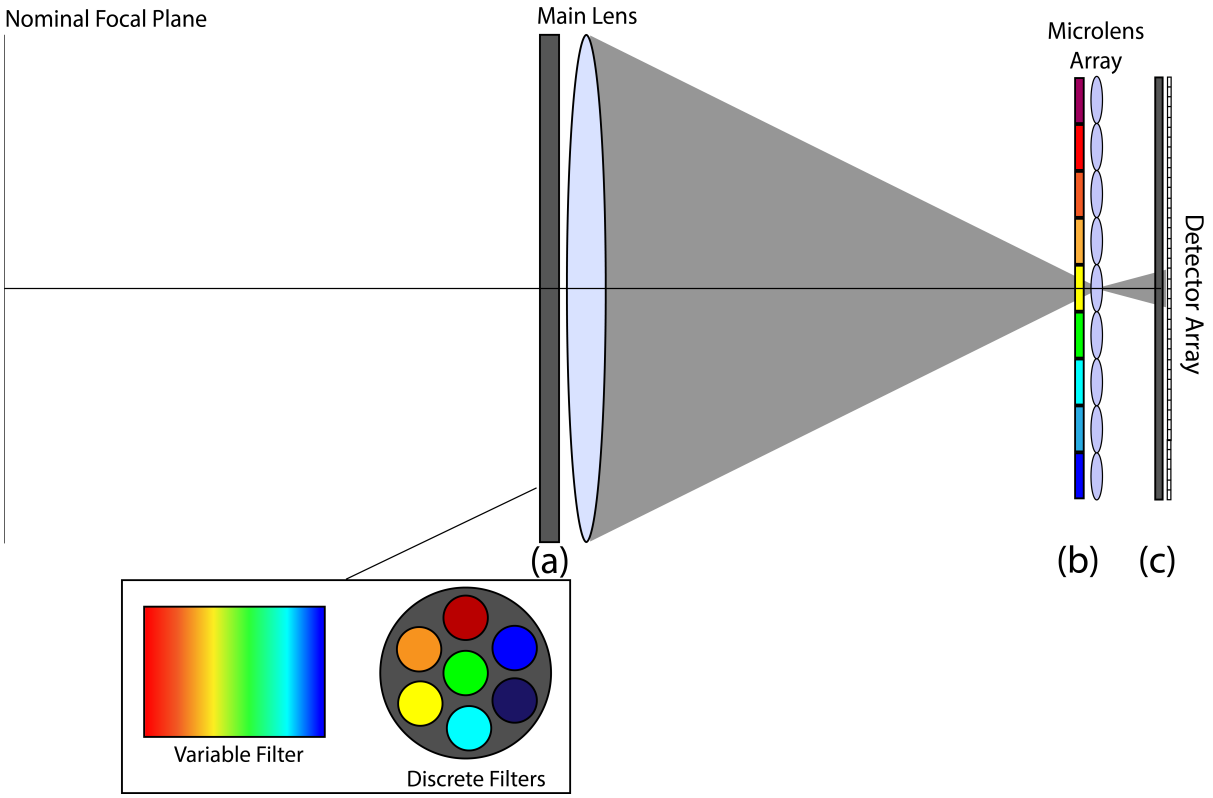

Figure 2.14: System layouts for a multiaperture filtered camera (MAFC), with configurations inlcuding (a) a filter at the aperture plane, (b) filters at the lenslet array plane, and (c) filters at the detector array plane. Two filter designs at (a) are depicted with discrete filters as described by Fahringer [11] and a variable filter as first described by Levoy *et al.* [12].

The first known implementation of MAFC for pyrometry was done by Danehy *et al.* [3]. Figure 2.15 shows the three bandpass filter configuration that was placed in front of the aperture plane to get temperature measurements of an oven cooling off. The number of wavelengths and design of the system was progressed by Fahringer *et al.* [11], where he increased the design to fit seven color filters, similar to the design shown in Figure 2.14. Fahringer *et al.* was able to design a system that placed filters approximately at the aperture plane. This design allows specific wavelengths to be easily located on the sensor due to their separation. However, the filter mount covers portions of the main lens, which causes unusable areas of the microlens. Further discussion about a MAFC system with a variable filter at the aperture plane is discussed in the following chapter.

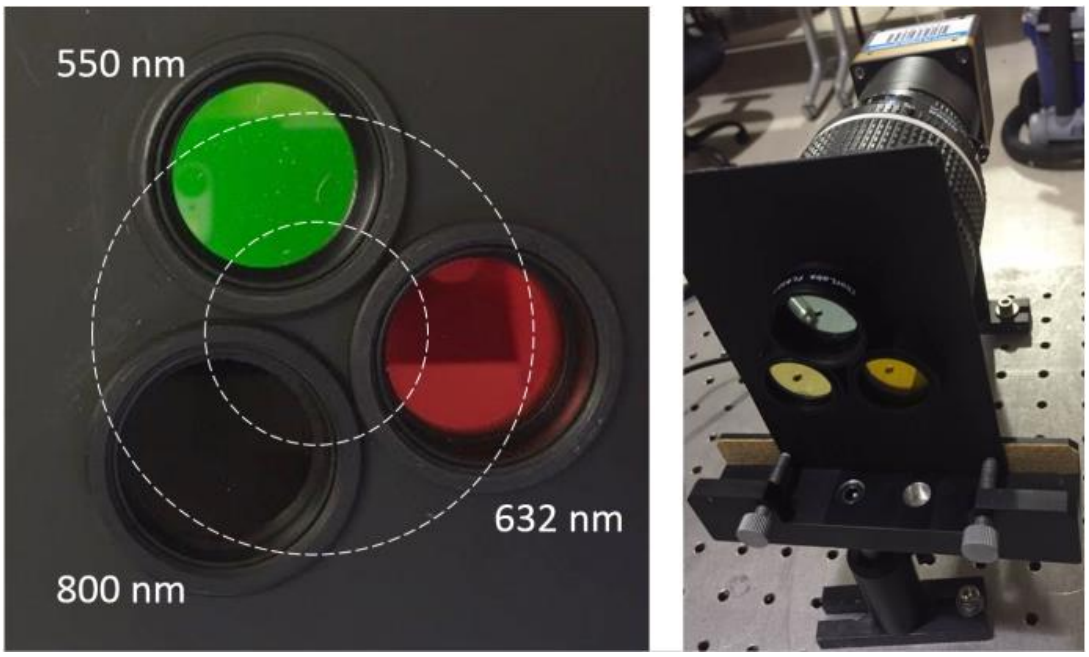

Figure 2.15: (Left) Configuration of three bandpass filters used by Danehy [3]. (Right) Image showing the location of the bandpass filter mount in front of the main lens of a plenoptic camera. Image is taken from Danehy [3].

Chapter 3

Light Field Imaging

3.1 Background

The origins of sampling the angular and spatial information of light came from Lippmann in 1908 [38]. It was not until 1936 when Gershun [39] coined the term *light-field* referring to the specifications on how light rays travel through every point in space. Adelson and Bergen [40] created the plenoptic function, which describes the light field with seven parameters. The parameters include the different directional angles (θ,ϕ), spatial coordinates (V_x, V_y, V_z), time (t), and wavelength (λ) of the light rays. The plenoptic function, given in Equation 3.1 defines the light rays that are emitted and reflected from bodies.

$$P = P(\theta, \phi, \lambda, t, V_x, V_y, V_z) \tag{3.1}$$

This function describes the light rays, but does not give a way to sample the light field. Similar to Lippmann's method of capturing a light-field, Adelson and Wang [41] described a way of using miniature pinhole cameras placed at the image plane of a main lens to sample the light-field. Adelson then constructed a light-field camera using a lenslet array to create depth maps of images using sampled spatial (V_x, V_y, V_z) and angular (θ, ϕ) coordinates. The camera was termed as a plenoptic camera, which was able to sample 4 dimensions of the light-field (V_x, V_y, θ, ϕ).

Figure 3.1 shows the two plane parameterization of a light ray. Levoy and Hanrahan [13] described a way to parameterize light rays using points on two parallel planes, assuming light travels in a straight line through the volume. Levoy explained that the radiance remains constant along the ray, assuming that nothing is blocking the ray. Two plane parameterization

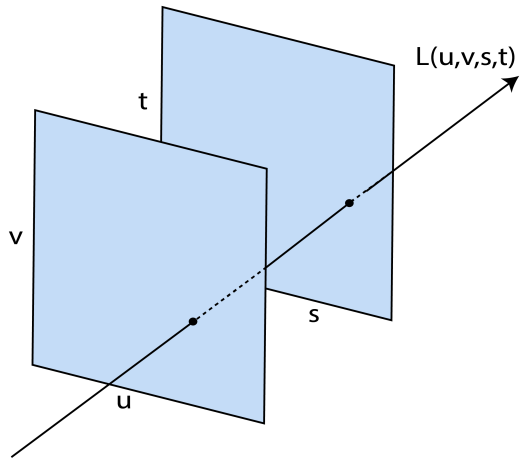

Figure 3.1: Two plane parameterization of a light ray with a pair of two points. Adapted from Levoy [13].

is useful when light is sampled in four dimensions. The light field is now a function given by $L(s,t,u,v)$, where the points (s,t) are on one plane and (u,v) points on the other. These two planes have a known distance, which allows angular information to be fully defined from the spatial locations on both planes.

A simple schematic of how each pixel corresponds to a portion of the main lens is shown in Figure 3.2. Each line corresponds to an edge of a pixel, showing the region of the aperture plane a pixel captures. Traditional imaging needs to be understood before we cover how plenoptic cameras are able to capture the spatial and angular information of a light-field. In a traditional camera, the main lens focuses light onto the sensor, which records intensity regardless of a light ray's direction. Therefore, traditional imaging averages light intensity over a range of angles. A plenoptic camera samples the light-field by discretizing the main lens using a microlens array placed between the main lens and the sensor. Adelson and Wang created a complex version of the plenoptic camera using a diffuser, a main lens, a field lens, lenslet array, ground glass, and a relay lens. Ng [42] further advanced the plenoptic technology by creating the first hand-held plenoptic camera. This consisted of a regular camera with a lenslet array placed next to the sensor.

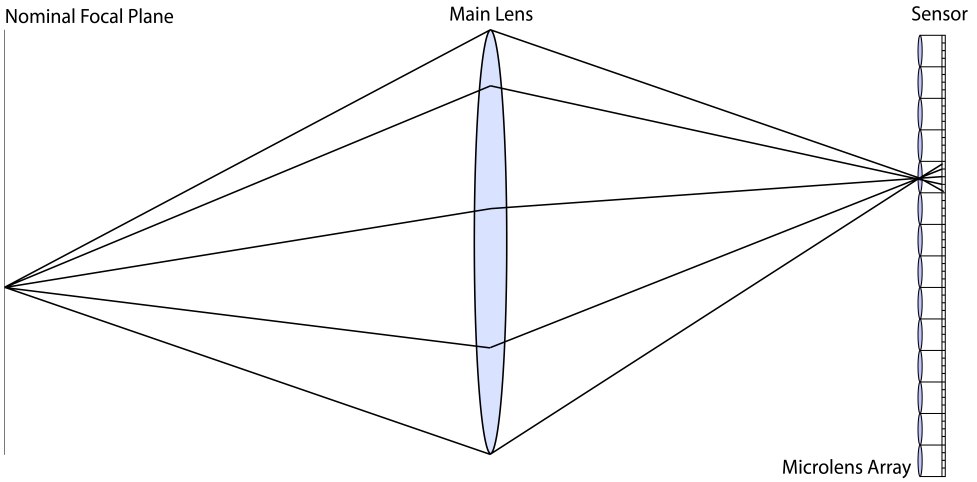

Figure 3.2: 1D schematic of a plenoptic camera. Each line through the main lens corresponds to edges of a pixel, showing the discretization of the main lens.

3.2 Capabilities

Figure 3.2 shows the conceptual design for plenoptic cameras, with the microlens array next to the sensor, similar to the design by Ng *et al.* [42]. In this design, the main lens coordinates correspond to the (u,v) plane and microlens plane to the (s,t) plane of the Levoy's two plane parameterization. The plenoptic camera introduces two main capabilities, perspective shifting and computational refocusing, which comes from the discretization of the main lens.

A visualization of perspective image generation is displayed in Figure 3.3. A perspective image is a rendering of a synthetic image compiling a particular (u,v) coordinate for all (s,t) locations. In general, the image produced will correspond to imaging through a small portion of the main lens for a specific (u,v) discretized coordinate. The perspective image will have a larger depth of field because each pixel samples a smaller portion of the lens, which effectively mimics a pinhole aperture. Perspective image compilation equation is given by Equation 3.2.

$$I_{perspective}(s', t') = L(u_p, v_p, s', t') \tag{3.2}$$

In this equation u_p and v_p are one location on the (u,v) plane. Perspective image resolution is determined by the number of microlenses in the lenslet array. The resolution of the sensor specifies the angular resolution or number of perspective views.

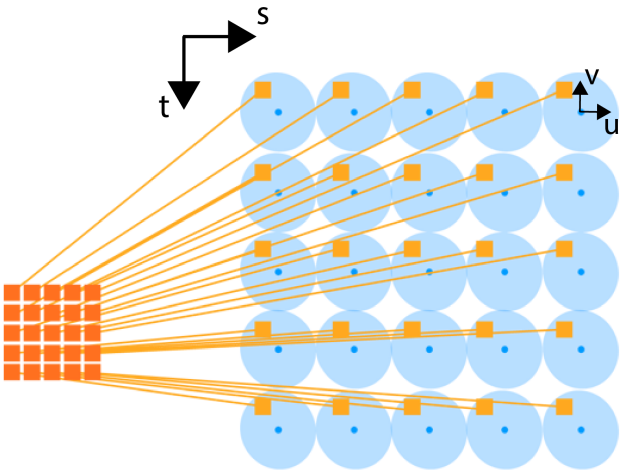

Figure 3.3: Diagram of perspective view generation algorithm.

Computational refocusing is another attribute of plenoptic imaging, where the focus of the image can be changed to different planes in object space by creating synthetic image planes. Figure 3.4 shows the relationship between synthetic planes that refocusing uses to trace light rays to a new synthetic plane. The nominal focal plane is the distance, s_o, from the camera where light from a point will be captured by a single point on the (s,t) plane. When all light rays emitted from that point in the nominal focal plane are integrated, the point will appear sharp and in focus. Points not within the nominal focal plane will be spread out over several microlenses depending on depth. If light rays are traced to a new synthetic plane where they intersect at a single (s',t') location, then the point of emission will be in focus in the new synthetic image. The new virtual image plane is at depth, s_i' = αs_i, where s_i is the original sensor plane and α is a scaling factor. The creation of a refocused image is given by Equation 3.3 [42].

$$E(s',t') = \int\int L'\left(u',v',u' + \frac{s'-u'}{\alpha}, v' + \frac{t'-v'}{\alpha}\right) du'dv' \tag{3.3}$$

Perspective shift and computational refocusing can be very powerful tools for the research community. Figure 3.5 shows two perspective images from the left and right side of the aperture, and two images that are focused on the back card and front cards, independently. All of these images originate from the same raw plenoptic image. Generally, to get images at different angles (perspectives), it would require multiple conventional cameras or sensors moved

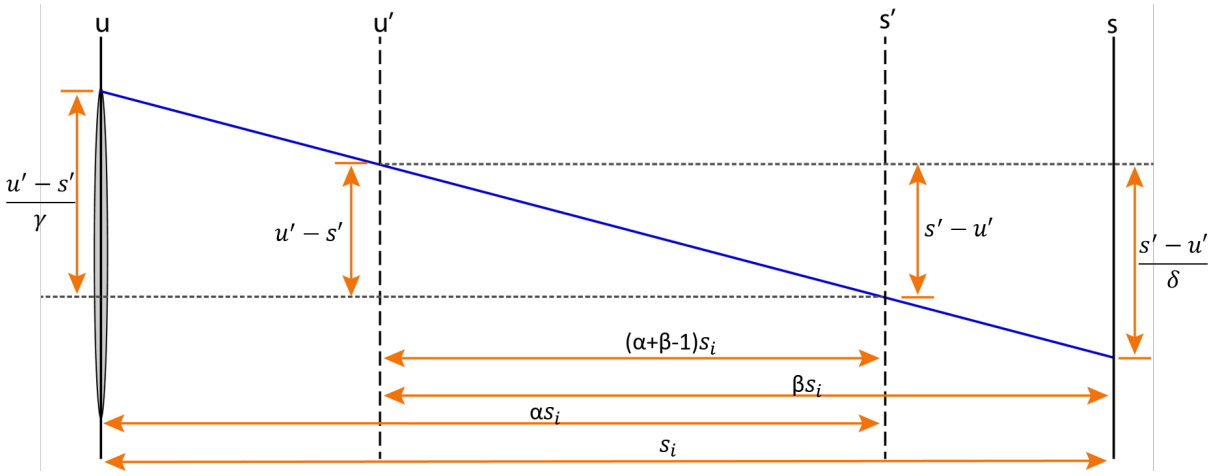

Figure 3.4: Schematic of synthetic light field plane relationships.

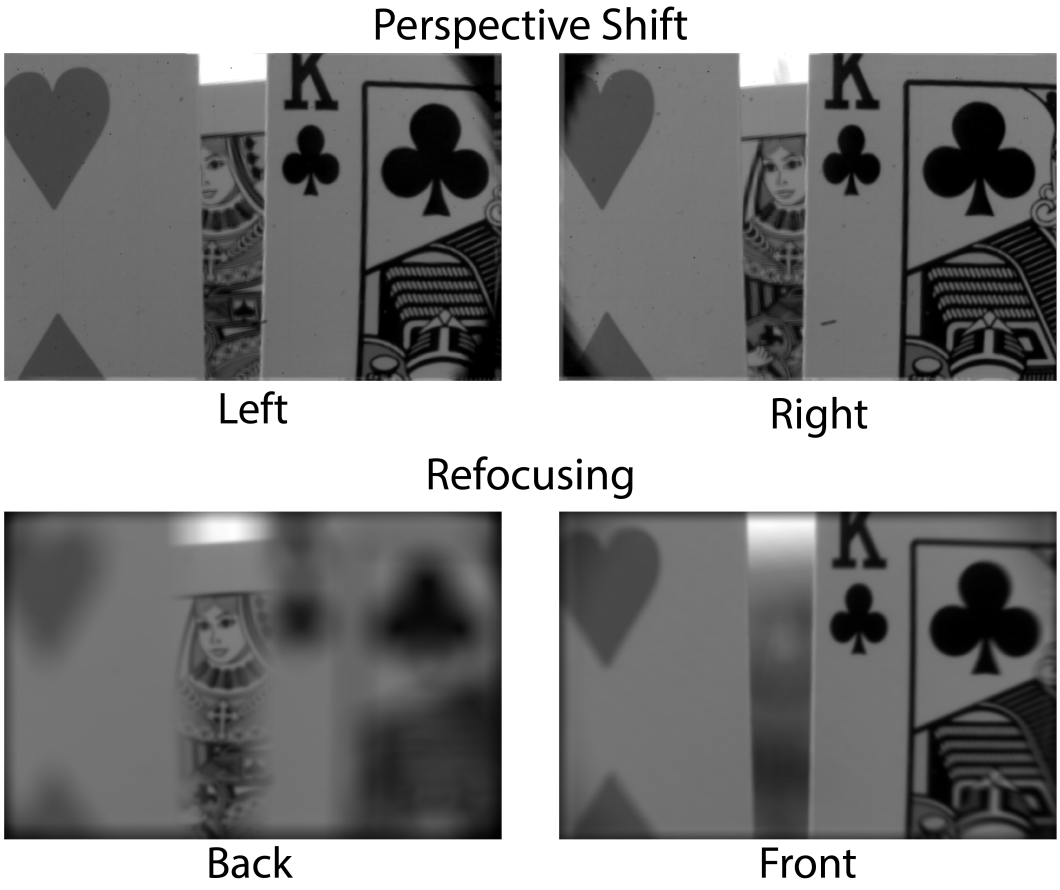

Figure 3.5: Top set of images shows the capability of generating perspective images from the left and right sides of the aperture. Bottom set of images shows refocused images on both the back and front cards.

between frames, while the plenoptic camera captures angular information in one frame from a single aperture and sensor. In the past, the Advanced Flow Diagnostic Laboratory (AFDL)

has developed the plenoptic camera for an assortment of aerospace diagnostic applications. The plenoptic camera has been utilized for particle image velocimetry (PIV) with both a single and multiple plenoptic cameras [43, 44]. Plenoptic PIV has been applied to many applications including leading-edge vortex development on a flapping wing, shock-wave boundary layer interaction [45], and flow over a hemispherical particle bed [46]. Another technique developed is plenoptic background orientated Schlieren [47]. Plenoptic also allows the ability to determine object size and depth due to the angular information, which has been used for particles [48]. Recently, a new modular high-speed plenoptic camera has been developed increasing research opportunities [49].

3.3 Multi-band plenoptic imaging

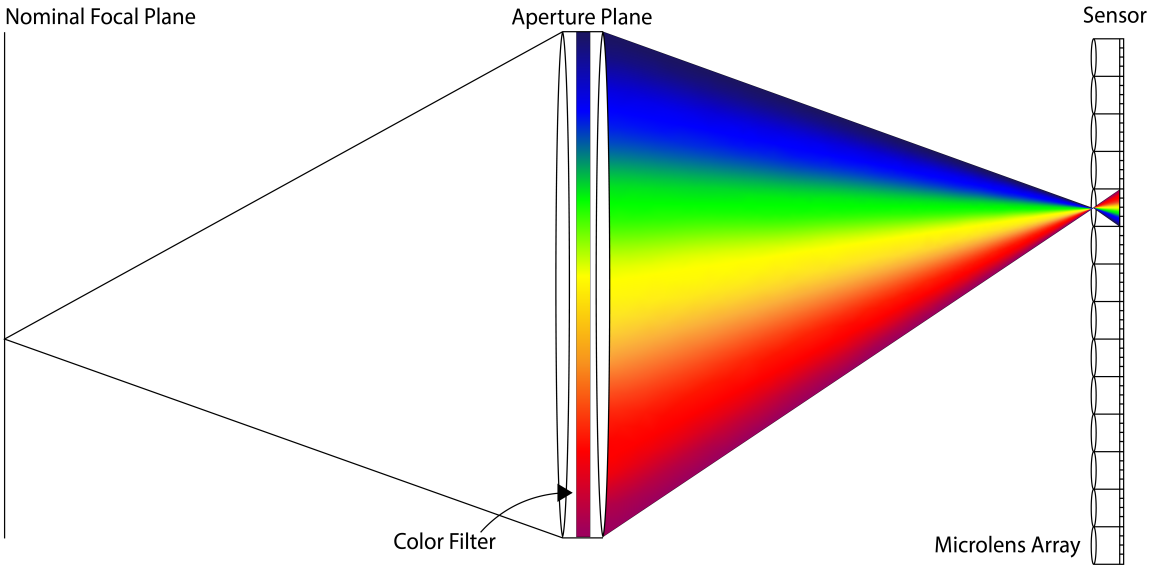

Figure 3.6: 1D schematic of the multi-band plenoptic camera that uses a rainbow filter.

A multi-band plenoptic camera is a combination of the earlier described plenoptic camera and a color filter or filters. A diagram for the multi-band plenoptic camera with a rainbow filter at the aperture plane is shown in Figure 3.6. Each microlens creates a micro image of the aperture plane, therefore, placing a filter at the aperture plane will produce micro spectra across the image plane. Angular information typically captured by the plenoptic camera now has wavelength encoded on some or all of the angular information. The multi-band plenoptic

camera creates a way to sample the wavelength portion of the light-field. With the color filter, each perspective image corresponds to a certain wavelength band or “color”.

Even though a rainbow filter is depicted in Figure 3.6, similar to Figure 2.14, discrete color filters can be placed at the aperture plane. Figure 3.7 displays microlens images of three filter and seven filter configurations, designed by Danehy *et al.* [3] and Fahringer *et al.* [11], respectively. Each filter has a region of (u,v) points that captures light intensity of the corresponding wavelength. The more filters that are added, the fewer (u,v) points that will capture a particular wavelength. A linearly variable filter will have a continuous function of (u,v) points. A particular wavelength will be a sub-pixel level location. The maximum number of wavelengths that can be captured will depend on the number of (u,v) points, for both discrete filters and the variable filter.

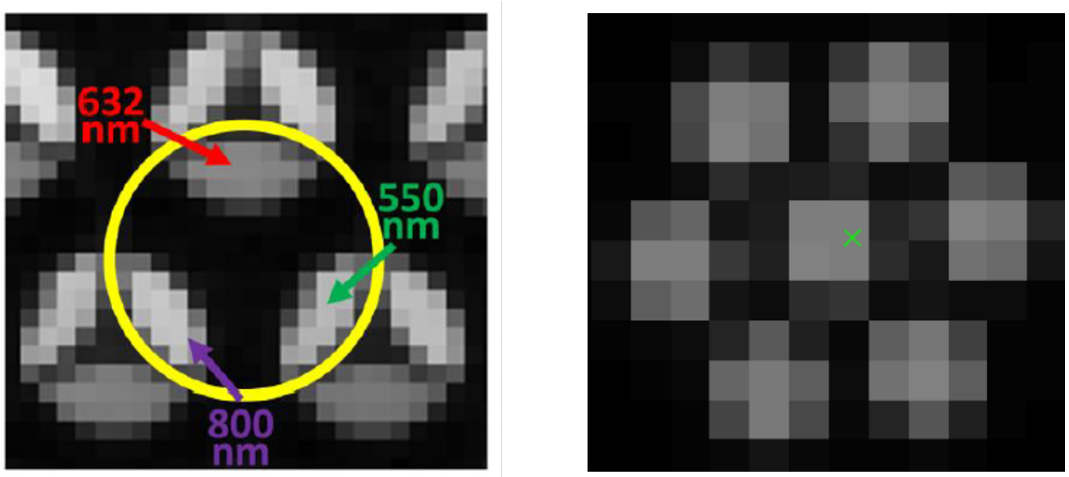

Figure 3.7: (Left) Microlens image of a three filter design by Danehy, where the edge of the microlens is shown by the yellow circle. Taken from Danehy *et al.* [3]. (Right) Microlens image of the seven filter design by Fahringer. Taken from Fahringer [11].

Figure 3.8 shows perspective images for three different wavelength bands using the rainbow filter. The perspective shift can be seen by the second duck’s eye being visible in the blue image, but being completely covered in the red image. The scientific duck, however, does not move in the perspectives because it is located at the nominal focal plane. Even though only three colors are shown, the number of wavelength bands is determined by microlens diameter. However, the number of wavelengths for the discrete filter designed by Fahringer *et. al.* [11] is determined by the number of filters as presented in Figure 3.7.

Figure 3.8: Multi-band perspective shift of rubber ducks at different depths. The white circle is placed at the same location on the images to show the movement of the ducks.

3.3.1 Plenoptic depth of field

One important note is that for a spectrum to be captured by one microlens, the point in space must be within the depth of field (DOF) of the nominal focal plane. Figure 3.9 shows the limits of the DOF of the nominal focal plane. As objects move away from the nominal focal plane, the image gradually becomes blurred. For plenoptic imaging, increasing distance causes the light rays to be captured by surrounding microlenses. The depth of field can be found using the diameter of the main lens (d_a), object plane distance (s_o), and the circle of confusion distance in object space (c_o). Equation 3.4 and Equation 3.5 shows the near and far depth limits of the nominal focal plane. The DOF can be found from the difference between of the near and far depth limits as shown by Equation 3.6.

$$s_{near} = \frac{d_a s_o}{d_a + c_o} \tag{3.4}$$

$$s_{far} = \frac{d_a s_o}{d_a - c_o} \tag{3.5}$$

$$DOF = s_{far} - s_{near} \tag{3.6}$$

DOF is an important limitation for the current multi-band plenoptic camera. The main takeaway from this paragraph should be that the current work's algorithm, described in Chapter 5, must have the target surface/object within the DOF of the imaging system in order to ensure accurate temperature measurements. This is because the current method assumes that

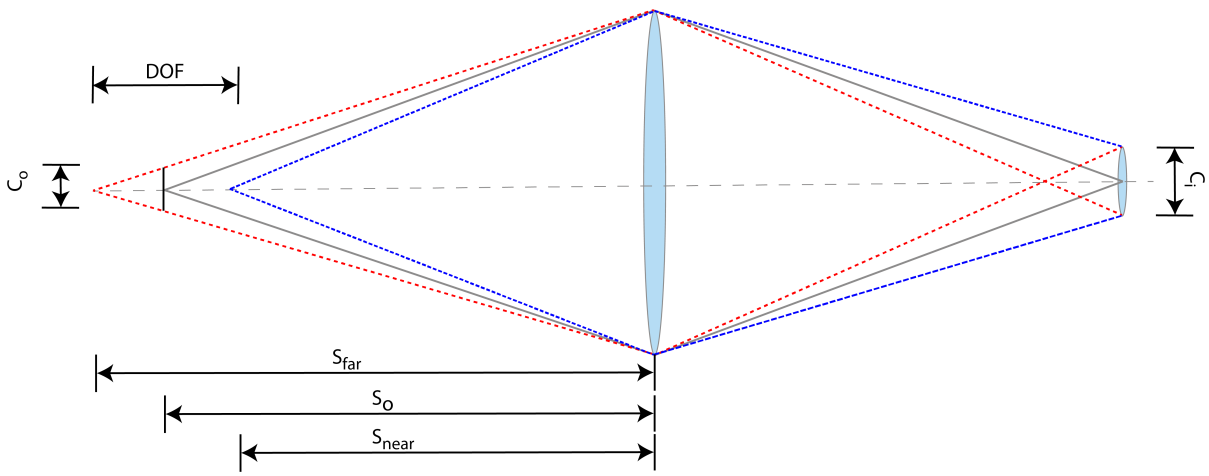

Figure 3.9: Schematic of the different lengths that is required to calculate DOF of a multi-band plenoptic camera. Light from the nominal focal plane is represented by the gray lines.

the spectrum captured by a microlens corresponds to a point in object space. A microlens captures light from one point as long as it is within the DOF. When outside of the DOF, the light from a point spreads beyond one microlens. Therefore, that point outside of the DOF will have different portions of the emitted spectrum captured by separate microlenses. This can be shown assuming the circle in Figure 3.8 is one microlens. The blue spectrum corresponds to the second duck's eye, the yellow is a combination of the second and third duck, and then the red is only the front duck. Therefore, that circle/microlens's spectrum has a combination of both the front and second duck. When using an out of focus spectra for temperature measurements, the combination of spectra will give errors unless properly handled. For objects located outside the DOF, the temperature measurements may be inaccurate. Future work will investigate algorithms that combine depth and spectra measurements to resolve the DOF limitation.

Chapter 4

Multi-band Plenoptic Camera Design

This section covers the design progression of the multi-band plenoptic camera developed by AFDL. The multi-band camera implementation combines an arrangement of lenses, a linearly variable wavelength filter (rainbow filter), and a plenoptic camera. The multi-band module was designed for the current version of the plenoptic camera developed by AFDL as shown in Figure 4.1. The plenoptic camera used for measurements is an Imperx Bobcat 6640, which has a custom bracket developed by AFDL to house the microlens array approximately one microlens' focal length distance from the sensor. Camera specifications along with the current multi-band module are presented in Table 4.1. To reduce image artifacts associated with placing the filter outside of the camera as described by Fahringer *et al.* [11], a two lens configuration was designed to position a filter approximately at the aperture plane of the camera.

Table 4.1: Current multi-band plenoptic camera parameters.

Parameter	**Value**	**Parameter**	**Value**
Camera	Imperx Bobcat 6640	Pixel pitch	0.0055mm
Microlens pitch	0.077mm	Number of pixels: X-direction	6600
Microlens focal length	0.308mm	Number of pixels: Y-direction	4400
Microlens f-number	4	Lens 1 focal length	500mm
Number of microlenses: X-directions	471	Lens 2 focal length	75mm
Number of microlenses: Y-direction	362	Wavelength filter range	300nm - 850nm
Microlens layout	Hexagonal		

Figure 4.2 shows a two lens configuration that allows for flexibility in main lens focal length. Selection of two lenses depends upon a desired working distance, magnification, and microlens image size. Lens 1, called the collection lens, determines the working distance and magnification. An effective focal length for the two lens system is given by Equation 4.1.

$$\frac{1}{f} = \frac{1}{f_1} + \frac{1}{f_2} - \frac{d}{f_1 f_2} \tag{4.1}$$

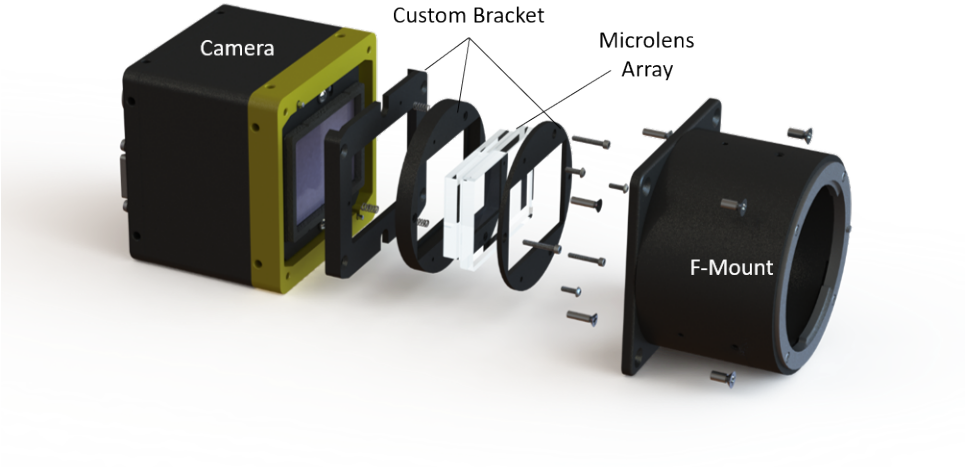

Figure 4.1: Plenoptic camera developed by Advanced Flow Diagnostic Laboratory at Auburn University.

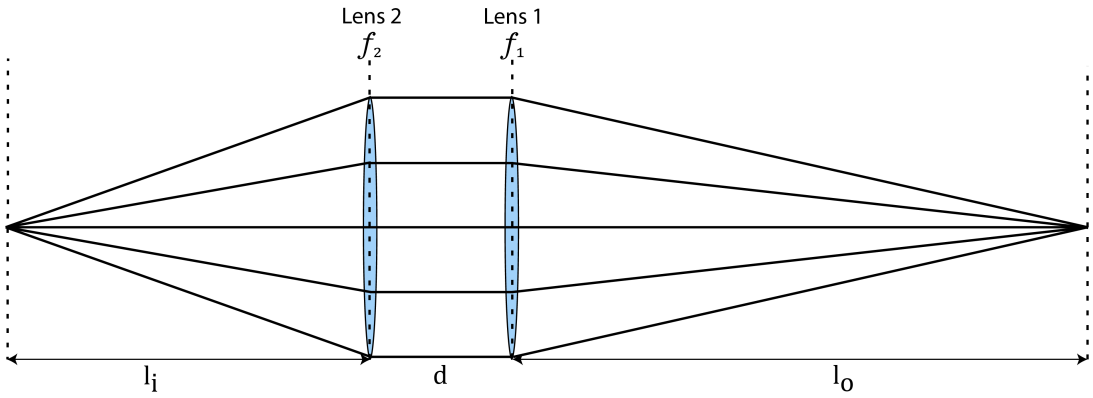

Figure 4.2: Schematic of a two lens system with the corresponding image and object distances.

The collection lens collimates the light before lens 2 focuses the light onto the image plane. Lens 2 can be varied to adjust l_i with a fixed aperture diameter, which will determine the microlens image size as shown by Figure 4.3. Equation 4.2 explains the relationship to produce f-matched microlens images [11],

$$d_s = \frac{d_a f_\mu}{l_i} \tag{4.2}$$

where d_s is the diameter of a microlens, d_a is the diameter of the aperture, f_μ is the focal length of a microlens, and l_i is the distance between lens 2 and the microlens array. The relationship of the similar triangles to formulate Equation 4.2 is displayed in Figure 4.3. A perfectly f-matched

image means each microlens image has the same size as a microlens, filling the sensor without overlap between microlens images. With the assumption of light rays being collimated by the collection lens, the image distance will be the focal length of lens 2. Fahringer *et al.* [11] calculated f_2 = 150mm to capture an aperture size large enough that every filter appears in the microlens images.

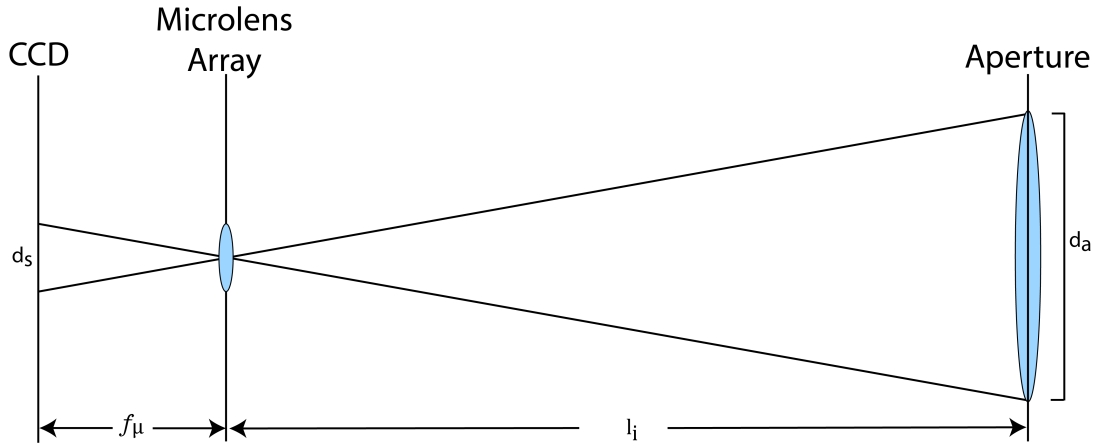

Figure 4.3: Schematic to describe the relationship between aperture and microlens size.

The collection lens can be designed with two separate variables. One way is to set the magnification variable constant, which will return both working distance and focal length. The other way is to set working distance constant that will generate a focal length and magnification. Not all combinations of magnification and working distance will work with the current plenoptic camera design as described by Fahringer [11]. If a certain combination of magnification and working distance is required but is not achievable, there are two methods to adapt the systems for the requirements. One option includes changing the aperture diameter, which would require changing the focal length of lens 2. The second option includes redesigning a new microlens array to have f-number = l_i/d_a [11]. However, due to cost and complexity, redesigning the microlens array is not the preferred method. Lens 2, on the other hand, is relatively trivial to change. Fahringer *et al.* [11] found after using the two lens configuration, the drifting that occurred in Danehy's *et al.* [3] design was drastically reduced.

4.0.1 Preliminary Design

A schematic of the preliminary design for the multi-band plenoptic camera is displayed in Figure 4.4. The design was based on earlier work by Fahringer *et al.* [11], but with a linearly variable filter instead of discrete filters. The rainbow filter is rectangular with dimensions of 3.94 cm wide by 3.25 cm tall. A plastic rectangular filter mount is composed of two rectangular pieces that sandwich the filter. The plastic filter mount is held in a custom 5.08 cm diameter lens tube connector, produced by Danehy's group at NASA Langley. Lens 1 and 2 are both 5 cm diameter plano-convex, achromatic lenses with an anti-reflective (AR) coating wavelengths between 400nm-1000nm from Edmond Optics. Lens 1 is mounted in a 5.08 cm diameter lens tube that is 1.27 cm long. To allow for fine adjustments between lens 2 and the microlens plane, lens 2 is mounted in a 5.08 cm diameter adjustable lens tube with a range of 3.33 cm. The focal length f_1 = 500mm was chosen to produce a long working distance, which will separate the camera from high temperatures. Consequently, the larger working distance also provides a larger depth of field. Lens 2 had a focal length of f_2 = 150mm because it was designed to image the entire rainbow filter with of 3.94 cm, similar to Fahringer [11]. With a perfect system, the lens would f-match the microlens array, but it cannot be completely f-matched because of the use of commercial lenses. Consequently, an circular iris was added between the two lenses to ensure control of aperture size on the sensor plane. If sub-aperture images (microlens images) were not controlled, they would overlap making the overlapping portions unusable. The whole multi-band assembly was connected to the plenoptic camera using a 5.08 cm lens tube to F-mount adapter. The initial design was usable, but had artifacts that added limitations.

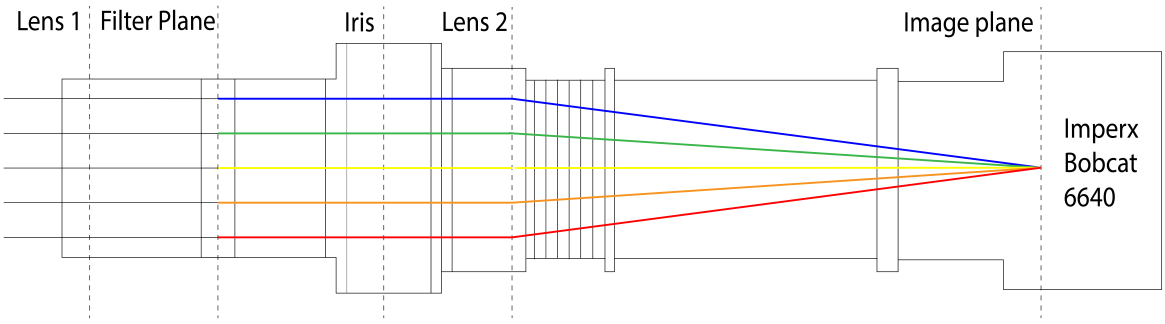

Figure 4.4: Schematic of the preliminary design of the multi-band module.

The preliminary design of the camera produced several image artifacts that could be detrimental to color imaging. The first artifact was the color filter did not attenuate wavelengths longer than 800nm in the section that was supposed to pass wavelengths 300nm - 400nm as presented in Figure 4.5. This can lead to the illusion of wavelengths between 300nm - 400nm being at higher intensities than is actually emitted. This will create disparities in wavelength intensities since blackbody radiators emit higher intensity at longer wavelengths as described by Equation 2.1. One way to correct for this would be to make a physical mask over the undesired portion of the filter. Unfortunately, a mask would completely eliminate the portion of the filter it covers, but that is acceptable because the corresponding intensities are already unusable. Another option would be to image the desired portion of the filter by reducing aperture size by altering lens 2. If those wavelengths are important, a shortpass filter can be placed in lieu of the rainbow filter to attenuate this unwanted result. The preliminary design used a mask. The correct mask was found by increasing the amount of tape over the portion of the filter that produces the undesired result until it was completely eliminated. A 3D printed filter holder was then designed to mask the undesired section of the filter.

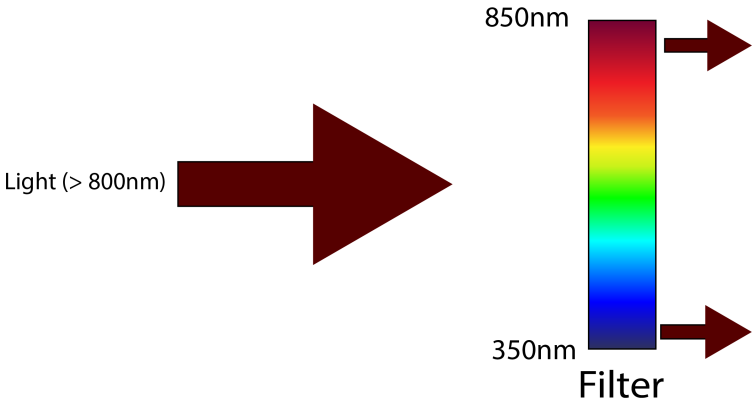

Figure 4.5: Schematic showing how longer wavelengths passing through the region that correspond to shorter wavelengths.

Another artifact of the preliminary design was a large shift in (u,v) wavelength location across the (s,t) plane of approximately 2.5 pixels, which can be seen in Figure 4.7. As displayed in the graph on the left, wavelength location for 610 nm was around two pixels from the center of the microlens towards s coordinates close to 0. On the other side of the s plane,

610nm wavelength locations were at one pixel to the left of the microlens center. In a ideal configuration, wavelength location in the (u,v) plane would remain constant across the (s,t) plane. The limitation occurs due to the finite distance between lens 1 and lens 2 as a simple schematic shows in Figure 4.6. If light is emitted at the focal plane of lens 1, but off the optical axis, the light will be collimated at an angle by lens 1, with respect to the optical center line. If the filter is not placed at the exact aperture plane of two lenses, there will be some angle between the filter and aperture plane. The angle changes depending on location in the object plane, and will cause a linear shift in location behind the microlens.

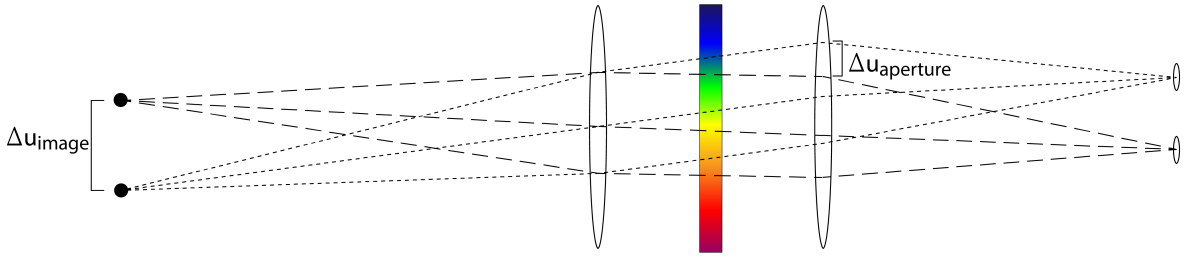

Figure 4.6: Schematic of the two lens system with the filter not at the aperture plane causing a shift in wavelength location.

Lastly, periodic banding or ”grid locking” was observed in both wavelength locations and temperature maps. This artifact occurs due to discrete sampling of the light. As will be explained in Chapter 5, wavelength information is averaged vertically (v direction) because the linear variable wavelength filter is oriented to only be a function of horizontal direction (u). Variations in wavelength can occur vertically, causing this artifact. Another explanation is that the microlens array axis is not aligned perfectly with the sensor axis, causing the banding artifact as explained by Fahringer [11]. The amplitude of variation in wavelength locations was about 0.2 pixels, which led to temperature fluctuations of approximately 10 K.

4.0.2 New Design

Figure 4.8 shows the current version of the multi-band plenoptic camera with labeled part locations. Lens 1 and lens tube mount are the same as the preliminary design. Connection between the multi-band module and the plenoptic camera remains consistent with a lens tube

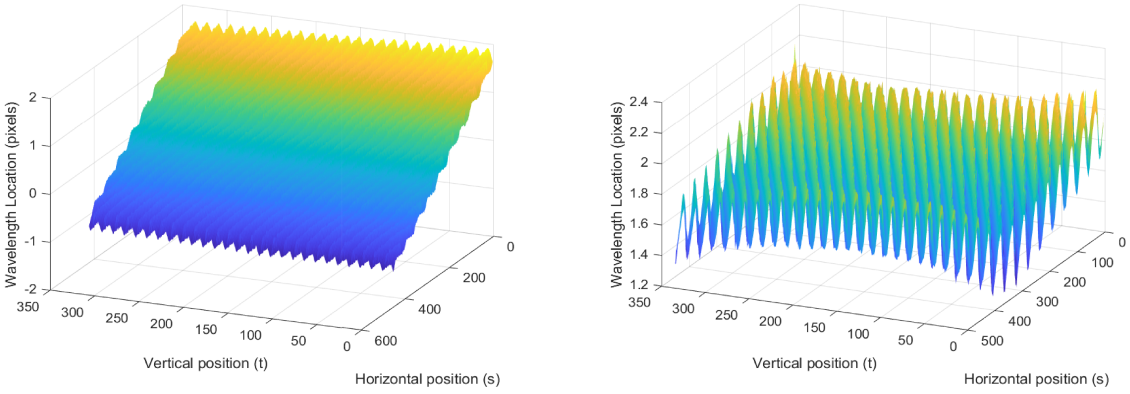

Figure 4.7: Wavelength locations with respect to the center of a microlens across the microlens plane (s,t) for 610nm of the old design (left) and new design with the 3D printed aperture stop(right). Note that the z-axis range is different for both cases to show the grid locking.

to F-mount adapter. The newest design changed lens 2 to be a plano-convex, achromatic lens with an AR coating between wavelengths 400nm-1000nm, with a focal length, $f_2 = 75$mm. The adjustable lens tube also had to be replaced with a two inch diameter, 3.81 cm long lens tube. The new lens 2 has a larger center thickness of 4.5mm, which was too wide for the adjustable lens tube used in the preliminary design.

From Equation 4.2, a reduction in focal length for a fixed microlens array makes the diameter size smaller. Therefore, the lens 2 images a 1.9 cm diameter region of the rainbow filter instead of the preliminary design, which imaged a diameter of 3.75 cm. The main reason for changing lens 2 was to capture the desirable portion of the rainbow filter, eliminating the need to mask a portion of the filter. the removal of the mask allows all pixels behind the microlens to capture spectral information. The new design has a spectral resolution of about 22nm/pixel, compared to the 42nm/pixel of the preliminary design. The increased spectral resolution is a product of each pixel imaging a smaller region of the filter. Also, increasing the wavelength resolution decreased the period and amplitude of the periodic banding. However, decreasing the focal length of lens 2 caused an increase in spherical aberrations. Fortunately, spherical aberrations can be accounted for during wavelength calibration as described in the following section.

Another key aspect of the new design is reduction in spacing between lens 1 and lens 2. Spacing reduction was done to attempt to reduce the distance from the filter plane and the

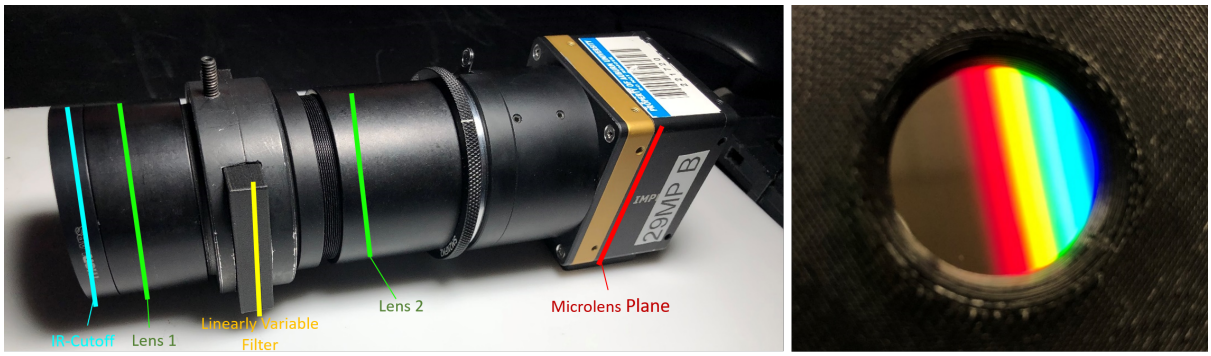

Figure 4.8: (Left) Schematic of the latest multi-band plenoptic camera design. (Right) Image of the linearly variable filter behind the 3D printed filter mount with an aperture stop.

aperture plane to decrease the wavelength location shift as described earlier. The reduction in wavelength location shift across the microlens plane can be seen in Figure 4.7, with a shallower slope across the surface of wavelength locations. The iris was removed, causing a spacing reduction of about 2 cm. Since the rectangular filter already had a plastic holder, a new filter mount, shown in Figure 4.8, of the same dimensions was 3D printed to have the appropriate aperture diameter of 19mm, according to Equation 4.2. Placing the aperture stop directly on the filter reduces angular components that can occur between the filter and iris. The reduced spacing with nothing else altered, reduced the wavelength shift from 2.5 pixels to 0.8 pixels for every wavelength calibrated. The old design caused wavelengths close to the perimeter of the wavelength range to be unusable due to vignetting. With a decrease in shift, more wavelengths became available as a result of of less vignetting.

A final addition to the multi-band plenoptic to improve temperature measurements was an IR-cutoff filter in front of lens 1. Figure 4.9a shows emitted intensities of a black body at 1500 K over the spectrum captured by the rainbow filter. For unfiltered intensities, the sensor can only record down to 600nm with saturated pixels corresponding to 825nm because the sensor has a bit depth of 12. A 12 bit sensor can record a dynamic range up to 4095 intensity levels. Using the intensity distribution from Planck's equation in Figure 4.9, intensity at 850nm is about $4{\cdot}10^9$, where intensity at 650nm is about $0.2{\cdot}10^9$. Thus, there are approximately 3800 intensity levels between wavelengths 600nm and 850nm. While a 12-bit sensor can record up to 4095 levels, low intensity has increasing signal-to-noise errors that arise. Only half of the wavelengths are being illuminated on the sensor for this case, which limits the number of

wavelengths bands because wavelengths below 600nm are not intense enough to be recorded by the sensor. Filtering light before being captured by the sensor can balance the intensities across all wavelengths, allowing the sensor to record intensities at all wavelengths. This can be conducted by attenuating intensities at the longer wavelengths such that the shorter wavelengths will be within the 4095 intensity levels of the sensor. Figure 4.9b shows transmission percentage of light for different wavelength for an IR-cutoff filter with a cutoff frequency of 720nm. The transition window from passband to stopband was about 200nm. The transmission function balances intensities across the microlens to have most pixels illuminated. It is also easy to install and has no correlation to orientation. A gradient ND filter was considered, but it was difficult to find one with the appropriate gradient. It would also be difficult to secure a gradient ND filter to have the equivalent gradient between temperature measurements and experiments.

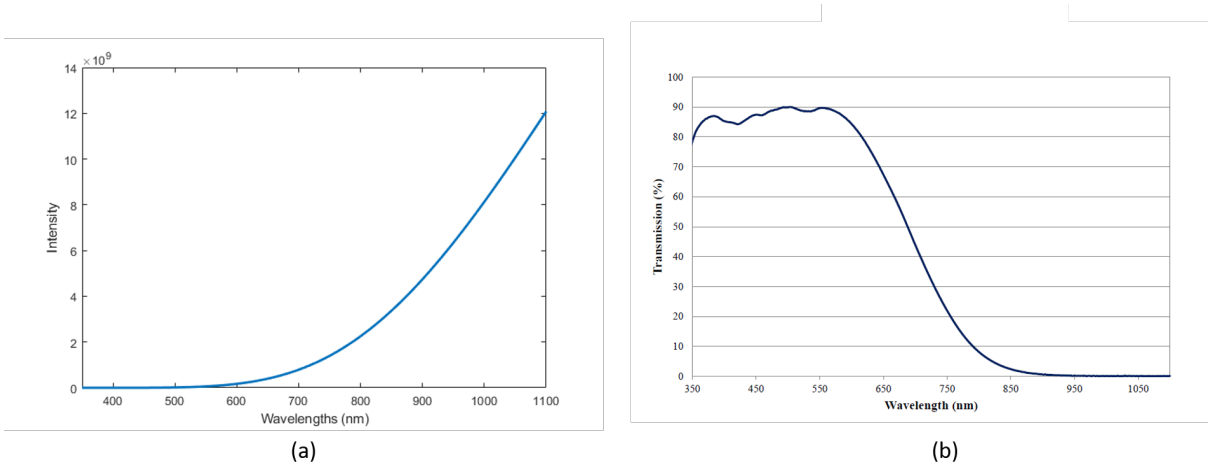

(a) (b)

Figure 4.9: (a) Intensities emitted by a blackbody radiator at 1500K. (b) IR-cutoff filter 4th order polynomial fit over wavelengths 400nm to 800nm, which will be convolved with the blackbody spectrum reducing balancing intensities across the wavelength range.

Chapter 5

Data Processing

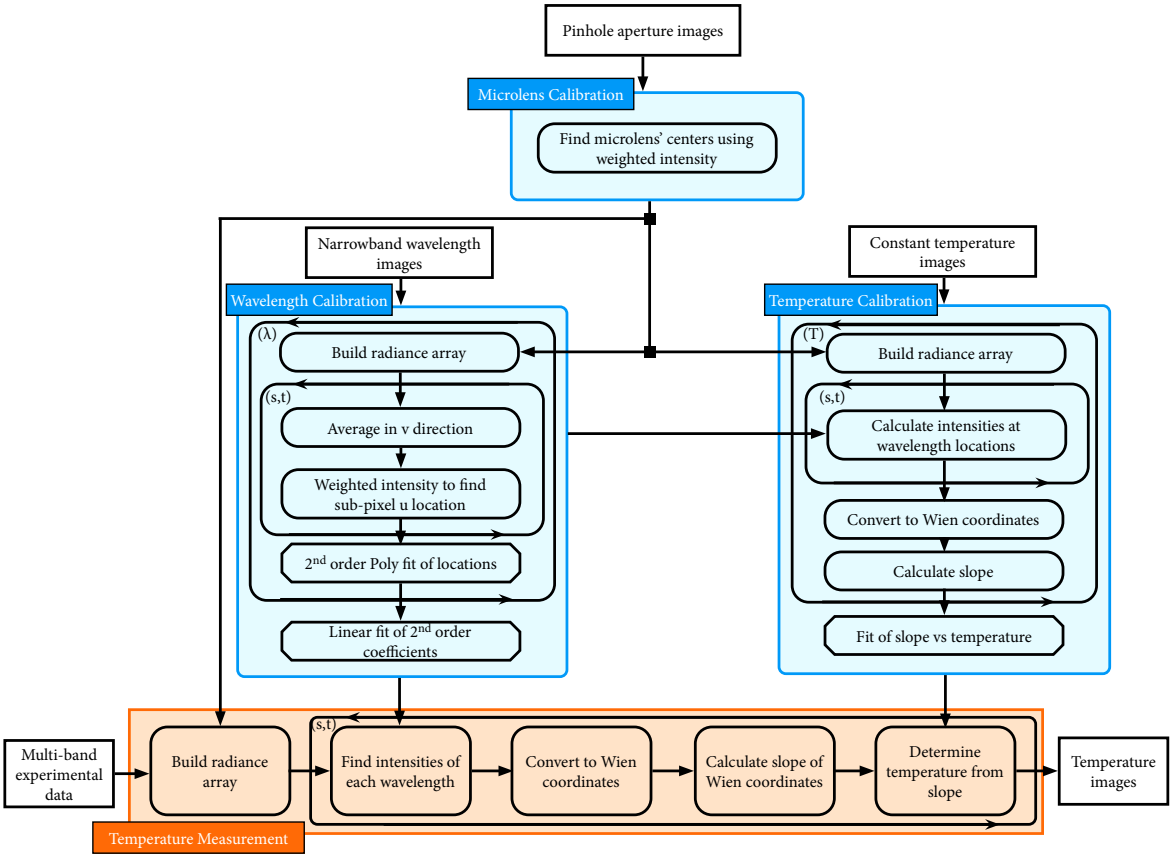

Figure 5.1: The multi-band plenoptic pyrometer pipeline flowchart that shows the required steps and calibration to achieve temperature maps.

Figure 5.1 presents a flow chart depicting the different steps and calibration required to generate a temperature map image from both experimental and calibration images. Microlens calibration is the first step required for wavelength and temperature calibration, and temperature measurements. Wavelength calibration is required to find the wavelength locations behind

each microlens, which can be used to find wavelength intensities for both temperature calibration and measurements. Temperature calibration is used to determine the cameras response to irradiance. In this chapter, data processing steps for calibration and temperature measurements will be discussed in detail.

5.1 Microlens Calibration

One important step to create the 4D radiance array for the two plane parameterization, as described in Chapter 3, is locating where each microlens image is captured on the sensor. The center of the microlens is the origin of the (u, v) coordinate system of the two-plane parameterization. The number of microlenses in the horizontal and vertical directions provides the number of s (horizontal) and t (vertical) points in the (s, t) plane. Each microlens center can be determined by imaging white light through a pinhole aperture. Since the center of the aperture corresponds to the center of the microlens, small circular groupings will appear on the image sensor as shown in Figure 5.2. A weighted intensity centroid finding algorithm, from the Light-Field Imaging Toolkit (LFIT) produced by AFDL, steps through the pinhole aperture image to calculate sub-pixel locations of microlens centers. A matrix of center locations in sensor coordinates along with the number of microlens centers found in the horizontal and vertical directions are outputs from microlens calibration. LFIT is described in a more detail by Bolan *et al.* [50].

5.2 Wavelength Calibration

Wavelength calibration is conducted to find an equation to assign a (u, v) location of all corresponding wavelengths of the rainbow filter for each (s, t) coordinate. For an ideal system, every wavelength location would be the same across the microlens plane, but this is not the case. Therefore, wavelength calibration accounts for anomalies like wavelength shift and spherical aberrations. Wavelength calibration is conducted by sampling the filter with narrow-band LEDs. An example of a narrow-band LED with a central wavelength at 465nm is shown in Figure 5.3. LEDs are diffused before entering the camera so that light fills the entire image plane.

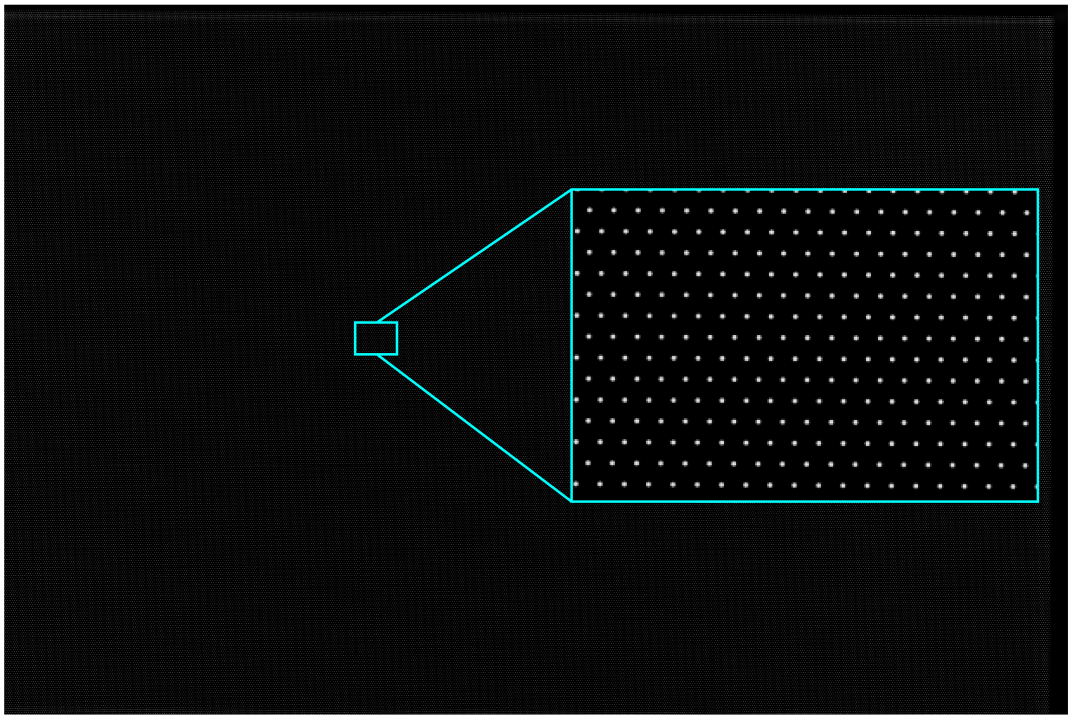

Figure 5.2: Raw plenoptic image of white light through a pinhole aperture. A region of the image is zoomed into to show several microlens images.

This is conducted by placing a diffused glass in front of the multi-band module to produce images shown in Figure 5.3. Microlens images of each of these narrow-band LEDs are displayed in Figure 5.4. For this research, eight different wavelengths locations are sampled using LEDs with a central wavelengths of 405nm, 465nm, 525nm, 610nm, 645nm, 680nm, 750nm, and 800nm. Every LED was purchased from Thorlabs and is powered by a USB-powered LED mount. The center wavelength, spectral full width half maximum, and maximum optical power are depicted for each LED in Table 5.1.

Table 5.1: Narrow-band LEDs used for wavelength calibration.

Thorlabs Part #	**Center Wavelength**	**Spectral FWHM**	**Optical Power**
LED405E	405nm	20nm	10 mW
LED465E	465nm	25nm	20 mW
LED528EHP	528nm	35nm	7 mW
LED610L	610nm	12nm	8 mW
LED645L	645nm	16nm	16 mW
LED680L	680nm	16nm	8 mW
LED750L	750nm	23nm	18 mW
LED800L	800nm	30nm	20 mW

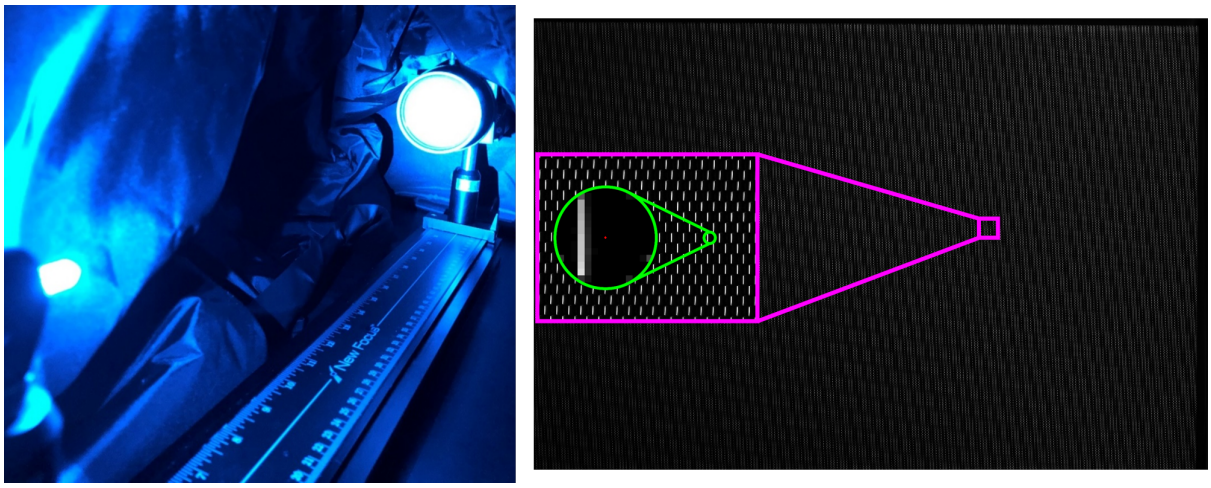

Figure 5.3: (Left) Image of a 465nm narrow-band LED being used to produce the image on the right. (Right) Raw multi-band image of 465nm narrow-band LED that is zoomed in to show a single microlens image.

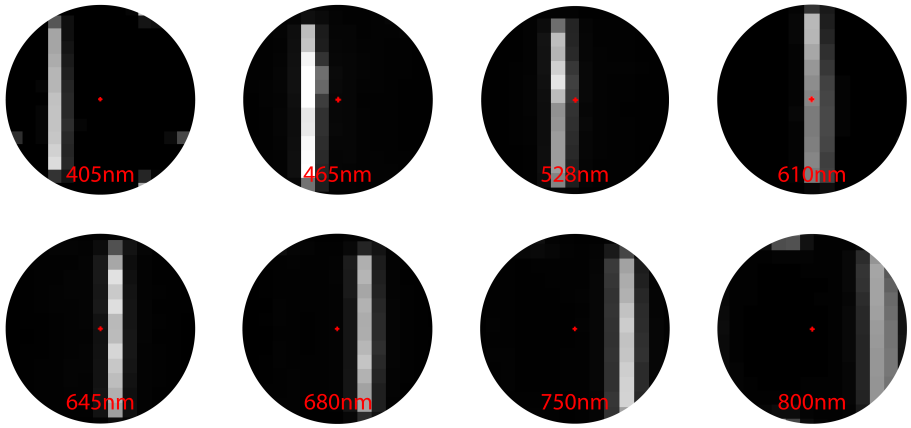

Figure 5.4: Microlens images for different narrow band LEDs which is used for wavelength calibration. Adapted from Kelly [14]

Stepping through the wavelength calibration algorithm of Figure 5.1, the first step of wavelength calibration is to create the microlens image stack (radiance array) of a narrow-band LED plenoptic image using microlens centers from calibration. The algorithm then steps through every microlens image and averages in the v direction because the wavelength filter is oriented such that the wavelengths vary linearly in the u direction. Orientation of the filter can be different, but the algorithm would need to be altered accordingly. The averaged array is then passed into a weighted intensity algorithm to find a sub-pixel u location for that wavelength. Once every location of one wavelength is determined for each microlens, a 2^{nd} order polynomial fit is applied across the (s, t) plane using Equation 5.1, where each a is a coefficient determined

using a least squares solver. The fit accounts for the linear shift and the spherical aberrations for every wavelength.

$$u_\lambda(s,t) = a_0 + a_1 s + a_2 t + a_3 st + a_4 s^2 + a_5 t^2 \tag{5.1}$$

Once a 2^{nd} order polynomial is formed for every calibration wavelengths, one final step of wavelength calibration is required to provide the ability to calculate any wavelength location of the filter. It was concluded that the 2^{nd} order coefficients varied linearly with wavelength. Therefore, a linear fit of wavelength is formed for every coefficient. Finally, Equation 5.2 is the final wavelength calibration equation that can determine wavelength location across the microlens plane.

$$u(s,t,\lambda) = a_0(\lambda) + a_1(\lambda) s + a_2(\lambda) t + a_3(\lambda) st + a_4(\lambda) s^2 + a_5(\lambda) t^2 \tag{5.2}$$

where each coefficient a_i is a linear function of wavelength. One future improvement includes factoring in the v direction instead of averaging vertically because the wavelengths could vary vertically due to optics and alignment of the filter. The banding issue described earlier, was eliminated when using only one v position to determine temperature. Therefore, there are variations in the v direction that requires further calibration.

5.3 Temperature Calibration

Temperature calibration is conducted by imaging objects at a range of known temperatures to quantify the pyrometer's response to emitted irradiation. The first step is to determine the material surface that will be used to generate irradiation. Generally, a material that has properties similar to a black body radiator is used to eliminate emissivity variation for calibration as described by Arújo [1]. Spectral pyrometry technique was used for measurements because it reduces the dependence on emissivity. Therefore, a black body is not required for calibration, but rather a gray body. Graphite was chosen for the calibration material because of its gray body characteristics in the temperature and wavelength range that was used.

Figure 5.5 shows how temperature calibration images were captured. A bar of graphite, bought from McMaster-Carr (part #: 9121K63), was placed in a Lindberg/Blue box furnace, which graphite was imaged through a two inch optical hole. The grain size of the graphite was 0.0004". A set of images is captured of the graphite with oven temperatures ranging from 600°C to 1100°C at increments of 50°C, where 1100°C was the maximum temperature of the oven. To ensure accurate temperature measurements for calibration, two thermocouples were placed against the graphite on either side of the optical hole. Exposure time of the camera was varied to maximize signal-to-noise ratio between temperatures.

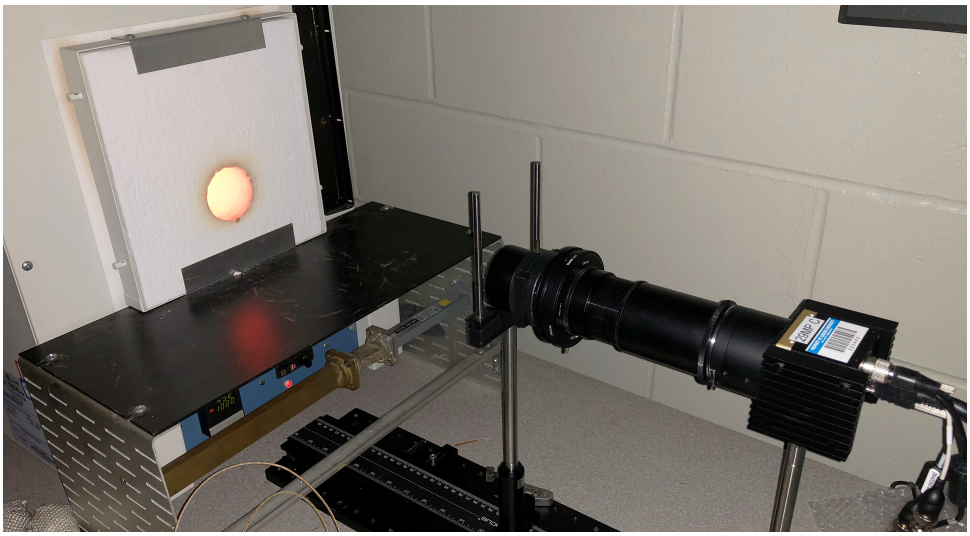

Figure 5.5: Temperature calibration arrangement of the box furnace and camera.

Calibration images were then processed to formulate the camera's response to radiation. The first step of temperature calibration was to discretize the microlens images into a 4D radiance array at one temperature, using microlens calibration. Since the optical hole did not fill the entire sensor, the images were cropped to the part of the image that captured the heated graphite. Figure 5.6 shows a multi-band plenoptic image of the radiating graphite inside the optical hole of the oven along with a microlens image. The algorithm then steps through the (s, t) values of the radiance array, calculating intensities at a range of wavelengths. Wavelengths ranging from 625nm to 825nm were used when the IR-cutoff filter was not installed. When the IR-cutoff filter was in place, wavelengths 450nm-825nm were used for calibration. Intensities captured at one temperature for every (s, t) value are then averaged and converted to Wien

coordinates that are given by Equation 2.18. Next, a linear fit was conducted on the Wien coordinates to determine the slope of the line. Once slopes were determined for every temperature, a fit was formulated to calculate temperature from a slope. Normalized captured intensities for three different temperatures and captured intensities converted to Wien coordinates at those three different temperatures are displayed in Figure 5.7. Exposure times were 44.5, 3.7, and 0.8 milliseconds (ms) for temperatures of 758°C, 939°C, and 1092°C, respectively. The slope of the Wien coordinates was increasing with increasing temperature. It also shows how linear Wien coordinates were compared to the measured spectrum.

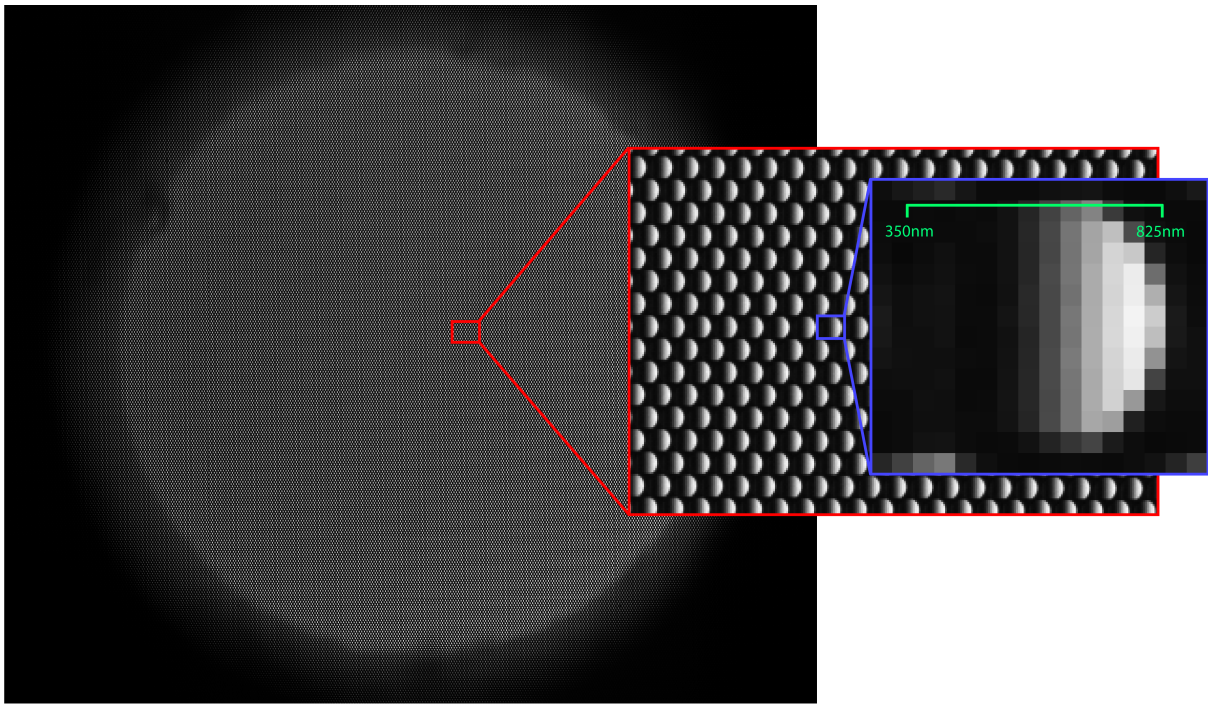

Figure 5.6: A multi-band plenoptic image of graphite at a temperature of 1000°C. It further shows a zoomed image encompassing several microlenses and a single microlens.

The IR-cutoff filter can be calibrated in two ways: 1) it can be added to the camera during temperature calibration of the graphite at known temperature, or 2) intensity percentage attenuation over different wavelengths can be determined. Since the IR-cutoff filter was added to the design when the temperature calibration oven down for maintenance, the IR-cutoff filter was calibrated by option two. However, for future experiments, calibration using option 1 will be used to get a more accurate calibration. To do this, the narrow-band LEDs used for wavelength calibration were used as the light source. The narrow-band LEDs were rigidly mounted in front

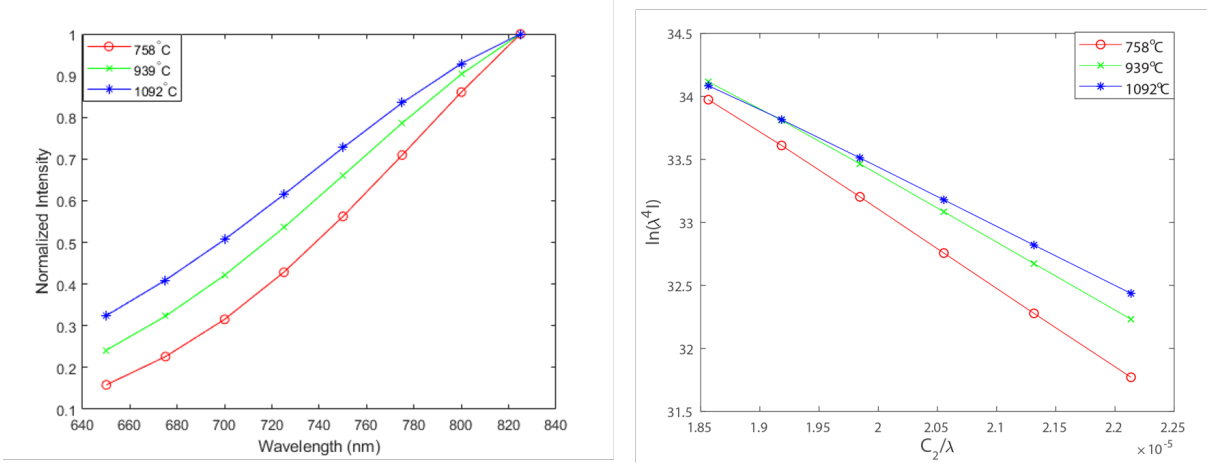

Figure 5.7: (Left) Captured intensities at three different temperatures for one microlens, and (Right) those intensities converted to Wien coordinates.

of the multi-band plenoptic camera. Two images were captured for each narrow-bad LED, one with and without the IR-cutoff filter in front of the camera. The percentage in intensity attenuation for each wavelength was measured. A 4^{th} order polynomial was then fit to the eight points as shown in Figure 5.8, so the calibration could be used for any wavelength. The calibration appeared to be very similar to the reference filter response shown in Figure 4.9. However, to increase accuracy using this method of calibration, more points and a higher order polynomial is required.

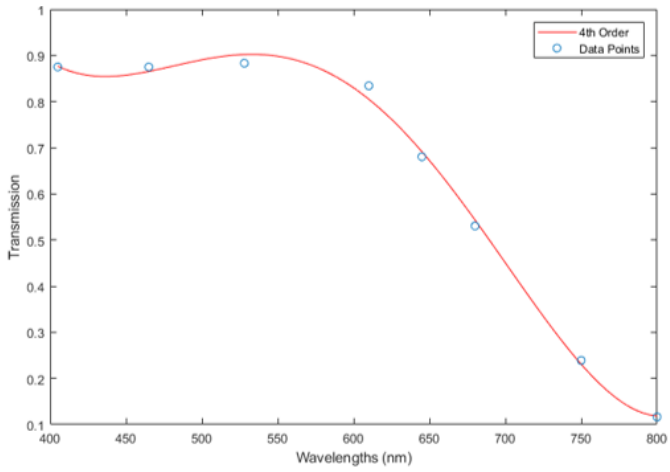

Figure 5.8: Calibration points for IR-cutoff filter with the 4^{th} order polynomial curve fit overlaid over the points.

5.4 Temperature Measurement

Upon completion of multi-band plenoptic camera calibration, 2D temperature measurements can be acquired. The first step was to capture a multi-band plenoptic image of the target surface or flame. Using microlens calibration, the image was formed into a 4D radiance array. As the algorithm looped through each s and t values, a threshold on microlens image intensity was checked ensure appropriate signal-to-noise ratio was kept before calculating temperatures. If the threshold was not met, the algorithm continued to the next microlens. If the microlens image intensity was above the threshold, intensities at user specified wavelengths were found using wavelength calibration to generate locations and a bilinear interpolation method to find intensities at sub-pixel locations. The function given by wavelength calibration could be used to find wavelength for a specified pixel location. The captured intensities were then converted to Wien coordinated and fit to a linear function. The slope of the Wien coordinates was then an input into the function generated by temperature calibration. The output of the function was temperature for a (s,t) location, and then continues to the next (s,t) point. Note that if a rectangular microlens array is used, then the generated temperature image is the final output. However, if a hexagonal microlens array is used, an extra step is required to map hexagonal coordinates to rectangular to be properly displayed. The hexagonal to rectangular interpolation method used for the temperature map was created by AFDL for LFIT.

Chapter 6

Experimental Configuration

In this chapter, three different experimental setups are explained that test the limits of measuring temperature using the multi-band plenoptic camera. The initial experiment was an ideal case, which imaged the same graphite used for calibration at known temperatures. Another experiment using the same graphite was imaged as the graphite cooled down from a high temperature and compared to thermocouple measurements. Since the two graphite experiments are ideal, the purpose was to determine the best accuracy that can be achieved by the multi-band camera. The last two experiments applied the multi-band plenoptic to applications where the camera should see better results compared to traditional methods. One experiment consisted of imaging a dynamic flame of a strand burner plume for two different fuels with known temperature differences. Finally, the multi-band plenoptic camera was used to determine temperatures of copper during solidification. Material properties change drastically between the two phases of copper, making it difficult to measure temperature using conventional pyrometers.

6.1 Oven Measurements

Figure 6.1 shows the side and front view the graphite bar location inside a box furnace that was heated to different temperatures. The multi-band camera was used to determine temperatures of graphite at constant and cooling temperatures. The experimental configuration was shown in the previous chapter (Figure 5.5), which shows the Lindberg box furnace and plenoptic camera locations that were was used for both the initial calibration and this experiment's data acquisition. A schematic of the thermocouple locations on the graphite are displayed in Figure 6.1. The graphite plate is located about 10 cm from the optical hole. Two K-type thermocouples

were placed on either side of the graphite to get a distribution of point measurements to compare to the multi-band camera. The selected thermocouples were shielded, and each probe had a diameter of 3.2 mm. Thermocouples have an accuracy of $\pm 0.75\%$ between the actual and measured temperatures. The temperature were varied to four different set point temperatures: 675°C, 775°C, 875°C, and 975°C. The four temperatures differed from the calibration temperatures by 25°C. The measurements were recorded using a handheld thermocouple reader. The temperature of the graphite was ensured constant by waiting 5 minutes once the temperature was stabilized according to the thermocouples.

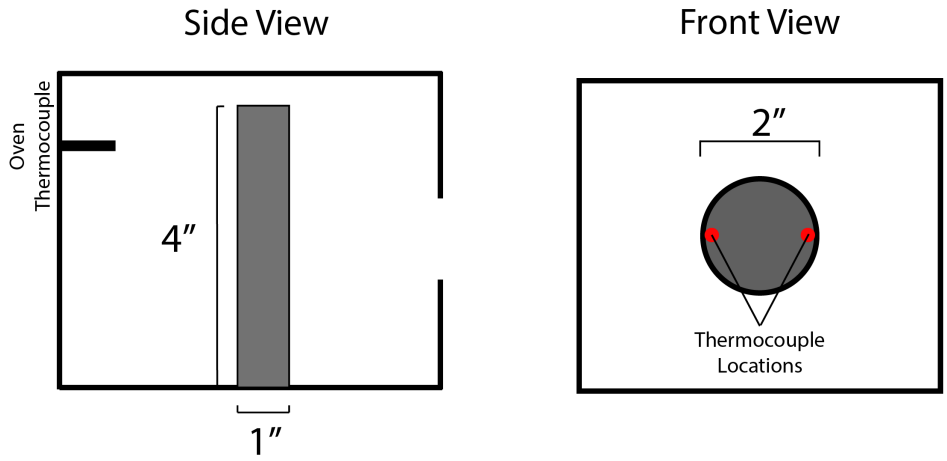

Figure 6.1: Schematic of the box furnace with the graphite inside from a front view (right) and front view (right).

The next test using the Lindberg box furnace and the graphite was imaging the graphite as it cooled inside the furnace. The graphite was heated and stabilized at 890° before the oven was turned off. During the cooling process, the camera and thermocouples captured data points every 30 seconds. The cooling oven was imaged because it produced an idealized trend that could be measured by the thermocouples and compared to the mulit-band.

6.2 Strand Burner Plume

The strand burner experiment applied the multi-band camera to a dynamic flame structure. The strand burner plume experiment was an example of one aerospace application that the multi-band camera is applicable. The strand burner, shown in Figure 6.2, used for this experiment was

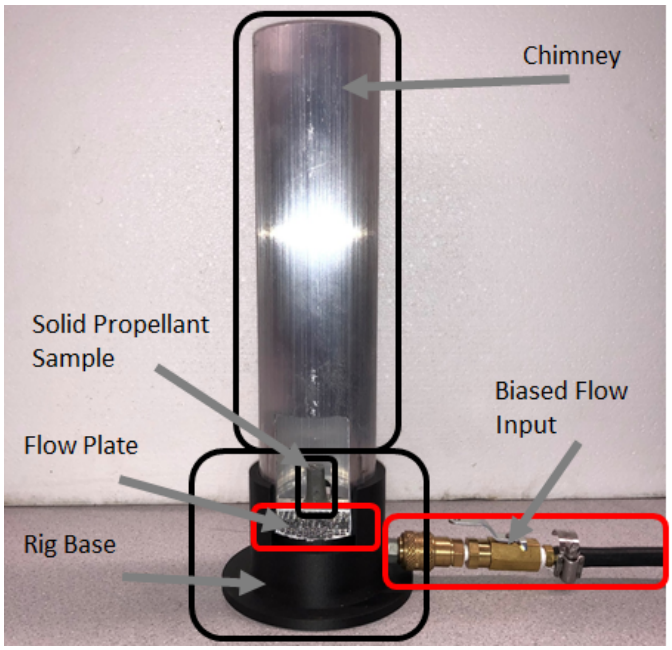

Figure 6.2: Atmospheric strand burner schematic.

kept at atmospheric pressure. The burner had two open holes, one for optical access perpendicular to flame propagation and the other at the top of the chimney for soot removal. The optical hole had dimensions of 8.3 cm tall by 7 cm wide. The chimney had a diameter of 7.62 cm, which compressed air was blown from the bottom flow plate to ensure flame and smoke was removed from the optical viewing window. A K-type thermocouple, with a probe diameter of 1.57 mm, was placed down the chimney directly above the center of test samples with vertical separation of approximately 1.75 cm. The thermocouple provided preliminary comparisons in temperature with the multi-band camera's temperature measurements. However, a thermocouple is a time averaged temperature measurement and cannot capture both temperature gradients or temperature fluctuations. Therefore, the temperature captured by the thermocouple was an average value over time. The thermocouple recorded temperatures every 0.05 seconds, but could not capture temperature fluctuations at that rate. The camera sensor acquired images at 1Hz, with an exposure time of 100μs. Note that the camera captures line of sight temperature measurements, which can result in a biased towards higher temperatures of the flame.

The two fuels were selected based on: (1) their known temperature differences and (2) the fuel production capabilities of the Combustion Physics Laboratory. Figure 6.3 shows the two different solid fuels that were used in the strand burner. The solid fuel samples were made from

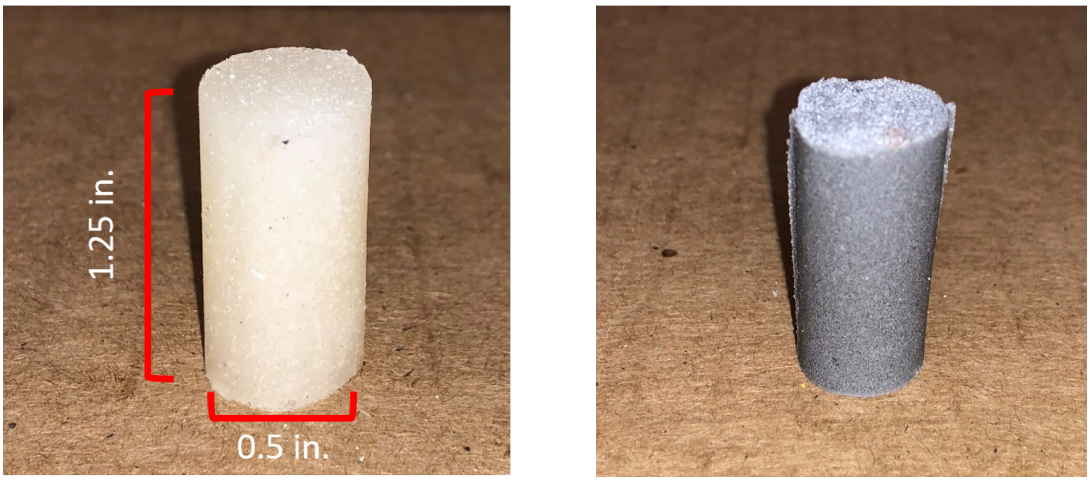

Figure 6.3: (Left) Image of one solid fuel strand composed of AP and HTPB with dimension shwons, (Right) image of solid fuel strand composed of AP, HTPB, and Al. These fuels are used for the strand burner experiments.

hydroxyl-terminated polybutadiene (HTPB) as the binder and ammonium perchlorate (AP) as the oxidizer and fuel. The difference between the two samples was one also had aluminum (Al) particles added to the mixture. The addition of Al was chosen because it burns at higher temperatures, which is typically added to increase burn rates and increase specific impulse compared to non-detonable propellants. Composition of the two fuels were 40% HTPB, 60% AP, and 0% Al for the first sample, while the second was 30% HTPB, 60% AP, and 10% Al. The fuels were ignited with a butane torch to ensure fast and even ignition. Images were captured from ignition to burnout for 5 samples of each fuel. Exposure time was set constant during each test. Initially, each fuel had several samples that were burned, but not recorded to get the exposure time set for maximum SNR.

6.3 Solidifying Copper

The solidifying copper experiment was designed to determine the efficacy of the multi-band camera to capture temperature and temperature gradients in an image with different material properties. Solidifying copper also simulated another important application in aerospace of additive manufacturing. Figure 6.4 shows a schematic of how the plenoptic camera was configured to capture temperatures of the copper. Copper was melted in an electric metal foundry with a maximum temperature of 1150°C. The foundry had a graphite crucible to contain the

melted copper with a depth of 10.16 cm and a diameter of 3.8 cm. Multipurpose 110 copper rod with a 2.54 cm diameter was used for the experiment. 110 copper is 99.9% copper, which is often used in electrical applications. The melting point for 110 copper is 1083°C. The emissivity of heated oxidized solid and liquid copper are approximately 0.78 and 0.143, respectively [16][51]. These emissivity numbers are only an approximation as shown by several papers that measure normal spectral emissivity at high-temperatures [52, 53, 54]. Kurosawa *et al.* [54] compared his measurement to several predecessors showed a variation of normal spectral emissivity over a range of temperatures. Another issue with measuring temperature and emissivity of molten metals is that they are highly reactive at high temperatures [54]. All of these works measured normal spectral emissivity of liquid copper, but emissivity can vary with angle of emission. Furthermore, Cagran *et al.* [52] showed that emissivity varied with wavelength from 0.35 to 0.1 for wavelengths 500nm to 800nm, respectively. Difference in emissivity of this magnitude would generally cause high temperature errors for traditional methods. Therefore, this challenging problem was chosen to help identify some of the challenges that will be faced when applying the multi-band plenoptic camera to a broad set of applications.

A 2.54 cm long cylinder of 110 copper was machined from the original rod with length of 15.1 cm. The multi-band camera was placed approximately 50 cm from the copper, which was conducted by getting the top part of the copper into focus. Then the foundry was closed and set to a temperature of 1150°C. Once the heated copper had temperatures above melting temperature, the lid of the foundry was opened and the exposure time of the camera was adjusted accordingly, to 1400μs. The foundry was turned off, allowing the liquid copper to cool. A K-type thermocouple was placed down one side of the crucible into the liquid copper to track temperatures. The thermocouple probe was placed towards the bottom of the liquid copper. This allowed the thermocouple to measure a more accurate temperature because it resulted in less radiation heat transfer. The thermocouple was shielded, which had a diameter of 3.2 mm. The accuracy of the thermocouple is $\pm$0.75% of the actual temperature. The multi-band camera captured images at 1 Hz as the copper cooled and solidified, which was performed simultaneously with the acquisition of thermocouple measurements.

Figure 6.4: Schematic of the metal foundry and location of camera with appropriate dimensions.

Chapter 7

Results and Discussion

This chapter covers the results from the three different experiments as described in Chapter 6, starting with the oven measurements. After presenting the results for each experiment, the performance of the multi-band plenoptic camera is discussed.

7.1 Oven Measurements

7.1.1 Steady temperature

Figure 7.1 shows 2D temperature measurements of a graphite plate at four different temperatures through the optical hole of the box furnace. The thermocouples are visible in both 963.2°C and 871.4°C temperature maps. The temperatures measured by the right thermocouple are displayed in the top left corner of the temperature maps. The temperatures measured by the thermocouples, and the average temperature and standard deviation of temperatures for the multi-band camera are presented in Table 7.1. Thermocouple measurements also have the accuracy in temperature shown next to the measurement. The right thermocouple measured a cooler temperature, which was also calculated by the multi-band camera. The average temperature was calculated using a 40x40 window of microlenses around the left and right side close to the thermocouples' location, while the standard deviation is conducted over for the temperature map of one image. A histogram of each temperature map is shown in Figure 7.2. Each bar in the histogram has a width of 4°C. The shape of each curve corresponds to a narrow bell curve.

As shown in Figure 7.1, the temperature distribution was captured to be relatively constant which is expected be because the thermocouples at most read a difference of 4°C. The maximum temperature difference between thermocouple and average temperature measured

Table 7.1: Temperature measurements of a graphite plate in the box furnace.

Oven set point	Left Thermocouple	Right Thermocouple	Averaged Camera Temperature	Standard Deviation
675°C	676.6°C ± 5.1	674.5°C ± 5.1	677.3°C	1.7°C
775°C	778.2°C± 5.8	774.1°C± 5.8	781.1°C	1.9°C
875°C	873.5°C± 6.5	871.4°C± 6.5	868.5°C	2.5°C
975°C	964.3°C± 7.2	963.2°C± 7.2	963.7°C	2.2°C

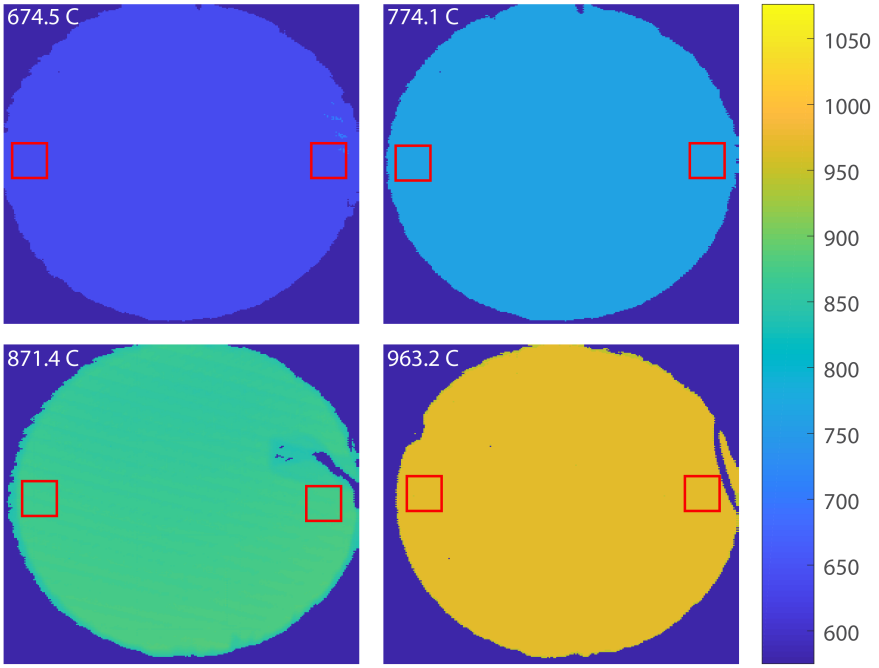

Figure 7.1: Temperature measurement (°C) of graphite at steady temperatures of 674.5°C, 774.1°C, 871.4°C, and 963.2°C as measured by thermocouples in the furnace. Red boxes indicate the region used to calculate average temperatures close to thermocouples.

by the multi-band camera was at 774.1°C, but was still within the accuracy of the thermocouples (±0.75%). Overall, the 2D temperature map had a maximum standard deviation of 2.5°C at 871.4°C. The deviation in temperature was 0.5% in the temperature of the graphite. The histogram shows that temperatures were very concentrated around one temperature with each having a spiked bell curve, which indicates small deviations from a measured temperature. The broadest peak occurred at 875°C, which agrees with the larger standard deviation. However, the number of bars is the same as the other static temperatures. For the ideal case, the multi-band camera using the spectral pyrometry method can determine temperatures within the calibration range to approximately 1%.

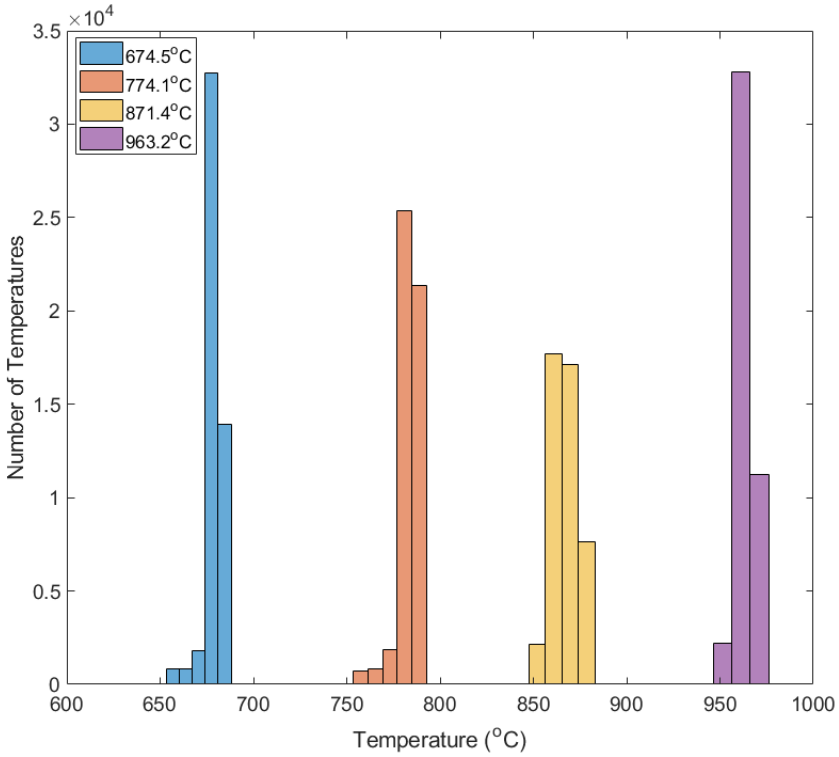

Figure 7.2: Histogram of temperatures across the graphite plate 674.5°C, 774.1°C, 871.4°C, and 963.2°C that was measured by the multi-band camera. The bin size of each bar is 4°C.

7.1.2 Cooling oven

Figure 7.3 presents a graph of thermocouple temperatures, calculated temperature at one microlens close to thermocouple 2, and the average temperature measured by the multi-band camera for each time step spanning the total time of 600 seconds. The temperature measurement of one microlens has some variation with regards to the thermocouple, but stays within the bounds of the two thermocouple measurements. The overall trend between the average temperature and the thermocouples are the same, with an initial slow decrease in temperature then increasing slope after 90 seconds. The graph also shows the average temperature with the standard deviation across the 2D temperature map at each time step. The error that is seen at one microlens corresponds to SNR, but only varies approximately .1% to .2% of the measured temperature. Taking thermocouple accuracy into account, camera temperatures fall within the range of thermocouple measurements. This shows the multi-band camera can capture trends

with a single microlens. Overall, the camera was able to capture the temperatures of the cooling oven to within 0.5% error.

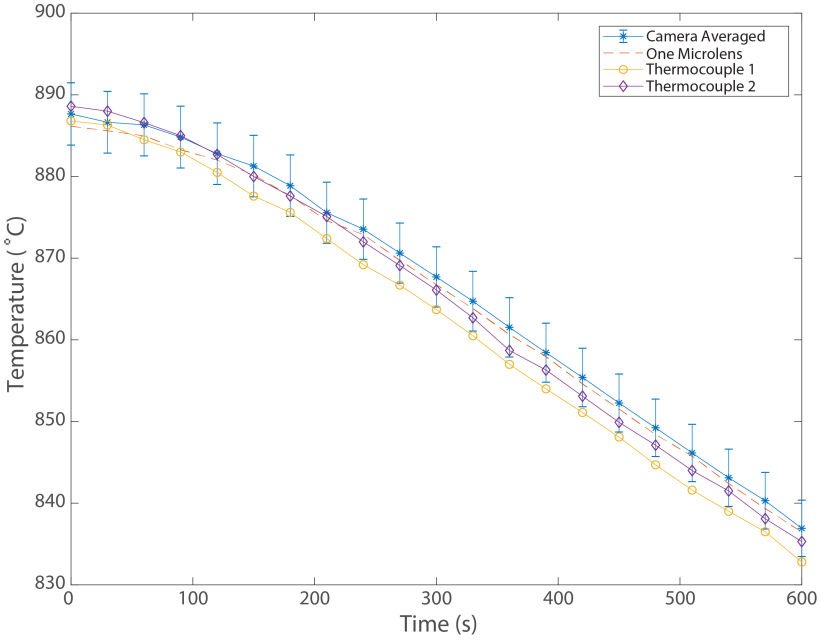

Figure 7.3: Comparison of temperature versus time of graphite in a box furnace with the oven turned off at t = 0. The graph shows two thermocouple temperatures, one microlens close to a thermocouple temperatures, and the average temperature measured by the multi-band camera with the standard deviation bars of the camera temperatures.

7.2 Strand Burner Plume

A raw multi-band plenoptic image of a plume produced by a sample with Al is shown in Figure 7.4. Notice the bright aluminum particles towards the top of the left image of Figure 7.4, where some of the particles appear to be out of focus. Particles have portions of their spectrum captured by several microlenses. The figure in the middle shows a zoomed-in region of a few microlenses from the raw plenoptic image. Balanced intensities across the microlens occurred due to by the IR-cutoff filter. The final temperature map created from the left image is displayed as the right image in Figure 7.4. Note that the Al particles have a higher temperature compared to the rest of the flame.

The left image of Figure 7.5 is the temperature measurement from the multi-band camera of the fuel with no Al. When compared to Figure 7.4, the flame is much smoother without the

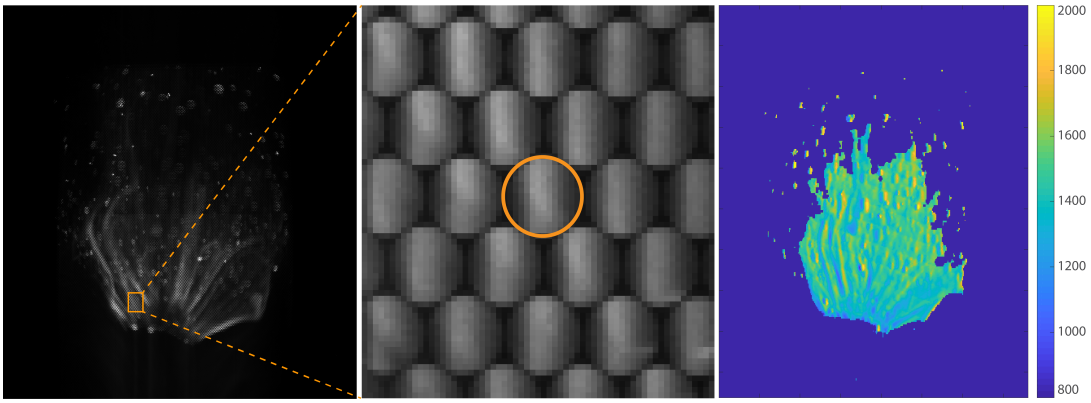

Figure 7.4: (Left) Raw multi-band plenoptic image of the strand burner plume, (Middle) zoomed raw image showing several micro images with the orange circle representing the boundaries of a single microlens, and (Right) temperature map of the strand burner plume [14].

high temperatures corresponding to Al particles. Two points were selected to show differences in captured raw intensities between a higher and lower temperature region, which is shown in the top right graph of Figure 7.5. The higher temperature region resulted in higher intensities as expected, while any temperature below 800°C would be thresholded because of the low intensities across the spectrum. The raw spectrum does not appear to resemble a Planck's equation due to the addition of the IR-cutoff filter. The two raw spectrums are then converted to Wien coordinates as displayed in the bottom right graph of Figure 7.5. Once in Wien coordinates, there is some waviness in the two spectra, although it is expected to be a straight line.

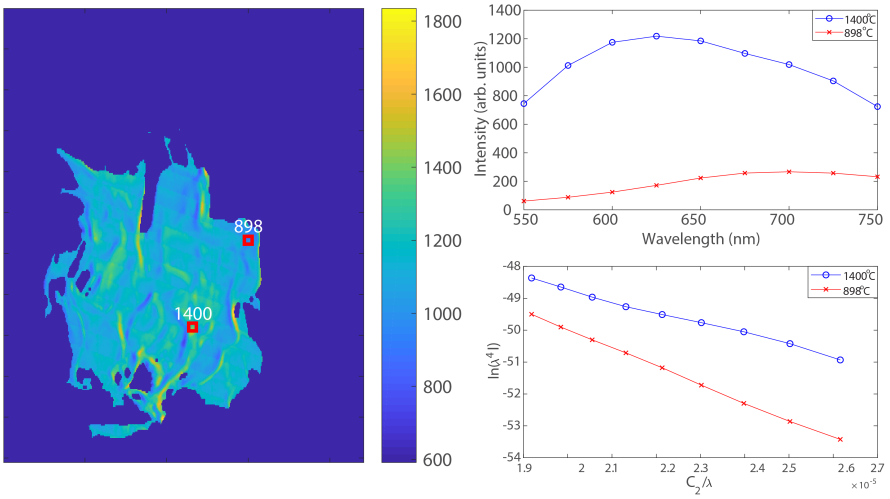

Figure 7.5: (Left) Temperature map of the strand burner plume with no Al, (Top Right) raw spectrum from the two points of interest, (Bottom Right) conversion of raw spectrum to Wien coordinates [14].

A histogram of temperatures calculated by the multi-band camera with and without Al are overlaid in Figure 7.6. As seen from Figure 7.5, the flame is smooth with many temperatures around the same temperature, which is presented as a spike in the histogram. When Al particles are added, the peak of the histogram is flattened and distributed across more temperatures. A temperature increase was expected between the two flames, and the case with Al increased approximately 400°C compared to the plume with no Al. The range of temperatures captured by the camera in both cases were between 800°C to 1000°C.

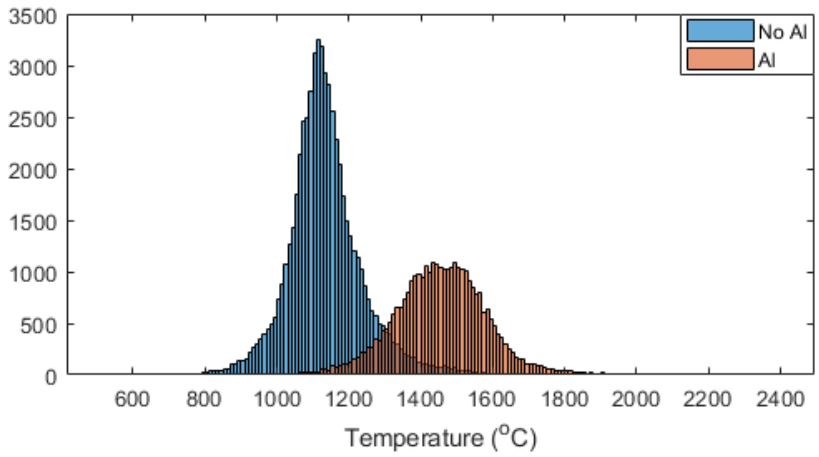

Figure 7.6: Histogram of temperatures calculated by the multi-band for the fuel with and without Al [14].

The experimental results aim to assess the multi-band camera's ability to capture temperatures of a dynamic flame. Due to the inherent three conditionality of the strand burner plume, portions of the flame appeared to extend beyond the DOF limits. This can affect the measurements acquired by the camera. Figure 7.4 shows the Al particles spanning several microlenses, which is a direct result of particles being out of focus. Temperature measurements for the out of focus particles will have error caused by portions of the spectra that were distributed across several of the surrounding microlenses. This distribution results in each microlens containing higher intensities for the respective portion of the spectrum. Therefore, the Wien coordinates will not be linear because of fluctuations in wavelength intensities. The particles that were captured by one or two microlenses provided higher temperature measurements than the ones that were out of focus, and the particles were only one or a couple microlenses wide. Based on this result, the temperatures of the histogram would be redistributed if every particle was in

focus. While the temperatures would be higher for the aluminum particles, they would span less microlenses possibly broadening the temperature distribution.

The waviness in the Wien coordinates, from Figure 7.5, could have originated from several factors. The factors include the 3D nature of the flame, IR-cutoff filter response calibration not being adequate, and variation in spectral emissivity. If radiation captured by the camera is outside the DOF, the parts of the spectrum captured by a microlens do not correspond to the same region, similar to the discussion in the last paragraph. Another reason for the waviness in the Wien coordinates could originate from the IR-cutoff calibration. For these experiments, the IR-cutoff filter had a separate calibration, therefore, the calibration polynomial could have not matched the actual attenuation curve of the filter. When accounting for the IR-cutoff filter, different wavelengths could have more error than others causing the waviness. However, if this was the case, both Wien coordinate spectra would have similar variation. Finally, waviness in Wien coordinates can originate from non-constant spectral emissivity. Spectral pyrometry reduces the effect of fluctuating spectral emissivity but does not eliminate it. Using spectral pyrometry technique, emissivity is assumed to be a gray body. Variation in spectral emissivity would cause a logarithmic variation in Wien coordinates. Spectral emissivity can be varying throughout the flame due to reactions that are happening throughout the flame. Waviness in Wien coordinates are most likely a combination of all of these factors.

7.3 Solidifying Copper

A zoomed and unprocessed multi-band plenoptic image of solidifying copper is displayed in Figure 7.7. The image was taken when most of the copper had solidified. The red circle indicates the edge of the graphite crucible, with any intensity outside of the red circle corresponding to the inner surface of the graphite. The yellow circle shows the location of the thermocouple used to monitor temperatures. Figure 7.7 also shows the temperature map that was calculated from the unprocessed image. Liquid copper is still present in the upper left side of the crucible as shown by the higher temperatures, which corresponds to the lower intensity region in the unprocessed image. Temperatures are relatively constant across regions of solidified copper. Some temperature calculation artifacts are seen at the boundaries between solid and liquid

phase. In these regions, temperature calculations indicate large temperature gradients, which are not expected.

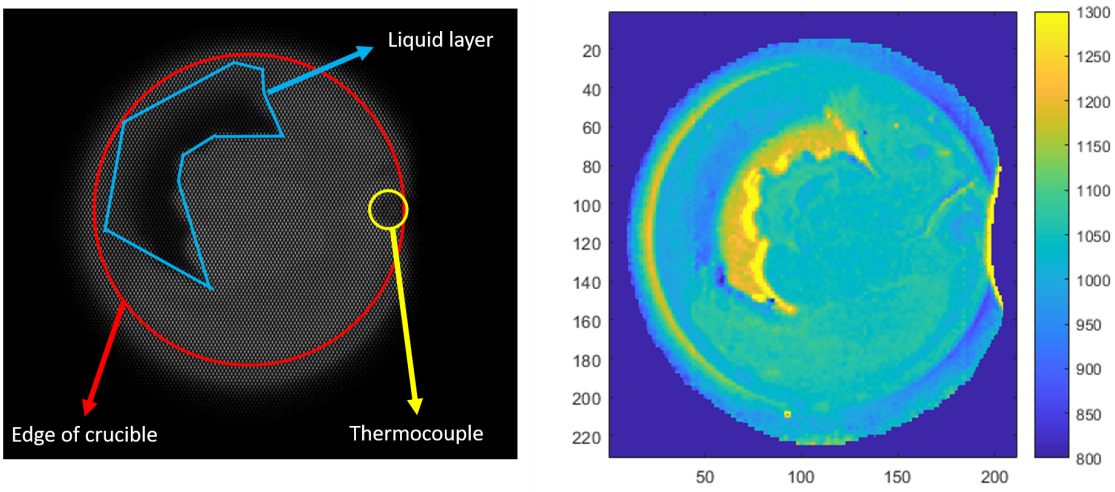

Figure 7.7: (Left) Raw multi-band plenoptic image that is zoomed into the location of copper during a phase of solidifying in a metal foundry, with the edge of the graphite crucible marked in red,thermocouple in yellow, and liquid layer of copper enclosed in blue. (Right) Temperature map (°C) produced by the raw multi-band plenoptic image.

Figure 7.8 shows the standard deviation in intensity in the v direction at a location corresponding to 750nm across the microlens plane. There are higher deviations at the edge of the crucible. Standard deviations are relatively small in regions of solidified copper. The significantly large standard deviation in intensity is observed at the boundary between solid and liquid phase. This variation of over 200 can be generated from either the emissivity difference between solid and liquid, or a physical height disparity is created due to stress across the boundary. The mean intensity for a wavelength of 750nm is shown in Figure 7.8. Intensities are much higher for solid copper compared to liquid copper, even though the liquid copper is at higher temperatures. At the boundary between liquid and solid copper, intensity gradually transitions from darker to brighter over several microlenses instead of being a sharp transition.

A zoomed in portion of a boundary in the raw multi-band plenoptic image is displayed in Figure 7.9. The microlenses at the boundary capture spectra that is not consistent to the surrounding microlens images corresponding to only liquid or solid copper. At the boundary, microlenses are capturing spectra from both liquid and solid copper. Microlenses outside the transition region have intensities fairly constant in v direction and have increasing intensity

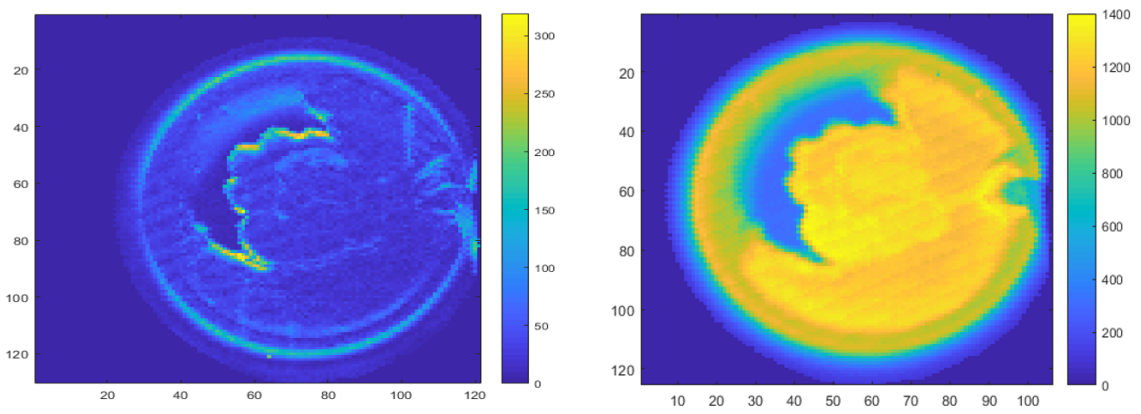

Figure 7.8: (Left) Standard deviation of intensities for each microlens in v direction for a given u location corresponding to 750nm. (Right) Mean intensity at each microlens for a u location corresponding to 750nm.

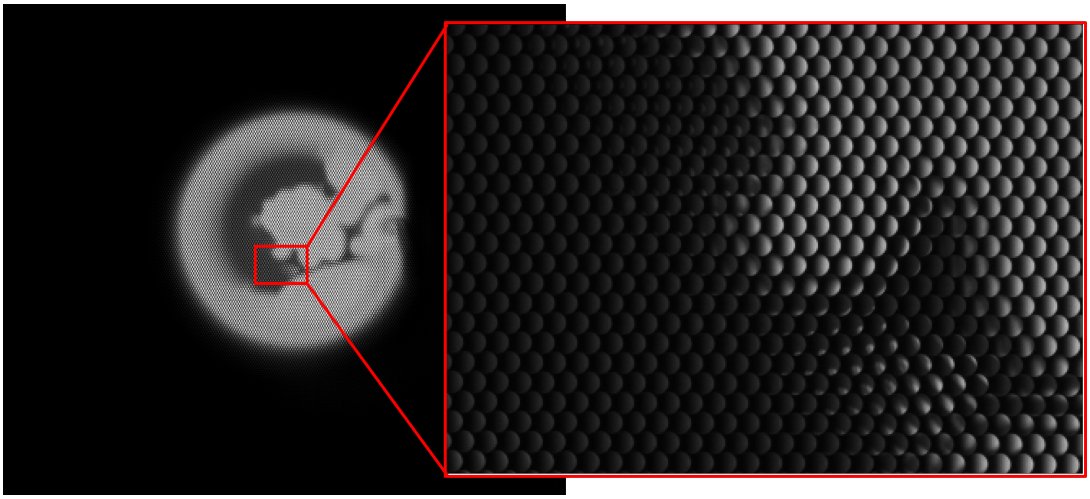

Figure 7.9: (Left) raw plenoptic image during phase change. (Right) A zoomed in image of one of the liquid and solid boundaries.

from left to right. Surface tension could develop at the solid/liquid interface that creates a physical slope, which could lead to problems with reflections on the liquid copper.

Average temperatures of a small region close to the thermocouple spanning a total time of 42 seconds are presented in Figure 7.10. For comparison, the thermocouple measurements are plotted over the same time interval. The solidifying/melting temperature of copper (1083°C) is marked on the graph with a horizontal green line. Since the end of the thermocouple is placed approximately 12 mm from the surface, temperature variation will be less because it is surrounded by copper. The surface might have more significant variations in temperature due to conduction and radiation heat transfer. Emitted radiation captured by the camera originates

from a very thin layer of atoms at the surface. A small window marked in red is a 12 x 12 microlens region used to calculate average temperatures. The small region changed phase after 19 seconds of recording the emitted radiation from the surface of the copper during cooling. The small region is depicted on the 2D temperature map of the copper at the point it transitions to solid from Figure 7.10. Averaging in that region smooths out some of the large temperature gradients that occur at the transition point of phase change. A general temperature decline is observed in both solid and liquid phases, while the phase change region has a sharp decrease in temperature. There is temperature variation in both regions as seen by the spikes and dips for each time step. Temperatures for a microlens contained in the red window is shown in Figure 7.10. As expected, there are larger temperature variation when compared to the average temperature, but the same trends are captured. A large drop in temperature appears during phase change due to boundary artifacts.

Figure 7.11 shows the evolution of temperatures across the copper for four different times during solidification. The first set of a plenoptic image and temperature map is of the copper in a complete liquid state, which shows large temperature variations across the copper. Higher intensities in the vicinity of the crucible sides could be occurring due to reflections from the crucible walls. Even though the walls could be at a lower temperature, the intensities emitted from the graphite wall will have higher intensities compared to the liquid copper due to emissivity values of approximately 0.8 for the graphite crucible. Also in the liquid state, small regions of lower temperature are located towards the center of the copper. These small regions could be generated due to impurities forming on the surface. Once all the copper is solid, the temperature variation is reduced. One thing to note about the temperature map once solid, the temperature increase approaching the edges of the crucible. There is approximately 15°C difference between the center and edges of the copper. The temperature difference could be occurring due to higher temperatures in the graphite crucible, which is caused by a smaller heat conductivity and larger thermal mass.

The multi-band plenoptic camera was able to capture temperatures in both liquid and solid phases for copper. The regions of melted copper had lower emissivity compared to solid copper, as can be seen by the lower intensities in liquid layer. Melted copper had very low SNR because

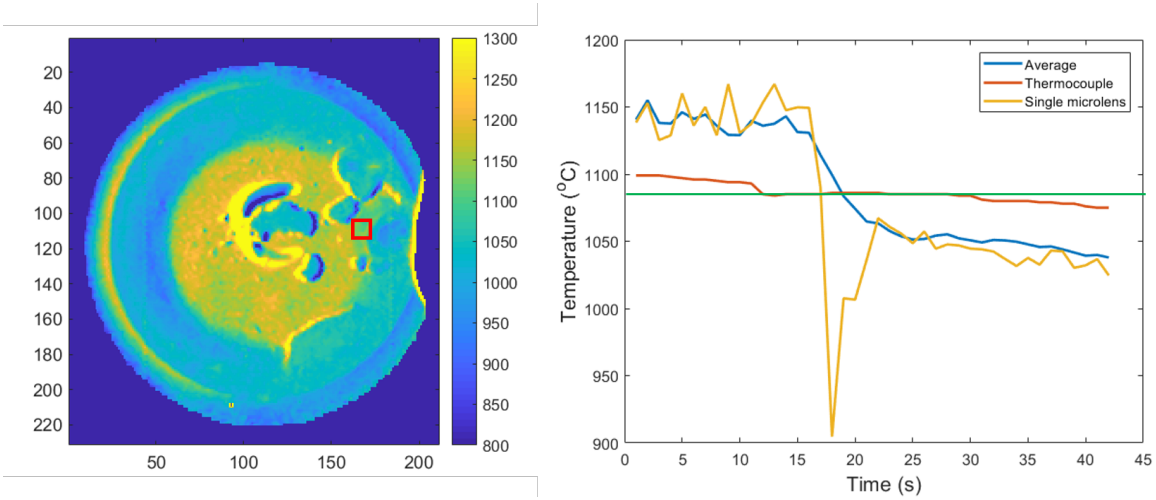

Figure 7.10: (Left) Temperature map (°C) of the copper melt pool at the instant the small region in red changes phase. (Right) Temperature versus time of the average temperatures measured by the camera in the red box, thermocouple temperatures, and temperatures measured by a single microlens. The green line indicates the melting temperature of copper (1083°C).

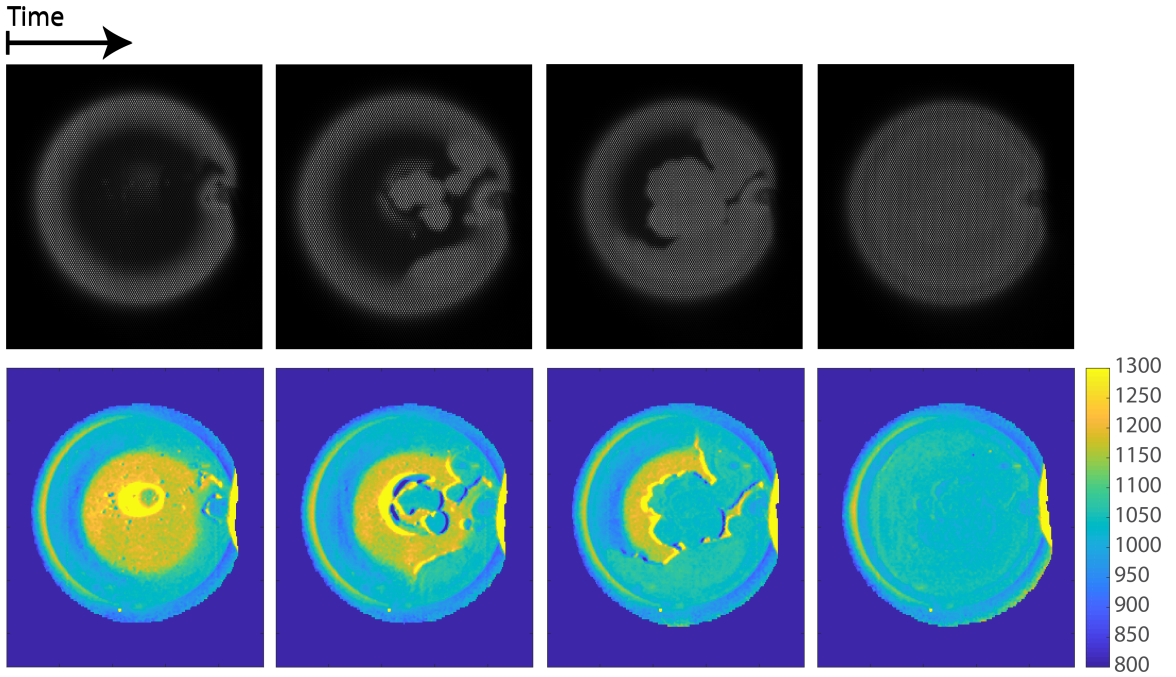

Figure 7.11: Time evolution of plenoptic images (top) and temperature map (°C) (bottom) of copper during solidification, starting with fully liquid to fully solid.

of the lower emitted radiation intensities, which can cause errors in temperature measurements. For this case, the dynamic range of the sensor was a limiting factor because SNR in the liquid region was very low. In the liquid regions, the maximum intensity values across the microlens was approximately 550. This is a small fraction of the largest intensity that can be recorded by

the sensor of 4095. As emitted intensity decrease, a larger percentage of the recorded signal will be composed of noise. Therefore, the low intensity in the liquid regions is a proposed reason for the larger temperature variations as shown in Figure 7.10. The amount that this effects the temperature measurement will be explored further. Another effect of low intensities is that it leads to less available wavelengths. Since all intensities are not the same across all wavelengths, less wavelengths will have high enough intensity to be recorded by the sensor as the maximum intensity decreases. With less wavelengths, the spectral pyrometry technique could have more variation in slope because of noise and emissivity effects. Similar to the waviness seen in the solid rocket plume measurements, errors could arise if that waviness occurs in the few wavelength samples that are captured for the liquid regions. In Figure 7.7, the liquid region was still indicating over 1100°C, while the solid layer was just below the melting temperature of copper. The temperature of copper at the solid and liquid boundary during phase change should be in thermal equilibrium. The speculations that are proposed in this paragraph will be investigated further in future work.

Artifacts at the boundary between solid and liquid phases originates from microlenses capturing both solid and liquid spectra in a single microlens as seen in Figure 7.9. Microlenses at the boundary had standard deviations up to 50% of the mean intensity. The intensities are different depending on the angle the light rays enter the camera, which is shown by variations in intensity with respect to v direction for a certain wavelength. If this is the case, either the copper is not within the depth of field of the camera or emissivity (reflections) could depend on the angle of emission. Boundary temperatures varied between 900°C to 1200°C within a few microlenses. Right edges of the boundaries are at the higher temperatures, while the left edges are much cooler. Another factor that could contribute to copper being out of focus is that liquid copper has increased reflectivity. Irradiation will now be reflected instead of absorbed, which needs to be accounted for when background temperatures are similar to the copper using Equation 2.7.

The general slope of temperatures in Figure 7.10 before and after the phase change are similar to that measured by the thermocouple at 0.67°C/sec. The slope steepens during phase change while the red box is close to the boundary. During phase change, the temperature should

remain fairly constant as represented by the thermocouple measurements in Figure 7.10. The large gradient in temperature during phase change could be physical, however, it is probable that the gradient is generated from boundary artifacts. When located at the boundary the calculated temperatures drop off significantly as shown by the single microlens measurements in Figure 7.10. Once the boundary moves away from the microlens, the temperature calculations are closer to the average temperature. Therefore, image artifacts occurring at the boundary could be the cause of the temperature gradient.

Liquid copper temperatures measured by the camera have a systematic difference of approximately 50°C above the thermocouple measurement. Thermocouples measured a maximum temperature of 1105°C, where the multi-band camera measured 1157°C close to the thermocouple. That is an difference of 4.7% in the liquid layer. One explanation for the temperature difference is the variation in spectral emissivity. It has been shown that liquid copper has larger emissivity values at shorter wavelengths, where emissivity at 500nm is approximately 0.35 compared to 0.1 at 800nm [52]. Therefore, intensities at shorter wavelengths will be higher than if the spectral emissivity was equal to that of 800nm. The higher intensities will cause the slope of Wien coordinates to increase, which would cause temperature calculations to increase accordingly.

Once the copper has completely solidified, copper temperatures measured by the camera differed from the thermocouple by approximately 30°C. One thing to note is that the thermocouple measurements are capturing temperatures within the copper, which could be at higher temperatures compared to the surface. The temperature difference can be caused by heat transfer occurring between the surface of the copper and the room temperature air. For heat transfer to be present, a temperature gradient is required throughout the copper. Therefore, this temperature difference of 30°C could be a physical phenomenon. However, this is a very complex 3D heat transfer problem, therefore, it would be hard to determine the exact temperature variation that is occurring throughout the copper. Another thing to note about the solid copper measurements is that temperature fluctuations are smaller in the solid regions compared to liquid regions as shown in Figure 7.10, which had variations of approximately 3°C and 15°C, respectively. The reduction in temperature variation could be generated by the much higher SNR in

the copper region as shown in Figure 7.9. Another reason for the larger variation in the liquid copper could originate from natural convection and other flow patterns within the liquid copper.

Chapter 8

Conclusions

This thesis presents a new multi-band snapshot camera combining plenoptic camera technology and a linearly variable wavelength filter to measure high temperatures of surfaces. A plenoptic camera creates an array of micro images of the aperture plane on the sensor through the use of a microlens array. Therefore, with a linearly variable wavelength filter placed at the aperture plane, micro-images of the spectral filter will be captured by the sensor. The multi-band plenoptic camera's current design captures 15 wavelength bands in the visible and near infrared spectrum (450nm - 800nm). An important feature of the multi-band plenoptic camera is the ability to alter the design of both the module and filter to generate the appropriate wavelength range and resolution. With up to 15 wavelength bands available, spectral pyrometry is used to calculate temperatures. Spectral pyrometry used the linearized Wien distribution equation to generate Wien coordinates. These coordinates are used to measure temperature, reducing the need to calculate surface emissivity. Before measuring temperatures the multi-band plenoptic camera requires three calibration steps including: microlens calibration, wavelength location calibration, and temperature calibration.

The multi-band adapter was created to be easily attached to the plenoptic camera to produce multi-band images. The multi-band module consists of a two lens configuration. The front lens collimates the light entering the camera, and it is designed for a specific working distance or magnification. The second lens is designed to f-match the microlenses for a given aperture size. The rainbow filter is placed between the first and second lens, which corresponds to an approximate aperture plane. The initial design of the multi-band module was able to capture spectra, but image artifacts were discovered that required accounting for or reducing by adjusting the design. The first suboptimal design characteristic was from the wavelength filter not

attenuating wavelengths from the near infrared spectrum in the section of the filter that corresponds to ultra-violet (<400nm). Another characteristic was wavelength location varying up to 2.5 pixels across the (s, t) plane because the filter is separated from the aperture plane. Lastly, wavelength location and temperature measurements had a periodic banding or "grid locking" effect that caused temperature fluctuations of up to 10 K across the image. The design utilized for the experiments in this thesis changed the second lens of the camera to have a shorter focal length of 75nm. This design change was chosen to image a smaller region of the spectral filter. It also increased wavelength resolution, reducing the periodic banding. The manual iris was replaced with a fixed 3D printed iris on the filter mount. Removal of the iris minimized the distance between the two lenses, allowing for the filter to be placed closer to the aperture plane. This reduced the wavelength shift to less than 0.8 pixels across the (s, t) plane.

Three experiments were designed to test and demonstrate the multi-band plenoptic camera's effectiveness in calculating 2D temperatures of an image. The first experiment included imaging graphite at both constant and varying temperatures within a box furnace. This experiment was an ideal case, where the calibration target was used for temperature measurements. It was found that the maximum difference between the thermocouple temperature and average temperature captured by the multi-band was less than 1%. Temperatures calculated by the camera fell within the accuracy of the thermocouple measurements. Standard deviation showed that fluctuation in temperature calculations across the graphite plate were within 0.5% of the average indicated temperature. Therefore, uncertainty of temperature measurements under well controlled and idealized conditions is less than 0.5%. The multi-band camera was also shown to capture the general trend measured by the thermocouple from a graphite plate cooling in a box furnace. The success of the experiment created motivations to apply the camera to problems that are challenging for other pyrometers.

The multi-band plenoptic camera was then used to measure temperatures of a solid fuel strand burner plume. Two different fuels, with known temperature differences, were chosen to test the camera's ability to capture flame temperatures, as well as, the temperature difference between the two fuels. The fuel samples were composed of hydroxyl-terminated polybutadiene (HTPB) and ammonium perchlorate (AP), with one having aluminum added to increase

flame temperatures. Mean temperatures from the camera around the thermocouple, showed comparable results to the temperatures measured by the thermocouple. The technique used does not account for line of sight integration, therefore the temperatures were biased towards higher temperatures. A temperature increase of over 400 K was recorded by both the camera measurements and thermocouples when aluminum was added to the fuel sample. The camera captured a temperature range of approximately 1000 K, corresponding to the dynamic range of the camera. The 3D structure of the flame added complexities with burning particle and portions of the flame being outside the DOF. This experiment shows that the instrument can be utilized in a more dynamic environment with spatially and time varying features. However, the DOF of the camera and line of sight measurements should be accounted for to ensure accurate temperatures. The instrument is limited to only capturing 2D temperature maps of 3D structures like flames.

Finally, an experiment imaging copper during the phase change between liquid and solid is used to determine the camera's ability in capturing temperatures of with two different material properties present. Liquid copper has material properties such as low and varying spectral emissivity and high reflectivity which have typically challenged traditional optical pyrometers. The camera was able to measure temperatures within both the liquid and solid regions, and distinguish between the two. However, the liquid region measurements had several artifacts that affected the temperature measurements. One artifact occurred at the liquid and solid copper boundary. Large temperature gradients were measured, which could have been caused by reflective nature of liquid copper. Temperatures calculated from the camera were $>50°C$ compared to the thermocouple measurements. The systematic error potentially occurs due to spectral emissivity increasing in the shorter wavelengths of the visible spectrum. In the vicinity of the wall of the crucible, measured liquid temperatures were less than melting temperature. One explanation for the lower temperatures was that the crucible radiation could have been reflected by the liquid. Since the graphite crucible has higher emissivity, the radiation is brighter and takes dominance over the liquid radiation. Once the copper was solid, the temperature distribution was smoother and had less variations across the image. Overall, the multi-band plenoptic camera was able to calculate temperatures for two very different surface properties

between the liquid and solid copper. The camera is limited by the amount of intensity levels it can capture, which was exemplified by low intensities in the liquid region from low emissivity. Also, the instrument is limited by the algorithm's assumption that surface emissivity does not vary spectrally. When imaging reflective surfaces, background radiation interferes with the intensities captured by the multi-band plenoptic camera. Therefore, the camera is limited to cases of low reflectivity and background temperatures.

In future developments, wavelength calibration will account for variation in wavelength location in the v direction instead of averaging. This should lead to the ability to capture stereoscopic angular wavelength information about a scene in the v direction. Investigation into using both angular and spectral information will be conducted to calculate 3D temperature measurements. Also, adding the capability to calculate emissivity will be useful for experiments with varying material properties like flames and liquefied metals. Liquid copper measurements showed the importance of accounting for reflectivity, especially when emissivity is low and background temperatures are high. Therefore, algorithm development will try to account for background radiation. Research into a more suitable IR filter will be conducted to better balance intensities across the captured spectrum. To help increase the dynamic range in temperature measurements, the capability to dynamically alter the wavelengths used from each microlens will be added to the algorithm.

Future experiments will investigate the instrument's ability to capture solid rocket plume temperatures at high pressures. Furthermore, the multi-band plenoptic camera will be used to measure temperatures in hypersonic heating of surfaces and capture defects in additive manufacturing. Many of the future experiments will be able to capture time-resolved temperature measurements using a high-speed plenoptic camera. Not only can the multi-band plenoptic be used for temperature measurements, but it can also be used to generate colored images from an intensified plenoptic camera. As light passes through an intensifier, the wavelength information is compromised. However, the multi-band plenoptic camera module can be added before the intensifier to encode wavelength onto angular information.

References

[1] Araújo, A., "Multi-spectral pyrometry — a review," *Measurement Science and Technology*, 2017.

[2] Ketui, D., Chi, F., and Shan, G., "Single wavelength and ratio pyrometry reflection errors in temperature measurement of gas turbine blade," *Measurement*, Vol. 86, 2016, pp. 133–140.

[3] Danehy, P. M., Hutchins, W. D., Fahringer, T. W., and Thurow, B. S., "A Plenoptic Multi-Color Imaging Pyrometer," *55th AIAA Aerospace Sciences Meeting*, , No. January, 2017, pp. 1–7.

[4] Fu, T., Liu, J., and Tian, J., "VIS-NIR multispectral synchronous imaging pyrometer for high-temperature measurements," *Review of Scientific Instruments*, Vol. 88, No. 6, 2017, pp. 1–8.

[5] Fu, T., Liu, J., Duan, M., and Li, S., "Sub-pixel temperature measurements in hypersonic plasma jet environments using high speed multispectral pyrometry," *Journal of Heat Transfer*, Vol. 140, No. July 2018, 2018, pp. 1–7.

[6] Gao, S., Wang, L., Feng, C., Xiao, Y., and Daniel, K., "Multi-spectral pyrometer for narrow space with high ambient temperature," *Optical Review*, Vol. 22, No. 4, 2015, pp. 605–613.

[7] Fu, T., Yang, Z., Wang, L., Cheng, X., Zhong, M., and Shi, C., "Measurement performance of an optical CCD-based pyrometer system," *Optics and Laser Technology*, Vol. 42, No. 4, 2010, pp. 586–593.

[8] Fu, T., Zhao, H., Zeng, J., Wang, Z., Zhong, M., and Shi, C., "Improvements to the three-color optical CCD-based pyrometer system," *Applied Optics*, Vol. 49, No. 31, 2010, pp. 5997.

[9] Magunov, A. N., "Spectral pyrometry (Review)," *Instruments and Experimental Techniques*, Vol. 52, No. 4, Feb 2009, pp. 451–472.

[10] Hagen, N. and Kudenov, M. W., "Review of snapshot spectral imaging technologies," *Optical Engineering*, Vol. 52, No. 9, sep 2013, pp. 090901.

[11] Fahringer, T. W., Danehy, P. M., and Hutchins, W. D., "Design of a Multi-Color Plenoptic Camera for Snapshot Hyperspectral Imaging," *2018 Aerodynamic Measurement Technology and Ground Testing Conference*, 2018, pp. 1–9.

[12] Levoy, M., Ng, R., Adams, A., Footer, M., and Horowitz, M., "Light field microscopy," *SIGGRAPH06: Special Interest Group on Computer Graphics and Interactive Techniques Conference*, Jul 2006.

[13] Levoy, M. and Hanrahan, P., "Light Field Rendering," *ACM SIGGRAPH*, 1996, pp. 609–614.

[14] Kelly, D. L., Phillips, M. A., Thurow, B. S., and Scarborough, D. E., "A Novel Multiband Plenoptic Pyrometer used for Temperature Measurements of Strand Burner Plumes," *AIAA Scitech 2020 Forum*, May 2020.

[15] Coates, P. B., "Multi-Wavelength Pyrometry," *Metrologia*, Vol. 17, No. 3, jul 1981, pp. 103–109.

[16] Bergman, T. L., Lavine, A., and Incropera, F. P., *Fundamentals of heat and mass transfer*, John Wiley & Sons, Inc., 2019.

[17] Minkina, W., Dudzik, S., and Baran, J., *Infrared thermography: errors and uncertainties*, A John Wiley and Sons, Ltd, Publication, 2009.

[18] Zhang, Y., Lang, X., Hu, Z., and Shu, S., "Development of a CCD-based pyrometer for surface temperature measurement of casting billets," *Measurement Science and Technology*, Vol. 28, No. 6, 2017.

[19] Tsai, B. K., Shoemaker, R. L., Dewitt, D. P., Cowans, B. A., Dardas, Z., Delgass, W. N., and Dail, G. J., "Dual-wavelength radiation thermometry: Emissivity compensation algorithms," *International Journal of Thermophysics*, Vol. 11, No. 1, 1990, pp. 269–281.

[20] Jenkins, T. and Hanson, R., "Soot pyrometry using modulated absorption/emission," *Combustion and Flame*, Vol. 126, No. 3, 2001, pp. 1669–1679.

[21] Stasio, S. D. and Massoli, P., "Influence of the soot property uncertainties in temperature and volume-fraction measurements by two-colour pyrometry," *Measurement Science and Technology*, Vol. 5, No. 12, Jan 1994, pp. 1453–1465.

[22] Zhao, H. and Ladommatos, N., "Optical diagnostics for soot and temperature measurement in diesel engines," *Progress in Energy and Combustion Science*, Vol. 24, No. 3, 1998, pp. 221–255.

[23] Vattulainen, J., Nummela, V., Hernberg, R., and Kytölä, J., "A system for quantitative imaging diagnostics and its application to pyrometric in-cylinder flame-temperature measurements in large diesel engines," *Measurement Science and Technology*, Vol. 11, No. 2, Jul 2000, pp. 103–119.

[24] Duvaut, T., "Comparison between multiwavelength infrared and visible pyrometry: Application to metals," *Infrared Physics and Technology*, Vol. 51, No. 4, 2008, pp. 292–299.

[25] Fu, T., Liu, J., Tang, J., Duan, M., Zhao, H., and Shi, C., "Temperature measurements of high-temperature semi-transparent infrared material using multi-wavelength pyrometry," *Infrared Physics and Technology*, Vol. 66, 2014, pp. 49–55.

[26] Fu, T., Tan, P., Pang, C., Zhao, H., and Shen, Y., "Fast fiber-optic multi-wavelength pyrometer," *Review of Scientific Instruments*, Vol. 82, No. 6, 2011.

[27] Ng, D. and Fralick, G., "Use of a multiwavelength pyrometer in several elevated temperature aerospace applications," *Review of Scientific Instruments*, Vol. 72, No. 2, 2001, pp. 1522.

[28] Madura, H., Kastek, M., and Piatkowski, T., "Automatic compensation of emissivity in three-wavelength pyrometers," *Infrared Physics and Technology*, Vol. 51, No. 1, 2007, pp. 1–8.

[29] Araújo, A., "Analysis of multi-band pyrometry for emissivity and temperature measurements of gray surfaces at ambient temperature," *Infrared Physics & Technology*, Vol. 76, 2016, pp. 365–374.

[30] Modest, M. F., *Radiative Heat Transfer*, Academic Press Inc, 2013.

[31] Ishii, T., "Proposal of quantitative temperature measurement using two-color technique combined with several infrared radiometers having different detection wavelength bands," *Optical Engineering*, Vol. 40, No. 3, Jan 2001, pp. 372.

[32] Fu, T., Cheng, X., Fan, X., and Ding, J., "The analysis of optimization criteria for multi-band pyrometry," *Metrologia*, Vol. 41, No. 4, 2004, pp. 305–313.

[33] Fu, T., Cheng, X., Wu, B., Zhong, M., Shi, C., and Liu, T., "The measurement coordinates for multi-band pyrometry," *Measurement Science and Technology*, Vol. 17, No. 2, Apr 2006, pp. 379–383.

[34] Shogenji, R., Kitamura, Y., Yamada, K., Miyatake, S., and Tanida, J., "Multispectral imaging using compact compound optics," *Optics Express*, Vol. 12, No. 8, 2004, pp. 1643.

[35] Horstmeyer, R., Athale, R., and Euliss, G., "Modified light field architecture for reconfigurable multimode imaging," Vol. 746804, No. August 2009, 2009, pp. 746804.

[36] Mitchell, T. A. and Stone, T. W.

[37] Yu, Z., Yu, J., Lumsdaine, A., and Georgiev, T., "An analysis of color demosaicing in plenoptic cameras," *2012 IEEE Conference on Computer Vision and Pattern Recognition*, 2012.

[38] Lippmann, G., "Épreuves réversibles donnant la sensation du relief," *Journal de Physique Théorique et Appliquée*, Vol. 7, No. 1, 1908, pp. 821–825.

[39] Gershun, A., "The Light Field," *Translated by P.Moon and G. Timoshenkoin Journal of Mathematics and Physics*, Vol. XVIII, 1936, pp. 51–151.

[40] Adelson, E. H. and Bergen, J. R., "The plenoptic function and the elements of early vision." *Computational models of visual processing*, 1991.

[41] Adelson, E. and Wang, J., "Single lens stereo with a plenoptic camera," *IEEE Transactions on Pattern Analysis and Machine Intelligence*, Vol. 14, No. 2, 1992, pp. 99–106.

[42] Ng, R., Levoy, M., and Duval, G., "Light Field Photography with a Hand-held Plenoptic Camera," *Stanford Tech Report*, Vol. 39, No. 8, aug 2005.

[43] Fahringer, T. W., Lynch, K. P., and Thurow, B. S., "Volumetric particle image velocimetry with a single plenoptic camera," *Measurement Science and Technology*, Vol. 26, No. 11, 2015.

[44] Fahringer, T. W. and Thurow, B. S., "Plenoptic particle image velocimetry with multiple plenoptic cameras," *Measurement Science and Technology*, Vol. 29, No. 7, 2018.

[45] Clifford, C. J., Klemkowsky, J. N., and Thurow, B. S., "Volumetric Schlieren of a Shock / Boundary Layer Interaction using a Plenoptic Camera," .

[46] Johnson, K. C., Thurow, B. S., Kim, T., Blois, G., and Christensen, K. T., "Volumetric Velocity Measurements in the Wake of a Hemispherical Roughness Element," *AIAA Journal*, Vol. 55, No. 7, 2017, pp. 2158–2173.

[47] Klemkowsky, J. N., Clifford, C. J., Bathel, B. F., and Thurow, B. S., "A direct comparison between conventional and plenoptic background oriented schlieren imaging," *Measurement Science and Technology*, Vol. 30, No. 6, 2019, pp. 064001.

[48] Hall, E. M., Guildenbecher, D. R., and Thurow, B. S., "Development and uncertainty characterization of 3D particle location from perspective shifted plenoptic images," *Optics Express*, Vol. 27, No. 6, Apr 2019, pp. 7997.

[49] Tan, Z. P., Johnson, K., Clifford, C., and Thurow, B. S., "Development of a modular, high-speed plenoptic-camera for 3D flow-measurement," *Optics Express*, Vol. 27, No. 9, 2019, pp. 13400.

[50] Bolan, J., Hall, E., Clifford, C., and Thurow, B., "Light-Field Imaging Toolkit," *SoftwareX*, Vol. 5, 2016, pp. 101–106.

[51] Cagran, C. and Pottlacher, G., "Normal spectral emissivities of liquid copper, liquid gold and liquid silver at 684.5nm," *Journal of Non-Crystalline Solids*, Vol. 353, No. 32-40, 2007, pp. 3582–3586.

[52] Cagran, C., "Normal Spectral Emissivity of Liquid Copper and Liquid Silver at 684.5 nm," *AIP Conference Proceedings*, 2003.

[53] Nagata, K., Nagane, T., and Susa, M., "Measurement of Normal Spectral Emissivity of Liquid Copper." *ISIJ International*, Vol. 37, No. 4, 1997, pp. 399–403.

[54] Kurosawa, R., Inoue, T., Baba, Y., Sugioka, K.-I., Kubo, M., Tsukada, T., and Fukuyama, H., "Normal spectral emissivity measurement of molten copper using an electromagnetic levitator superimposed with a static magnetic field," *Measurement Science and Technology*, Vol. 24, No. 1, Oct 2012, pp. 015603.

Appendices

Appendix A

Derivation of Linearized Wien Function

In this section, we will derive the linearized Wien's distribution equation that is used for spectral pyrometry.

$$I_{Wien}(\lambda, T) = \frac{2hc^2}{\lambda^5} \exp\left(-\frac{hc}{\lambda kT}\right) \tag{A.1}$$

$$I = \varepsilon I_{Wien} \tag{A.2}$$

Substituting Equation A.1 into Equation A.2, to account for a real surface.

$$I = \varepsilon \left[\frac{C_1}{\lambda^5} \exp\left(-\frac{C_2}{\lambda T}\right)\right] \tag{A.3}$$

$$\frac{\lambda^5 I}{\varepsilon C_1} = \exp\left(-\frac{C_2}{\lambda T}\right) \tag{A.4}$$

$$\ln\left[\frac{\lambda^5 I}{\varepsilon C_1}\right] = \ln\left[\exp\left(-\frac{C_2}{\lambda T}\right)\right] \tag{A.5}$$

$$\ln(\lambda^5 I) - \ln(\varepsilon C_1) = -\frac{C_2}{\lambda T} \tag{A.6}$$